Abstract of "First-Principles Calculations of Alloy Free Energies" by Sayan Samanta, Ph.D., Brown University, October 16, 2022.

High-throughput computational thermodynamic approaches are becoming an increasingly popular tool to uncover novel compounds. However, traditional methods tend to be limited to stability predictions of stoichiometric phases at absolute zero. Such methods thus carry the risk of identifying an excess of possible phases that do not survive to temperatures of practical relevance. We demonstrate how the CALPHAD formalism, informed by simple first-principles input can be used to overcome this problem at a low computational cost and deliver quantitatively useful phase diagram predictions at all temperatures. We illustrate the method by re-assessing prior compound formation predictions and reconcile these findings with long-standing experimental evidence to the contrary.

Coupled with the Special Quasirandom Structure (SQS) formalism, CALPHAD offers a natural and efficient tool to generate input data for disordered solid solution phases. However, accounting for short range order (SRO) effects in a computationally efficient way presents a challenge. In this work we augmented the aforementioned computational toolkit to utilize the Cluster Variation Method (CVM) method in tandem with the SQS formalism. Our approach, implements the CVM to any level of accuracy, and determines a closed-form nonlinear expressions for temperature-dependent SRO corrections to the formation free energies. As a proof of concept, we re-assess the Ir-Ru binary alloy with SRO correction and show that under the tetrahedron approximation, the SRO correction to the hcp phase is sufficient to accurately reproduce the known experimental phase diagram.

Beyond equilibrium phase properties, the gamut of material properties of interest in engineering applications, extend to kinetically stabilized phases such as in Bulk Metallic Glasses (BMG). However experimental assessment of liquid properties is a time and economic bottleneck. To address this, we develop an Embedded Atom Method (EAM) force-field for the family of Zr-Cu-Al-Ni from a set of first principle calculations as reference data. The EAM was validated using an independent test data-set. Molecular Dynamics simulations to calculate equilibrium volume and viscosity at different liquid temperatures stipulate a good agreement with known experimental trends. Our developed EAM would thus be instrumental in accelerating screening of candidate BMG alloys of the Zr-Cu-Al-Ni family in a high-throughput pipeline.

First-Principles Calculations of Alloy Free Energies

by

Sayan Samanta

M.Tech, Materials Science, IIT Bombay, India, 2016
B.Tech, Metallurgical Engg., NIT Durgapur, India, 2014

A dissertation submitted in partial fulfillment of the
requirements for the Degree of Doctor of Philosophy
in the School of Engineering at Brown University

Providence, Rhode Island
October 16, 2022

This dissertation by Sayan Samanta is accepted in its present form by the School of Engineering as satisfying the dissertation requirement for the degree of Doctor of Philosophy.

Date _____ _____

Axel van de Walle, PhD, Advisor

Recommended to the Graduate Council

Date _____ _____

Yue Qi, PhD, Reader

Date _____ _____

Andrew Peterson, PhD, Reader

Approved by the Graduate Council

Date _____ _____

Thomas A. Lewis, PhD

Dean of the Graduate School

Curriculum Vitae

Sayan Samanta graduated first class with distinction from National Institute of Technology, Durgapur, India in 2014 where he received his Bachelor of Technology degree in Metallurgical Engineering and Materials Science. He received his Master of Technology degree in Materials Science from Indian Institute of Technology, Bombay, India in 2016. En route to his dissertation studies, he also obtained a transitional Master of Science degree in Engineering from Brown University in 2019. In his years of graduate research, he has published 2 journal articles and presented in 1 conference talk. He has 3 other manuscripts in preparation from results borne out of his PhD investigations. He has also acted in the role of Teaching assistant for 2 under-graduate and 2 graduate courses in engineering and data science. He also possesses hands-on expertise on implementing common Machine Learning/Deep Learning pipelines which he obtained in an informal foray in to Data Science concurrent to his PhD studies.

Publications

1. **Samanta, Sayan** & van de Walle, A. Rapid screening of high-throughput ground state predictions. *Calphad* **74,** 102306. ISSN: 0364-5916. https://arxiv.org/abs/2204.08963 (2021) (Sept. 2021)

2. van de Walle, A., Chen, H., Liu, H., Nataraj, C., **Samanta, Sayan**, Zhu, S., *et al.* Interactive Exploration of High-Dimensional Phase Diagrams. *JOM.* ISSN: 1047-4838, 1543-1851. https://link.springer.com/10.1007/s11837-022-05314-z (2022) (May 2022)

3. **Samanta, Sayan** & van de Walle, A. CVM Correction for Short Range Ordering in Iridium-Ruthenium Binary Phase Diagram (in preparation)

4. **Samanta, Sayan** & van de Walle, A. A software implementation to introduce SRO corrections to alloy free energies in the CALPHAD formalism (in preparation)

5. **Samanta, Sayan** & van de Walle, A. Classical EAM Force-Field construction of Zr-Cu-Al-Ni class of Bulk Metallic Glasses (in preparation)

Talks

1. **Samanta, Sayan** & van de Walle, A. *MS&T Technical Meeting and Exhibition* Integration between Modeling and Experiments for Crystalline Metals: From Atomistic to Macroscopic Scales. Columbus, Ohio, Oct. 2021. https://www.youtube.com/watch?v=eTrj0zlZiXU
2. **Samanta, Sayan**. *Inclusive application of numerical techniques in Materials Science* The Sheridan Teaching Seminar - Reflective Teaching (Certificate I). 2018. https://www.youtube.com/watch?v=S5bYc03QrgA

Teaching Experience

1. ENGN 0720 Thermodynamics (Spring 2019)
2. ENGN 0410 Materials Science (Fall 2019)
3. ENGN 2020 Mathematical Methods in Engineering and Physics II (Spring 2020)
4. DATA 2040 Deep Learning and Special Topics in Data Science (Spring 2021)

Positions of Responsibility

1. Chair of Social Events, Graduate Student Council, Brown University (2019)

Acknowledgements

If I have seen further, it is by standing on the shoulders of giants

Sir Isaac Newton

I would first and foremost thank my advisor, Prof. Axel van de Walle for his unbridled faith and near infinite patience that he showed on me from the genesis of my doctoral studies. From the first meeting till today Prof. Axel has been a constant support towards all things which I felt would help my career ahead even if didn't align perfectly with the group targets. He is extremely responsive person over email and I'm thankful for all the threads and discussion which has helped me progress towards a better material scientist (still improving !!!). His regard to details and his ability to break down the most complex concepts in an intuitive manner are lessons that shall pervade not just in research but overall philosophy of life.

Coming from a drug-delivery experimental background, I lacked the basic pre-requisites to work at a lab which does atomistic simulations. Fortunately due to the spectacular courses at Brown taught by ingenious Engineering, Physics, Chemistry and Data Science faculty members, I quickly got up to speed. Besides instructions, their affable personality and accessibility offered by them made my steep learning curve enjoyable and thrilling. The teaching-assistants deserve a special mention for their zeal in helping me and my colleagues often after regular hours and over weekends.

My past and present colleagues from the van de Walle group : Dr. Sara Kadkhodaei was my first mentor who got me started in the lab. A lot of the concepts and experimental practices during my PhD were taught to me by her. My fellow doctoral colleagues : Dr. Chiraag Nataraj, Helena Liu, Siya Zhu and Hantong Chen, beside being one of the smartest folks I know, are also exemplary researchers who are my constant source of motivation and inspiration to continue doing good work.

I'm pretty sure that this academic journey could not have reached this culmination without the camaraderie of the ratpack gang I call friends. The geek squad : Dr. Juny Cho, Nate Lussier, Dr. Mok Yun Jin, Dr. Nupur Jain and Dr. Selda Büyüköztürk and Dr. Laura Turcer; I cherished solving homeworks together and our unforgettable GCB trips. The Hermits : Siddhant Agarwal, Aravind

Anchala, Miranda Friel, Jason Roth, Ari Kohorn, Tarun Sharma, Dr. Sabina Stefan and Amrita Ramanathan, thank you for making Providence seem like a home away from home. Shout-out to Harsh Jagad, Tejas Kotwal, Gopal Iyer, Ramisa Fariha, Dr. Hammad Faizi, Dr. Srinivas Iyer, thanks for all the tea, biryani and hikes.

Life throws strangers at you all times, some of them become friends and a few become brothers. I have a special place in my heart for two of my brothers. Juny Cho is my cohort, my office-mate, my room-mate, my sensei and a friend for life. He taught me how to lift weights, he taught my how to drive. Always true, never hesitating to say the right thing, this gem of a human has been an integral component of what made this PhD a holistic and extremely fun learning experience. The other musketeer, Shubham Sharma and I shared a lot of our 'firsts' together. We arrived together, two awkward indians in a strange new country, we had our first snow experience, first calzone, first fireball, and many more experiences that shall remain etched in my memory forever. Thank you guys for all the good times.

No amount of words could do justice to my gratitude I feel towards my girlfriend, Ms. Yidan Bi. Of all the strokes of luck, that lady luck bestowed upon me, Ms. Bi's affection is the biggest of them all. Riding the tumultuous waves of graduate school together, she has been there with me through thick and thin. Her innate sense of discipline and unfathomable capacity to care about her fellow colleagues has been an ardent example and a guiding stick to keep me on-wards in the path of success without ever compromising with the highest standards of academic and personal integrity. 我爱你.

And finally, a big thanks to my Parents and my Grandparents. Thank you for inculcating the scientific bug into me. Thanks to all those trips to the book-fair and the science museum. Thank you for answering patiently all the myriad of questions which I had been bombarding you with since I was kid. Thanks for that Windows 98 PC you got me. Thanks for dragging me to IITJEE coaching. Thanks for the gift of existence and love. Look, I did it! I did get a PhD!

Contents

List of Tables

List of Figures

Chapter 1

Introduction

Computational methods in Materials science are the Yin to the Yang of the time and tested experimental methods to probe, measure, understand and predict material properties. Although experimental results are unequivocal ground truths, interactions governing physical properties act on length and time scales ranging between more than 10 orders of magnitude thus limiting the feasibility of experiments on grounds of complexity and economy. In particular, in the field of Alloy Thermodynamics, the sheer size of the composition-structure phase space of alloys make any sort of high-throughput experimental prototyping of novel alloys an indomitable challenge. Experiments are also at times difficult to control for precision in a direct and cost-effective way; Computer calculations on the other hand offer precise control and measurement over all the parameters of the *virtual experiments*, and thus are an excellent supplement and often complement to *real experiments* especially in small time and length scales.

> "Calculate what you cannot measure; measure what you cannot calculate."

Unfortunately at low length scales ($\sim$ Å), the quantum nature of large number of interacting particles pose a computational challenge - A full and accurate quantitative prediction of free energies of *real alloys* although in principle is a solved problem, is impossible in practice due to the "Curse of Dimensionality" [1]. This bottleneck was extremely severe up to the 1970's where the silicon revolution made processors cheaper and faster at an exponential rate[2]. Keeping up with hardware advancements, user-friendly programming languages[3, 4], efficient numerical libraries[5, 6] and more recently, specialized software for targeted special-purpose hardware were developed[7–9]. Concurrently revolutionary theoretical ideas in condensed state physics developed approximate theories which were very accurate enough for predictive analysis at the operating temperature of material applications. These were amenable to be implemented in the modern computers efficiently. Courtesy of which, first-principles simulations up to $\sim$ 150 atoms and dynamic simulation of event up to $\sim$ 1 ps is now routine.

However to establish an end-to-end pipeline from purely first-principles results to accurately predict phase stability of solid alloys or bulk properties of liquids such as viscosity, a larger system and for longer time has to be sampled to eliminate the inherent statistical biases which may be an artifact of arbitrary initial state. While this is not a straightforward task, the modus operandi of theories aiming to target this research niche almost always include the following steps:

1. Generating a dataset : Calculation of reference data-set of known input-output pairs. For eg. a dataset of alloy structures and energy obtained from a accurate yet size limited first-principles method.

2. Basis set selection: Using prior knowledge of the physics of the system, a choice of basis functions is made. Such that it is defined at every possible input variable and it spans the space of the output variable smoothly. Ideally a good choice of basis set is such which encodes the symmetry of the system. Often it is also used as a dimensionality reduction technique where the basis functions maps the input space to a lower dimensional space while preserving most of the correlations while removing any linear dependencies. For eg. In an ideal lennard-jones fluid, converting atomic coordinates to a list of pair distance might be a good choice since radial distances are spherically symmetric (like energies), and the energy is a function of radial distance between pairs of atoms rather than absolute positions.

3. Fitting an analytical function : Construct a function on the space spanned by the basis sets that maps each point to a desired thermodynamic quantity.

The fitted functions parameterize the underlying crucial physics of the system which can then be used to expedite alloy prototyping while being reasonably accurate, physically consistent and often systematically improvable.

In this thesis, we shall discuss 3 such methods : CALPHAD technique, Cluster Variation Method (CVM) and Embedded Atom Method (EAM) Inter-atomic Potentials. In Chapter 2 we shall review the theoretical foundations behind all the methods including Density Functional Theory (DFT), which is a first-principles technique to evaluate the electronic ground state structure and associated (free) energies. In this thesis, DFT would be the assumed ground truth. The theoretical discussions are neither original to this thesis nor a comprehensive one, however the format of presentation is designed for easy comprehension of the software implementation and results of the computer experiments performed in the following chapters. It is also instructive for any new entrant in this line of research. In Chapter 3 we employ the Compound Energy Formalism and the CALPHAD method to model alloy free energy as a sum of parametric polynomials, each representing a particular single and multi-body sub-interaction in the system. We also introduce Special Quasirandom Structures (SQS) which are particularly designed to eliminate spurious correlations due the small cell size in first-principles calculations. In concert, we demonstrate a software toolkit `sqs2tdb`; to predict alloy phase diagrams purely from first-principles in a systematically improvable fashion. In

Chapter 4 we exhibit a `python` based software implementation the CVM method to introduce temperature dependent Short Range Order (SRO) corrections to alloy free energies integrated into the CALPHAD+SQS paradigm from Chapter 3. This eliminates the prediction of fallacious ordered phases which incidentally undergo a order-disorder transformation at temperature window lower than the application regime and substantially improves the computed phase diagrams. In Chapter 5, an Embedded Atom Method (EAM) classical interatomic potential was developed for the Zr-Cu-Al-Ni Bulk Metallic Glass (BMG) forming liquid alloys. The fitted potential was validated using an independent test dataset. Molecular Dynamics (MD) simulation were conducted with the fitted EAM to calculate equilibrium volume and shear viscosities. The results were found to be within the same orders of magnitude as other compositions in the same family of BMGs (sans Ni) and express consenting trends. Finally in the last Chapter 6, we do a recap of the previous discussions concluded by some musings on possible future investigations.

References

1. Bellman, R. *Dynamic Programming (Dover Books on Computer Science)* Paperback, 384 (Dover Publications, Mar. 4, 2003).
2. Gustafson, J. L. in *Encyclopedia of Parallel Computing* (ed Padua, D.) 1177–1184 (Springer US, Boston, MA, 2011).
3. Van Rossum, G. & Drake, F. L. *Python 3 Reference Manual* (CreateSpace, Scotts Valley, CA, 2009).
4. Bezanson, J., Edelman, A., Karpinski, S. & Shah, V. B. Julia: A fresh approach to numerical computing. *SIAM review* **59,** 65–98 (2017).
5. Harris, C. R., Millman, K. J., van der Walt, S. J., Gommers, R., Virtanen, P., Cournapeau, D., *et al.* Array programming with NumPy. *Nature* **585,** 357–362 (2020).
6. Virtanen, P., Gommers, R., Oliphant, T. E., Haberland, M., Reddy, T., Cournapeau, D., *et al.* SciPy 1.0: Fundamental Algorithms for Scientific Computing in Python. *Nature Methods* **17,** 261–272 (2020).
7. Einspruch, N. *Application specific integrated circuit (ASIC) technology* (Academic Press, 2012).
8. Bradbury, J., Frostig, R., Hawkins, P., Johnson, M. J., Leary, C., Maclaurin, D., *et al. JAX: composable transformations of Python+NumPy programs* version 0.3.13. 2018. http://github.com/google/jax.
9. Martín Abadi, Ashish Agarwal, Paul Barham, Eugene Brevdo, Zhifeng Chen, Craig Citro, *et al. TensorFlow: Large-Scale Machine Learning on Heterogeneous Systems* 2015. https://www.tensorflow.org/.

Chapter 2

Computational Methods

2.1 Density Functional Theory

The ground state of quantum particles (electron and protons) under the action of an external potential is governed by the Many-body Time Independent Schrodinger's Wave Equation[1]

$$\left[-\frac{\hbar^2}{2m}\nabla^2 + V(x)\right]\psi(x) = E\psi(x) \tag{2.1}$$

x is the spatial coordinates of the particles and $V(x)$ is the external potential energy field acting on them. $\psi(x)$ is the quantum wavefunction such that $\int |\psi(x)|^2$ gives the electronic charge density of the system. However to overcome the computational intractability of solving the full wavefunction, Density Functional theory (DFT) was formulated as an approximation to the ground state wavefunction. The cornerstone of DFT are the Hohenberg-Kohn Theorems [2, 3] which demonstrated a one-to-one correspondence between the charge density and the external potential and the number of electrons in the system. They also proved the existence of an universal functional of charge density: which uniquely defines the potential and the wavefunction; i.e. we can define $F[n(r)]$ such that

$$F[n(r)] = \langle\psi|T_e + V_{e-e}|\psi\rangle \tag{2.2}$$

We can therefore set up a variational framework in terms of the charge density as an alternative reformulation of Schrodinger's equation.

$$E_{V_{ext}}[n(r)] = F[n(r)] + \int V_{ext}(r)n(r)d^3r \geq E_0 \tag{2.3}$$

where minimizing the functional $E_{V_{ext}}[n(r)]$ gives us the ground state charge density ergo wavefunction[1].

[1] $\langle\psi|H|\psi\rangle = \langle\psi|T + V_{e-e} + v_{ext}|\psi\rangle = \int nv_{ext} + F[n]$

For computational ease, one can also use a proxy set of non-interacting electrons (Kohn-Sham electrons) such that it results in the same ground state charge density distribution. This decouples the $3N$-dimensional wavefunction to N 3-dimensional single electron orbital wavefunction. For the set of non-interacting pseudo-electrons, we can expand $F[n(r)]$ as

$$F[n(r)] = T_s[n(r)] + E_H[n(r)] + E_{xc}[n(r)] \tag{2.4}$$

where

- $T_s[n(r)]$ is the kinetic energy of non-interacting electrons

$$\sum_i^N -\frac{1}{2}\int \psi^*(r)\nabla^2\psi(r)dr \tag{2.5}$$

- $E_H[n(r)]$ is an average 'mean-field' effect felt by the electron from every other electron in the system.

$$\frac{1}{2}\int\int \frac{n(r_1)n(r_2)}{|r_1 - r_2|}dr_1 dr_2 \tag{2.6}$$

- $E_{xc}[n(r)]$ is the exchange-correlation function which includes everything else.

Now assuming we know the functional form of $E_{xc}[n(r)]$ is, we can apply Euler Lagrange equation to Eqn. 2.3 (along with enforcing constant N via Lagrange multipliers), we get

$$\begin{aligned} \delta\left(F[n(r)] + v_{ext}(r)n(r)dr - \mu\left(\int n(r)dr - N\right)\right) = 0 \\ \implies \frac{\delta F[n(r)]}{\delta n(r)} + v_{ext}(r) = \mu \end{aligned} \tag{2.7}$$

which gives us the Kohn-Sham equations

$$\left[-\frac{1}{2}\nabla^2 + v_H(r) + v_{xc}(r) + v_{ext}(r)\right]\psi_i(r) = H_{KS}\psi_i(r) = \epsilon_i\psi_i(r) \tag{2.8}$$

$$v_H(r) = \int \frac{n(r')}{|r - r'|}dr' \tag{2.9}$$

$$v_{xc} = \frac{\delta E_{xc}}{\delta n(r)} \tag{2.10}$$

$$n(r) = \sum_{i=1}^{N} |\psi_i(r)|^2 \tag{2.11}$$

This can be solved in an self-consistent iterative fashion until the solutions and trial do not change outside the limits of tolerance.

In practice, for periodic alloys, the wavefunction is expanded on a imaginary fourier basis up to a necessary wavelength cut-off necessary to reproduce the structure of the wavefunction. Since the

core electrons is strongly bound to the nucleus, it is customary to use Pseudo-Potentials which is an inaccurate description of the core electrons (which are considered frozen/screened in effect) but can reproduce the wave-form/energy of valence electrons to a good degree of accuracy. There are several flavors of pseudopotentials (Norm-Conserving, Ultrasoft etc.) but in this thesis we have used Projecter Augmented Wave (PAW). Further details of pseudopotential is beyond the scope of this document. However there is a rich body of literature if the reader is interested[4–7]. For the exchange-correlation energy, a popular functional form is the Local Density Approximation (LDA) where at every position in space for the exchange-correlation energy is the same as it would be for the uniform electron gas (UEG) having the same density as found at that position.

$$E_{xc}^{LDA}[n] = E_{x}^{LDA}[n] + E_{c}^{LDA}[n] \tag{2.12}$$

where

$$E_{x}^{LDA}[n] = C \int n^{4/3}(r) dr \tag{2.13}$$

and $E_{c}^{LDA}[n]$ are usually obtained by fitting to the results of accurate Quantum Monte Carlo (QMC) calculations of the UEG. However there also exist more general functionals which also include the gradient of the density.

$$E_{xc}^{GGA} = \int n(r)\epsilon_{xc}(n(r), |\nabla n(r)|) dr \tag{2.14}$$

Usually GGA functionals are constructed as corrections to the LDA functional

$$\epsilon_{x/c}^{GGA}[n] = \epsilon_{x/c}^{LDA}[n] + \Delta\epsilon_{x/c}\left[\frac{|\nabla n(r)|}{n^{4/3}(r)}\right] \tag{2.15}$$

For all DFT calculations in this thesis, we have used the Perdew-Burke-Ernzerhof (PBE) flavor of Exchange-Correlation Functional.

Another numerical issue is the discontinuity of the band structure at the fermi-level. To resolve this issue, the standard approach is to allow a 'smearing' to the discontinuous gap at the fermi-level (effectively adding a fictitious temperature), while not explicitly discussed, in all the work presented in this thesis, we have used Mathfessel-Paxson scheme of order 1 [8], where the broadening of the fermi-level is a linear function of the fictitious temperature.

One can also perform a first principles Molecular Dynamics instead of a relaxation using the same Kohn-Sham DFT formalism. For a given configuration average kinetic energy and initial ionic configuration, one can calculate the forces[2] on the nucleus, after an initial electronic ground state optimization according to

$$F_I = M_I \frac{d^2 R_I}{dt^2} = -\frac{dE(R)}{dR_I} = -\frac{d\left\langle \Psi_o | H_e(R) | \Psi_0 \right\rangle}{dR_I} \tag{2.16}$$

[2]Note that using Hellmann-Feynman theorem[9] forces can be calculated without recalculating the ground state wave function for small atomic displacements around the ground state

With the forces, the nuclei are moved. That constitutes one time-step of the simulation and continues in a minimize-move nuclei loop till the prescribed number of steps.

2.2 Cluster Variation Method

While DFT offers a feasible approximation to the Schrodinger's Wave equation; DFT calculations are primarily conducted at 0 K and it gives a suitable approximation to the ground state charge density and wave-functions only. It can be found in any standard statistical mechanics textbook[10] that at finite temperatures, in the classical limit, the probability of any configuration (microstate) with energy E_j in a canonical ensemble is given as

$$P_j = \frac{\exp\{(\beta E_j)\}}{\sum_i \exp\{(\beta E_i\})} \tag{2.17}$$

where $Z = \sum_i \exp\{(\beta E_i)\}$ is called the partition function is, $\beta = 1/k_B T$ where k_B is the Boltzmann constant and T is the temperature. The appropriate free energy to minimise would then be the Helmholtz Free Energy (F), defined as

$$F(N, V, T) = -\frac{1}{\beta} \log Z(N, V, T) \tag{2.18}$$

The partition function in principle contains all the necessary thermodynamic information about a system but the practical difficulty is at it's evaluation since it necessitates the summing over of a large number of states [3], where the assessment of each state has to be performed by DFT. Here we shall study the theory of Cluster Variation Method (CVM) which attempts at devising an analytical hamiltonian by expanding the energy as a linear combination of independent 'clusters'. Clusters which describe the structure in terms of the average distribution of independent 2-body, 3-body, ... n-body groups of atoms.

In the purview of alloys, the well-known Ising model can be generalized to multicomponent alloy hamiltonian following the CVM formalism originally introduced by Kikuchi and Colinet [11–15] and later reformulated by Barker[16] and again by Sanchez and co-workers[17–19]. In the CVM formalism, a structure is described as a vector of σ of length equal to the number of atoms in the structure. Therefore any lattice site (σ_i) can be labeled from 0 to $M_i - 1$, where M is the number of components in the system denoting the species which populate site i. We can the define clusters (α) as a collection of zero or more atoms (with the upper limit being the number of sites in the structure). A cluster is represented as a vector α of length equal to the number of points in the cluster, each component of which can hold values between 0 to ($M_i - 1$), 0 indicating the empty cluster[4] and everything else denote the functional dependence of the energy of cluster α on the

[3] consistent with thermodynamic constraints

[4] which plays the role of an concentration independent additive constant to the Hamiltonian

occupation σ_i of site i. We can then define Cluster functions[20, 21] - $\Gamma_\alpha(\sigma)$ as

$$\Gamma_\alpha(\sigma) = \prod_i \gamma_{\alpha_i, M_i}(\sigma_i) \tag{2.19}$$

where γ_{α_i, M_i} satisfies $\gamma_{0, M_i} = 1$ and the orthogonality condition

$$\frac{1}{M_i} \sum_{\sigma_i=0}^{M_i-1} \gamma_{\alpha_i, M_i}(\sigma_i)\gamma_{\beta_i, M_i}(\sigma_i) = \begin{cases} 1 & \text{if } \alpha_i = \beta_i \\ 0 & \text{otherwise} \end{cases} \tag{2.20}$$

It can be proven that any configuration dependent quantity can then be expanded in the basis of these cluster functions. If $G(\sigma)$ is one such function,

$$G(\sigma) = \sum_\alpha G_\alpha \Gamma_\alpha(\sigma) \tag{2.21}$$

Due to the orthogonality property, the coefficients, G_α can be obtained by taking inner product of G and the corresponding α.

$$\begin{aligned} \langle G(\sigma), \Gamma_\beta \rangle &= \left\langle \sum_\alpha G_\alpha \Gamma_\alpha, \Gamma_\beta \right\rangle \\ &= \sum_\alpha G_\alpha \langle \Gamma_\alpha, \Gamma_\beta \rangle \\ &= G_\beta \end{aligned} \tag{2.22}$$

Taking the ensemble average over all configurations we get,

$$\langle G \rangle = \sum_\alpha G_\alpha \langle \Gamma_\alpha \rangle \tag{2.23}$$

While the clusters go up to infinity, we can leverage the periodicity of the lattice to group clusters (and cluster functions) into groups of symmetrically equivalent clusters. We can re-write Eqn. 2.23 as

$$\begin{aligned} \langle G \rangle &= \sum_{\Omega(\alpha)} G_\alpha \sum_{i=1}^{N_\alpha} \langle \Gamma_{\alpha_i} \rangle \\ &= \sum_{\Omega(\alpha)} G_\alpha N_\alpha \langle \Gamma_{\alpha_i} \rangle \end{aligned} \tag{2.24}$$

Where $\Omega(\alpha)$ is the set of all clusters symmetrically equivalent to α[5] according to the space group of the crystal lattice. N_α is number of such orbits. For periodic structures of N atoms, the ensemble

[5] any one of such cluster is sufficient to represent all other clusters that are symmetrically related

average of G (for all possible σ) can then be defined as

$$g = \frac{\langle G \rangle}{N} = \sum_{\alpha} G_\alpha m_\alpha \langle \Gamma'_\alpha \rangle \tag{2.25}$$

Where α includes all symmetrically distinct clusters according to the space group symmetry of the lattice. m_α is the number of such symmetrically similar clusters present per unit-cell of the lattice.

To evaluate the cluster averages (aka cluster correlations[6]) in Eqn. 2.23, one can define Cluster configuration probabilities ρ_α which is the probability of finding a cluster of type α (equivalently any symmetric image) in a configuration σ as

$$\xi_\alpha = \langle \Gamma_\alpha \rangle = \langle \rho_\alpha, \Gamma_\alpha \rangle \tag{2.26}$$

Any particular cluster (α) probability can be also expanded as a function of correlations over all its sub-clusters (β).

$$\rho_\alpha = \frac{1}{2^{N_\alpha}} \sum_{\beta \subseteq \alpha} \xi_\beta \Gamma_\beta \tag{2.27}$$

In the event that the cluster probabilities are mutually independent, then the probability of any particular n-point cluster is the product of the probability of all it's sub-clusters[7]. However to correct for the mutual correlations of overlapping clusters, we define each cluster probability as a function of 'corrected' cluster probabilities of all it's sub-clusters such that

$$\begin{aligned} \rho_\alpha &= \prod_{\beta \subseteq \alpha} \widetilde{\rho}_\beta \\ \text{with } \widetilde{\rho}_\beta &= \frac{\rho_\beta}{\prod_{\gamma \subset \beta} \widetilde{\rho}_\gamma} \\ \text{and } \widetilde{\rho}_{\text{point}} &= \rho_{\text{point}} \end{aligned} \tag{2.28}$$

Note that the above illustration applies to all clusters α in the infinite cluster limit. We shall assume that beyond a certain cluster size α_m, (as $m \to \infty$) the clusters probabilities are uncorrelated, therefore

$$\widetilde{\rho}_\beta = 1 \quad \forall \ \beta > \alpha_{\text{m}} \tag{2.29}$$

The cluster probability for the maximal clusters is then given by

$$\widetilde{\rho}_{\alpha_{\text{m}}} = \frac{\rho_{\alpha_{\text{m}}}}{\prod_{\beta \subset \alpha_{\text{m}}} \widetilde{\rho}_\beta} \tag{2.30}$$

[6] it might seem a misnomer, but it can also be interpreted as 'how much' of the cluster is present in the structure, i.e. their cross-correlation.

[7] For eg. sub-clusters of ρ_{ABB} is a ternary alloy with elements A,B,C include $\rho_A, \rho_B, \rho_{BB}, \rho_{AB}$ (and maybe) ρ_{BA} but not ρ_C, ρ_{AC}, etc

and for any other cluster (all of which are sub-clusters of the maximal cluster) we have

$$\rho_\alpha = \prod_\alpha \left[\frac{\rho_\alpha}{\prod_{\beta \subset \alpha} \rho_\beta} \prod_{\gamma \subseteq \beta} \widetilde{\rho}_\gamma \right] \tag{2.31}$$

We therefore have a recurrence relationship

$$\begin{aligned} \rho_\alpha &= \prod_{\beta \subset \alpha} \rho_\beta^{k_\beta} \\ \text{where } k_\beta &= 1 - \sum_{\beta \subset \alpha} k_\alpha \\ \text{and } k_{\alpha_m} &= 1 \end{aligned} \tag{2.32}$$

where k's are the known as the Kikuchi-Barker (KB) coefficients. The KB recursive relationship in Eqn. 2.32 can be intuited by the consideration that while the cluster term should appears once when we consider the correction on that clusters (in the numerator). But it is repeated again each time we expand another cluster of which the current cluster is a sub-cluster (in the denominator). From this point onwards, we shall use the notation ξ for correlations instead of the $\langle \Gamma \rangle$ since we do not intend to perpetuate a possible confusion of $\langle \cdot \rangle$ and $\langle \cdot, \cdot \rangle$ - the former is an average which we shall henceforth denote as ξ and the latter is the notation for an inner-product.

In the above notation, the Helmholtz Free Energy associated to the Canonical Ensemble (fixed N,V,T) assumes the functional form as

$$F = \sum_\alpha \underbrace{\left[\rho_\alpha E(\rho_\alpha) + k_\mathrm{B} T \rho_\alpha \log \rho_\alpha \right]}_{U - TS} \tag{2.33}$$

such that $\sum_{\beta \subseteq \alpha} \rho_\beta = 1 \ \forall \ \alpha$

The second part of the free energy function in Eqn. 2.33 can be reformulated as

$$\begin{aligned} S &= -k_\mathrm{B} \sum_\alpha \rho_\alpha \log \left(\prod_{\beta \subseteq \alpha} \rho_\beta^{k_\beta} \right) \\ &= -k_\mathrm{B} \sum_\alpha \rho_\alpha \sum_{\beta \subseteq \alpha} k_\beta \log \rho_\beta \end{aligned} \tag{2.34}$$

in the infinite cluster limit

$$S = -k_\mathrm{B} \sum_\alpha k_\alpha \rho_\alpha \log \rho_\alpha \tag{2.35}$$

Applying the similar grouping of symmetrically equivalent clusters configurations (according to the

point group symmetry of the cluster) we can re-rewite Eqn. 2.35 in per unit term of the unit cell as

$$S = -k_{\mathrm{B}} \sum_{\Omega(\rho_\alpha)} k_\alpha N_\alpha \rho_\alpha \log \rho_\alpha \tag{2.36}$$

where the summation is taken for all symmetrically distinct cluster configurations. N_α being the number of symmetrically equivalent configuration of each cluster α. The value of entropy per unit cell is then

$$s = -k_{\mathrm{B}} \sum_{\alpha} k_\alpha \frac{N_\alpha}{N} \rho_\alpha \log \rho_\alpha = -k_{\mathrm{B}} \sum_{\alpha} k_\alpha w_\alpha \rho_\alpha \log \rho_\alpha \tag{2.37}$$

Similar to cluster multiplicities, we define $N_\alpha/N = w_\alpha$ as cluster configuration multiplicities. Note that α now includes only symmetrically distinct cluster configurations.

Expanding the cluster configuration probabilities in the cluster function basis and then applying symmetry grouping, we get

$$\rho_\alpha = \frac{1}{2^{N_\alpha}} \sum_{\beta \subseteq \alpha} \xi_\beta \Gamma_\beta \tag{2.38}$$

Summing over only the symmetrically distinct clusters, we can write

$$\rho_\alpha = \frac{1}{2^{N_\alpha}} \sum_{\Omega(\rho_\beta) \subseteq \rho_\alpha} \xi_\beta \sum_{\gamma \in \Omega(\beta), \gamma \in \alpha} \Gamma_\gamma \tag{2.39}$$

We could re-write the second sum as

$$\nu_{\beta\alpha} = \frac{1}{2^{N_\alpha}} \sum_{\gamma \in \Omega(\beta), \gamma \in \alpha} \Gamma_\gamma \tag{2.40}$$

Eqn. 2.40 define the terms of a matrix called the V-matrix. It is worth mentioning that the cluster multiplicities, cluster configuration multiplicities, V-matrix and the KB coefficients are all functions of the underlying lattice and the choice of cluster functions; therefore any numerical algorithm needs to calculate this only once during the optimization.

While the cluster sum still extends up to infinity we can now invoke the Connoly-Williams (CW) approximation and truncate the clusters up to a maximal size[20–22]. We can then fit the ground state formation enthalpies of select structures computed using DFT in accordance to the clusters expansion formalism to derive the independent energetic contribution V_α (Effective Cluster Interaction (ECI)) of each independent cluster following the equation

$$\langle H \rangle = \sum_{\alpha}^{\alpha_m} m_a V_\alpha \xi_\alpha \tag{2.41}$$

While the Cluster Expansion (CE)[8] is systematically improvable by increasing the size of the maximal cluster, it is extremely sensitive to the choice of clusters and the accuracy of the ground state structure estimates. In practice, since the true ground state structures are unknown apriori, one has to then enumerate several structures in the composition regime of the alloy to perform a least squares fit. Different choice of maximal clusters model different types of interactions between the constituents, hence the choice is very system dependent. Since the ground state structures are mere estimates, it is easy to over-fit the CE model and therefore one must also incorporate regularization/cross-validation strategies to choose the optimal set of cluster with best generalization among the data-points.

The Helmholtz-Free energy function in terms of cluster correlations up to a maximal cluster is therefore given by

$$F = \sum_{\alpha}^{\alpha_m} m_\alpha V_\alpha \xi_\alpha + k_{\mathrm{B}} T \sum_{\alpha}^{\alpha_m} w_\alpha k_\alpha \left(\sum_{\beta \subseteq \alpha} v_{\beta\alpha} \xi_\alpha \right) \log \left(\sum_{\beta \subseteq \alpha} v_{\beta\alpha} \xi_\alpha \right) \tag{2.42}$$

For a given alloy system Eqn. 2.42 can be minimized in a constrained optimization scheme - constraining the ρ's to be bound between $[0, 1]$ and optionally fixing 1-point correlations to fix composition. This delivers the minimal Free energy and equilibrium cluster correlations/cluster configuration at a given temperature and ECIs.

2.3 CALPHAD Formalism

The CVM methodology allow for a systematically improvable hamiltonian construction using DFT calculations as a reference. While CVM accuracy positively correlates with increasing the size of the maximal cluster, the number of sub-clusters scale exponentially and this poses a computational challenge for quick prototyping. Here we introduce the CALPHAD (CALculation of PHAse Diagrams)[23–25] method which is another parametric model to predict alloy free energies. In contrast to CVM, CALPHAD linearizes the energetic contribution of the system in terms of increasing orders of interaction between site fractions (equivalent to interactions between point clusters only in CVM[9]. As the name suggests, this method is particularly of choice for calculating phase equilibrium possibly due to the convenience of including both first-principles as well as experimental data into one framework.

The CALPHAD method is a generalization of the regular solid solution model which assumes the total enthalpy of an alloy as a sum of mixtures[10] of it's constituents with additive correction factors

[8] the enthalpy function of CVM

[9] In CVM we have $F(x) = \arg\min f(1\mathrm{pt}, 2\mathrm{pt}, \cdots))$, but in CALPHAD w have $F(x) = f(1\mathrm{pt})$. Every other interaction has been ascertained outside the model

[10] with respect to a certain reference state. The reference state is not mentioned but is assumed to be present unless throughout the discussion

for mutual interaction of the constituents with increasing orders of interaction. The underlying lattice is described in the sub-lattice model as per the Compound Energy Formalism (CEF)[26, 27] which is a suitable universal descriptor for all material types - gases, defect structures, magnetic structures, stoichiometric and substitutional solutions alike. In CEF, each sub-lattice has a_s sites[11] and the composition of a site in this model is given by y_{is}^{α} where i is the component (element or a compound) in the s sub-lattice of the α phase. The moles of any element A can be then calculated as

$$M_A^{\alpha} = \sum_s a_s^{\alpha} \sum_i b_{Ai} y_{is}^{\alpha} \tag{2.43}$$

where b_{Ai} is the stoichiometric coefficients of element A is component i[12]. By definition, sum of fractions for each constituent in any sub-lattice is equal to 1 ($\sum_i y_{is}^{\alpha} = 1$). The mole fraction of element A in phase α is therefore

$$x_A^{\alpha} = \frac{M_A^{\alpha}}{\sum_B M_B^{\alpha}} = \frac{M_A^{\alpha}}{M^{\alpha}} \tag{2.44}$$

Therefore total moles of A (and mole fraction of A) in the system with multiple phases,

$$N_A = \sum_{\alpha} \aleph^{\alpha} M_A^{\alpha} \tag{2.45}$$

$$x_A = \frac{N_A}{N} = \frac{\sum_s a_s^{\alpha} \sum_i b_{Ai} y_{is}^{\alpha}}{\sum_A \sum_s a_s^{\alpha} \sum_i b_{Ai} y_{is}^{\alpha}} \tag{2.46}$$

where $\aleph^{\alpha}$ is the number of moles of formula units of phase α

The Molar Gibbs Free Energy (G) relates the chemical potential (μ_A) of an element with the number of moles per formula unit of phase α (M_A^{α}). In general, we can define G^{α} as a function of $T, P, M_A^{\alpha}, \ldots$ as

$$\begin{aligned} G_M^{\alpha} &= \sum_A M_A^{\alpha} \mu_A \\ \text{where } \mu_A &= \left(\frac{\partial G^{\alpha}}{\partial M_A^{\alpha}} \right)_{T,P,M_{B\neq A}^{\alpha}} = \left(\frac{\partial G^{\beta}}{\partial M_A^{\beta}} \right)_{T,P,M_{B\neq A}^{\beta}} = \cdots \quad \text{(for all stable phases)} \end{aligned} \tag{2.47}$$

However since chemical potential of each species for all phases is not known easily, we shall instead first express G_M^{α} as

$$G_M^{\alpha}(T, P, y_{is}^{\alpha}) = {}^{\text{srf}} G_M^{\alpha} - T^{\text{cfg}} S_M^{\alpha} + {}^{E} G_M^{\alpha} \tag{2.48}$$

[11] reduced to the smallest integer ratio of all sites

[12] unless otherwise stated, in this thesis all components are pure elements

where

$$ {}^{\text{srf}}G_M^\alpha = \sum_I \left(\prod_I y_{is}^\alpha \right) G_I^{o\alpha}(T,P) \tag{2.49} $$

$$ {}^{\text{cfg}}S_M^\alpha = RT \sum_s a_s^\alpha \sum_i y_{is}^\alpha \log y_{is}^\alpha \tag{2.50} $$

$$ {}^{E}G_M^\alpha = \sum_J L_J^\alpha(T,P,y_{is}^\alpha) \tag{2.51} $$

Here ${}^{\text{srf}}G_M^\alpha$ represent the surface of reference which is a linear sum of the end-members of phase α where a end-member is defined as the structure with each sub-lattice being completely occupied by only one of the constituents. $G_I^{o\alpha}(T,P)$ being the Gibbs free energy of formation of the structure from it's constituents in the standard reference state.

In the configurational entropy term, random mixing is assumed within each lattice, however constituents are constrained to their respective sub-lattice thus avoiding cross-sublattice exchanges.

${}^{E}G_M^\alpha$ represent a series of non-linear interaction terms between the constituents of the form

$$ \sum_{l=0}^{L} L_{ij}^l(T,P) \left(\prod y_{js}^\alpha \right) (y_{js} - y_{is})^l \tag{2.52} $$

where $L_{ij}^l(T,P)$ are known as the Redlich-Kister (RK) Parameters.

The functions $G_I^{o\alpha}(T,P)$ and $L_{ij}^l(T,P)$ can be then fitted to known experimental/computational results for different alloy compositions in the system and together with the phase description can be packaged in a Thermodynamic Database File (TDB) that can be used for thermodynamic analysis of equilibrium site fraction distribution.

2.4 Special Quasirandom Structures

It is a computational challenge to perform DFT calculations on systems over $\sim$ 200 atoms. While periodic boundary conditions remove the effects of surfaces, the small cell size introduce artificial order in the periodic images which may deviate from the truly disordered structure even if the sites in the cell was populated with a robust random number generator. To circumvent the statistical correlations in an insufficiently large periodic cell($\propto 1/\sqrt{N}$), we describe a small cell approximation of the completely disordered structure using the Special Quasirandom Structure (SQS) formalism introduced by Zunger[28] and implemented by Van de Walle et al[29].

For a truly disordered set of (symmetrically distinct) clusters, the cluster probability of a n-body

cluster are independent of the cluster probability of it's sub-clusters.

$$\begin{aligned} \rho_\alpha &= \prod_{\beta \subset \alpha} \rho_\beta \\ \implies \frac{1}{2^{N_\alpha}} \sum_{\beta \subseteq \alpha} \xi_\beta \Gamma_\beta &= \prod_{\beta \subset \alpha} \frac{1}{2^{N_\delta}} \sum_{\delta \subseteq \beta} \xi_\delta \Gamma_\delta \end{aligned} \tag{2.53}$$

Gathering the coefficients of the common cluster correlations on both sides of the equation and using the identity $N_\alpha = \sum_{\beta \subset \alpha} N_\beta$, we get the following constraint that is satisfied by the correlations of a completely disordered structure,

$$\xi_\alpha = \prod_{\beta \subset \alpha} \xi_\beta \tag{2.54}$$

Since the point correlations are known for a fixed composition, the higher order correlations for a completely disordered structure can be obtained by recursively applying Eqn. 2.54 repeatedly with increasing size of cluster.

To derive the optimal structure within the specified size-cutoff once has to first decide on the set of clusters. Upon the choice of clusters, one starts with a randomly populated cell of the proper stoichiometry and symmetry. An objective function representing the deviation between the current structure and the truly disordered structure in the correlation space can then be constructed as

$$Q = -\omega L + \sum_\alpha |\Delta\xi| \tag{2.55}$$

where $\Delta\xi = \xi_{\text{curr}} - \xi_{\text{disordered}}$. L is the radius of the maximum cluster below which we would want to exactly match the structure to the disordered correlations with a hyper-parameter ω. Since locality is a feature of alloy hamiltonians such a preference to smaller size cluster expectedly improves the approximation for energy calculations. The structure optimization is then performed in a Monte Carlo scheme incrementally swapping atoms to minimise Q (Eqn. 2.55) while keeping the overall composition and lattice fixed.

2.5 Embedded Atom Method Classical Inter-atomic Force-Fields

We now discuss the rudiments of yet another structure $\leftrightarrow$ energy map in the form of a classical inter-atomic class potentials known as the Embedded Atom Method. While molecular dynamics (MD) can be performed purely from first-principles (see section 2.1), the length and time scales required to estimate accurate dynamic/static averages makes it prohibitively expensive. EAM potentials are particularly well-suited for large scale MD simulations both in the number of atoms and time scales for it's ability to scale over the number of particles and quick evaluation of forces (gradients

of energy). While CVM and CALPHAD aim at calculating thermodynamic variables by ensemble-averages, EAM potential driven classical MD simulations evaluate the same by time-averaging the evolution of the system[13].

Contrary to ab-initio MD which consider the quantum nature of particles, Classical MD instead simulate dynamics with a classical approach of particles in a box evolving according to Newton's Laws of motion. The forces in such MD is obtained from classical potential energy force-fields which are purely functions of the spatial coordinates of the atoms. These force-fields are analytic approximations of the underlying quantum system, and while this could be applied to scale simulations with millions of atoms over long time scales, it lacks in generality and are accurate only in the phase space on which it was fit on.

Owing to the lack of transfer-ability, classical analytical potential are often designed for a particular application and preferentially reproduce certain properties well over others. In particular for molecules and chemical reactions, where intra-molecular bond breaking-forming and angular dependence is an important feature, polarizable and reactive force-fields such as The PIPF (polarizable intermolecular potential function)[31], DRF90[32], AMOEBA[33], CHARMM[34, 35], AMBER[36], OPLS[37], GROMOS[38], ReaxFF[39] are the most popular ones. All have its characteristic pros and cons and hence are best suited for specific types of materials or applications. More information about inter-atomic potentials can be found in ample literature [40–42].

For non-polarizing, non-reacting periodic metallic alloys however, historically the simplest form of potentials as a function of pair-wise distance of atoms is often used for computational efficiency. Unfortunately pair potentials are volume agnostic and have to augmented with volume dependent terms. In cases when volumes are difficult to define such as studies involving surfaces - defects, relaxations, fracture calculations etc., simple pair potentials approach fails. It can also be demonstrated that by construction, pair potentials give zero Cauchy Pressure ($C_{12} - C_{44} = 0$). The deficiency can be attributed to the fact that pair potentials do not represent many-body effects and effects that are NOT the function of local coordination particularly for transition metals. Here we shall discuss the Embedded Atom Method[43–45] which accounts for total energy as an effective medium interaction of all atoms embedded in a pool of electrons with all other atoms. It is computationally feasible, has close analogies to Density Function Theories (DFT), and evades the volume problem by an effective medium interaction which is a function of the charge density that can always be defined irrespective of system geometry.

The roots of EAM are in the Hohenberg and Kohn [2] theorems on the equivalence of potential and charge density. In an alloy, if any one atom is considered as an 'impurity' in the medium of other 'host' atoms, then the unperturbed 'host' atom charge density defines it's potential. The extended proposition is that upon embedding the 'impurity atoms', the energetic cost of the embedding is a function of the position and type of the 'impurity' atom but only the charge density of the

[13] For an ergodic[30] system in equilibrium, it should lead to the same solutions

'unperturbed' host density [46].

$$E_{Z,r} = F_{Z,r}(\rho) \tag{2.56}$$

We can then consider every atom as an impurity in a medium including all other atoms and the total energy is then given by

$$E = \sum_i F_{Z,r}(\rho) = \sum_i F_i[\rho_{\bar{i}}(r)] \tag{2.57}$$

$\rho_{\bar{i}}(r)$ is the charge density at a position r without atom i. Since the exact form of F is not known, the common assumption to take is to assume that the charge density is locally uniform. However in a general case,

$$\rho_{\bar{i}}(r) = \sum_{j \neq i} \rho_{s_j}(r) \tag{2.58}$$

Here $\rho_{s_j}(r)$ can be reasoned as measure for the atomic density in the vicinity of atom j. Therefore, it should be expected to be well represented by any monotonically decreasing oscillatory function. The embedding energy method could also be deemed as a generalized *fixed volume* pair potential, such that the *volume* is now a function per atom and not of the whole system. This resolves the previously mentioned point about the disability of pair potentials to handle surfaces and defects where volume of a system is ill-defined. $\rho_{s_j}(r)$'s are however is purely a function of distances and is therefore agnostic of angular dependencies.

Nonetheless, this spherical symmetry, the non-linear nature of $F_i[\rho_{\bar{i}}(r)]$ account for many-body interactions beyond pairs. In this many-body perspective; more the number of bonds, weaker is every new bond. Therefore adding one more bond increases the total bonding energy while at the same time reducing the average energy per bond. From this view-point, each $\rho_{s_j}(r)$ is a bond-sensor while total F is a measure of the bond-order for the central atom. In order to adhere to this physically motivated inverse relationship of bond-order and bond length (bond weakening)[14], the one requirement on F is that it has a positive curvature $\left(\frac{\partial^2 F}{\partial \rho^2} > 0\right)$ everywhere. In the special case where the charge density is globally equivalent to that of a homogeneous electron gas distribution, F is a linear function $\left(\frac{\partial^2 F}{\partial \rho^2} = 0\right)$ and is equivalent to another pair function. This is consistent with such cases being true for chemically inert species. The Cauchy relationship also holds true in such special cases where the equilibrium curvature of F is zero[43].

While the curvature of F has a significance in the many-body interactions of EAM, the slope does not. It can be proven that changing the slope is equivalent to changing the pair potential[47, Chapter 4] which is usually added to account for the core-core overlap. Hence for solids in equilibrium, there exists a balance between expansion (or contraction) forces by the embedding function and the contraction (or expansion) forces due to pair-wise interactions. The resulting total energy is given by

$$E = \frac{1}{2} \sum_i \phi_{s_i,s_j}(r_{ij}) + \sum_i F_{s_i}(\rho_{\bar{i}}) \tag{2.59}$$

[14] this concept is also used in vibrational entropy calculation is solid, but discussion about it is beyond the scope of this thesis

Upon further simplifying $\rho_{\bar{i}}$ as a sum of atomic densities of all constituent atoms at site i, then $\rho_{\bar{i}} = \sum_{j \neq i} \rho_{s_j}(r_{ij})$, the complete EAM equation is therefore

$$E = \frac{1}{2} \sum_i \phi_{s_i, s_j}(r_{ij}) + \sum_i F_{s_i} \left(\sum_{j \neq i} \rho_{s_{\bar{j}}}(r_{ij}) \right) \tag{2.60}$$

There is an implicit double counting in the EAM formalism in the sense of each atom being hosted by other sites and itself acting as a host[48]. This is reconciled by scaling[15] ρ's such that Eqn. 2.60 is invariant, but Eqn. 2.56 is not.

$$\begin{aligned} \rho'_{\bar{i}}(r) &= s_{s_i} \rho_{\bar{i}}(r) \\ F_{s_i}(\rho'_{\bar{i}}(r)) &= F_{s_i}(\rho'_{\bar{i}}(r)/s_{s_i}) \end{aligned} \tag{2.61}$$

A common choice of the pair potential is the Morse Potential[49], which is an empirical function originally designed to capture the motion of atoms in a diatomic structure and is suitable for modelling pair interaction as well. It has a functional form,

$$E = D_r[(1 - \exp\{(-a(r - r_o))\})^2 - 1] \tag{2.62}$$

The atomic density at a point i from all atoms j is given by $\rho_{\bar{i}} = \sum_{j \neq i} \rho_{s_j}(r_{ij})$ where f is represented using an oscillatory function[50]

$$\rho_{s_j}(r_{ij}) = \frac{1 + a_1 \cos(\alpha r_{ij} + \varphi)}{r_{ij}^{\beta}} \tag{2.63}$$

For the embedding function, an universal functional form can be established by scaling the energy with respect to the equilibrium binding energy ($E^* = E/E_o$) and the equilibrium spacing ($a^* = (a - a_o)/\gamma$. The scaling of the equilibrium spacing scales the electron density as $\rho^* = \rho \exp\{(a^*)\} \rightarrow \rho* = \left(\frac{\rho}{\rho_o}\right)^{\gamma}$, such that the universal functional form of binding energy-charge density can be described as:[51]

$$E = E_o \left[1 - \gamma \log\left(\frac{\rho}{\rho_o}\right)\right] \left(\frac{\rho}{\rho_o}\right)^{\gamma} + E_1 \frac{\rho}{\rho_0} \tag{2.64}$$

In this work we ignore this scaling explicitly and represent the embedding energy function simply as

$$E = E_o \left[1 - \gamma \log \rho\right] \rho^{\gamma} + E_1 \rho \tag{2.65}$$

In an n element alloy, there are $\binom{n+1}{2} = \frac{n(n+1)}{2}$ pair potentials, n electron density function and n embedding functions. Based on the force matching technique by Ercolessi and Adams[52–54], once a

[15] note that the order of application of the scaling matters

choice of functions have been made, the coefficients of the function can be fitted to energy calculated from DFT by minimizing the objective function

$$Z(\alpha) = Z_F(\alpha) + Z_C(\alpha) \tag{2.66}$$

with

$$Z_F(\alpha) = \left(3\sum_{k=1}^{M} N_k\right)^{-1} \sum_{k=1}^{M}\sum_{i=1}^{N_k} |F_{ki}(\alpha) - F_{ki}^o|^2 \tag{2.67}$$

$$Z_C(\alpha) = \sum_{r=1}^{N_c} W_r[A_r(\alpha) - A_r^o]^2 \tag{2.68}$$

M is the number of reference configurations available, N_k is the number of atoms in the kth configuration, α is the set of parameters defining the potential. $F_{ki}(\alpha)$ is the force predicted by the potential at the current parameter set-up of α where F_{ki}^o is the reference force. One can specify additional information such as as Energy and Stresses as N_c terms. $A_r(\alpha)$ and A_r^o have the equivalent meaning in terms of the additional information. Based on the application, the weights of the additional information (W_r) are chosen as a hyper-parameter. The optimal parameters for the potential is thus obtained by minimizing Eqn. 2.66.

References

1. Schrödinger, E. An Undulatory Theory of the Mechanics of Atoms and Molecules. *Phys. Rev.* **28,** 1049–1070 (6 1926).
2. Hohenberg, P. & Kohn, W. Inhomogeneous Electron Gas. *Phys. Rev.* **136,** B864–B871 (3B 1964).
3. Kohn, W. & Sham, L. J. Self-Consistent Equations Including Exchange and Correlation Effects. *Phys. Rev.* **140,** A1133–A1138 (1965).
4. Blöchl, P. E. Projector augmented-wave method. *Phys. Rev. B* **50,** 17953–17979 (1994).
5. Kresse, G. & Furthmüller, J. Efficiency of ab-initio total energy calculations for metals and semiconductors using a plane-wave basis set. *Computational Materials Science* **6,** 15–50 (1996).
6. Kresse, G. & Furthmüller, J. Efficient iterative schemes for ab initio total-energy calculations using a plane-wave basis set. *Phys. Rev. B* **54,** 11169–11186 (1996).
7. Kresse, G. & Joubert, D. From ultrasoft pseudopotentials to the projector augmented-wave method. *Phys. Rev. B* **59,** 1758–1775 (3 1999).
8. Methfessel, M. & Paxton, A. T. High-precision sampling for Brillouin-zone integration in metals. *Phys. Rev. B* **40,** 3616–3621 (1989).
9. Feynman, R. P. Forces in Molecules. *Physical Review* **56,** 340–343 (1939).

10. McQuarrie, D. A. *Statistical Mechanics* Paperback (VIVA, 2015).

11. Kikuchi, R. CVM Entropy Algebra. *Progress of Theoretical Physics Supplement* **115,** 1–26 (1994).

12. Kikuchi, R. Second Hessian determinant as the criterion for order (first or second) of phase transition. *Physica A: Statistical Mechanics and its Applications* **142,** 321–341 (1987).

13. Kikuchi, R. A Theory of Cooperative Phenomena. *Physical Review* **81,** 988–1003 (1951).

14. Colinet, C. Applications of the cluster variation method to empirical phase diagram calculations. *Calphad* **25,** 607–623 (2001).

15. Colinet, C., Inden, G. & Kikuchi, R. CVM calculation of the phase diagram of b.c.c. FeCoAl. *Acta Metallurgica et Materialia* **41,** 1109–1118 (1993).

16. Barker, J. A. & Guggenheim, E. A. Methods of approximation in the theory of regular mixtures. *Proceedings of the Royal Society of London. Series A. Mathematical and Physical Sciences* **216,** 45–56 (1953).

17. Sanchez, J. M. Cluster expansions and the configurational energy of alloys. *Phys. Rev. B* **48,** 14013–14015 (1993).

18. Sanchez, J. M., Ducastelle, F. & Gratias, D. Generalized cluster description of multicomponent systems. *Physica A: Statistical Mechanics and its Applications* **128,** 334–350 (1984).

19. Sanchez, J. M. Cluster expansion and the configurational theory of alloys. *Phys. Rev. B* **81,** 224202 (2010).

20. Asta, M., Wolverton, C., de Fontaine, D. & Dreyssé, H. Effective cluster interactions from cluster-variation formalism. I. *Phys. Rev. B* **44,** 4907–4913 (1991).

21. Wolverton, C., Asta, M., Dreyssé, H. & de Fontaine, D. Effective cluster interactions from cluster-variation formalism. II. *Phys. Rev. B* **44,** 4914–4924 (1991).

22. Connolly, J. W. D. & Williams, A. R. Density-functional theory applied to phase transformations in transition-metal alloys. *Phys. Rev. B* **27,** 5169–5172 (1983).

23. Spencer, P. J. A brief history of CALPHAD. *Calphad* **32,** 1–8 (2008).

24. Kaufman, L. Computational Thermodynamics and materials design. *Calphad* **25,** 141–161 (2001).

25. Sundman, B., Lukas, H. & Fries, S. *Computational thermodynamics: the Calphad method* (Cambridge university press Cambridge, 2007).

26. Hillert, M. The compound energy formalism. *Journal of Alloys and Compounds* **320,** 161–176 (2001).

27. Hillert, M. Some viewpoints on the use of a computer for calculating phase diagrams. *Physica B+C* **103,** 31–40 (1981).

28. Zunger, A., Wei, S.-H., Ferreira, L. G. & Bernard, J. E. Special quasirandom structures. *Physical Review Letters* **65,** 353–356 (1990).

29. Van de Walle, A., Tiwary, P., de Jong, M., Olmsted, D. L., Asta, M., Dick, A., *et al.* Efficient stochastic generation of special quasirandom structures. *Calphad* **42,** 13–18 (2013).

30. Walters, P. *An Introduction to Ergodic Theory (Graduate Texts in Mathematics, 79)* Paperback, 259 (Springer, Oct. 6, 2000).

31. Gao, J., Habibollazadeh, D. & Shao, L. A Polarizable Intermolecular Potential Function for Simulation of Liquid Alcohols. *J. Phys. Chem.* **99,** 16460–16467 (1995).

32. Swart, M. & van Duijnen, P. DRF90: a polarizable force field. *Molecular Simulation* **32,** 471–484 (2006).

33. Ponder, J. W., Wu, C., Ren, P., Pande, V. S., Chodera, J. D., Schnieders, M. J., *et al.* Current Status of the AMOEBA Polarizable Force Field. *J. Phys. Chem. B* **114,** 2549–2564 (2010).

34. Patel, S. & Brooks, C. L. CHARMM fluctuating charge force field for proteins: I parameterization and application to bulk organic liquid simulations. *J Comput Chem* **25,** 1–15 (2004).

35. Lamoureux, G. & Roux, B. Modeling induced polarization with classical Drude oscillators: Theory and molecular dynamics simulation algorithm. *J. Chem. Phys.* **119,** 3025–3039 (2003).

36. Wang, Z.-X., Zhang, W., Wu, C., Lei, H., Cieplak, P. & Duan, Y. Strike a balance: optimization of backbone torsion parameters of AMBER polarizable force field for simulations of proteins and peptides. *J Comput Chem* **27,** 781–790 (2006).

37. Jorgensen, W. L., Jensen, K. P. & Alexandrova, A. N. Polarization Effects for Hydrogen-Bonded Complexes of Substituted Phenols with Water and Chloride Ion. *J Chem Theory Comput* **3,** 1987–1992 (2007).

38. Geerke, D. P. & van Gunsteren, W. F. On the Calculation of Atomic Forces in Classical Simulation Using the Charge-on-Spring Method To Explicitly Treat Electronic Polarization. *J Chem Theory Comput* **3,** 2128–2137 (2007).

39. Senftle, T. P., Hong, S., Islam, M. M., Kylasa, S. B., Zheng, Y., Shin, Y. K., *et al.* The ReaxFF reactive force-field: development, applications and future directions. *npj Computational Materials* **2,** 15011 (2016).

40. Chen, J. & Houk, K. N. Molecular Modeling: Principles and Applications By Andrew R. Leach. Addison Wesley Longman Limited: Essex, England, 1996. 595 pp. @@isbn 0-582-23933-8. *J. Chem. Inf. Comput. Sci.* **38,** 939–939 (1998).

41. Schlick, T. *Molecular Modeling and Simulation: An Interdisciplinary Guide: An Interdisciplinary Guide* (Springer New York, New York, NY, 2010).

42. Maple, J. R., Hwang, M.-J., Stockfisch, T. P., Dinur, U., Waldman, M., Ewig, C. S., *et al.* Derivation of class II force fields. I. Methodology and quantum force field for the alkyl functional group and alkane molecules. *Journal of Computational Chemistry* **15,** 162–182 (1994).

43. Daw, M. S. & Baskes, M. I. Embedded-atom method: Derivation and application to impurities, surfaces, and other defects in metals. *Phys. Rev. B* **29,** 6443–6453 (1984).

44. Daw, M. S. & Baskes, M. I. Semiempirical, Quantum Mechanical Calculation of Hydrogen Embrittlement in Metals. *Phys. Rev. Lett.* **50,** 1285–1288 (1983).

45. Foiles, S. M., Baskes, M. I. & Daw, M. S. Embedded-atom-method functions for the fcc metals Cu, Ag, Au, Ni, Pd, Pt, and their alloys. *Phys. Rev. B* **33,** 7983–7991 (1986).

46. Puska, M. J., Nieminen, R. M. & Manninen, M. Atoms embedded in an electron gas: Immersion energies. *Physical Review B* **24,** 3037–3047 (1981).

47. Paufler, P. J. H. Westbrook, R. L. Fleischer (eds.). Intermetallic Compounds. Principles and Practice. *Crystal Research and Technology* **30,** 920–920 (1995).

48. Manninen, M. Interatomic interactions in solids: An effective-medium approach. *Physical Review B* **34,** 8486–8495 (1986).

49. Morse, P. M. Diatomic Molecules According to the Wave Mechanics. II. Vibrational Levels. *Phys. Rev.* **34,** 57–64 (1929).

50. Chantasiriwan, S. & Milstein, F. Higher-order elasticity of cubic metals in the embedded-atom method. *Phys. Rev. B* **53,** 14080–14088 (1996).

51. Banerjea, A. & Smith, J. R. Origins of the universal binding-energy relation. *Phys. Rev. B* **37,** 6632–6645 (1988).

52. Ercolessi, F., Tosatti, E. & Parrinello, M. Au (100) Surface Reconstruction. *Phys. Rev. Lett.* **57,** 719–722 (1986).

53. Ercolessi, F. & Adams, J. B. Interatomic Potentials from First-Principles Calculations: The Force-Matching Method. *EPL (Europhysics Letters)* **26,** 583–588 (1994).

54. Ercolessi, F., Parrinello, M. & Tosatti, E. Simulation of gold in the glue model. *Philosophical Magazine A* (2006).

Chapter 3

First Principles assessment of Iridium-Ruthenium Binary Phase Diagram

3.1 Introduction

Phase diagram determination is a well-documented bottleneck for novel materials discovery and design [1]. To address this, high-throughput calculation tools [2–4] have been designed to provide robust and automated end-to-end first-principles pipelines to generate phase stability information. However, traditional approaches in this field tend to focus solely on ordered stoichiometric phases, which entails important limitations [5]. First, real engineering alloys tend to specifically exploit deviations from stoichiometry to optimize materials properties. Second, a focus on ordered phases essentially implies that only phase stability at absolute zero is considered[1]. This focus has the undesirable side-effect that it generally predicts a wide range of possible ordered ground states that exaggerate the number of phases that would typically observed at commonly accessible temperatures.

In this work, we seek to address this last shortcoming by providing a simple way to verify whether an ordered phase predicted to be stable at absolute zero, based on high-throughput calculations, is indeed a phase that should be considered in a phase diagram covering room temperature and above. Part of the solution is to leverage the CALculation of PHAse Diagrams (CALPHAD) [7–9] framework and the Compound Energy Formalism (CEF) [10–12]. Ab-initio electronic structure methods [13, 14] are routinely included to augment experimental input in CALPHAD assessments, [15–17] but these efforts typically focus on ordered phases. The inclusion of ab initio data for nonstoichiometric

[1] although phonon contributions are at least being increasingly considered in high-throughput settings [6]

phases is less frequently attempted [18–21] but when it is, it typically relies on the cluster expansion formalism, which is not easily amenable to a high-throughput treatment.

Methods that are more amenable to a purely computational high-throughput treatment in the construction of accurate phase diagrams at nonzero could revolutionize the process of new materials screening and discovery in an unprecedented manner [22–24]. In this work we demonstrate the effectiveness of a software pipeline that can model the thermodynamics of an alloy system by fitting the coefficients of a polynomial expression representing excess solution free energies in the CALPHAD formalism to a set of distinct ab-initio calculation [25]. To expedite the ab-initio calculations, this framework relies on the concept of Special Quasirandom Structure (SQS)[26].

An SQS is a representation of a completely disordered alloy that attempts to mimic the short-range correlations functions of a *true* completely disordered material in a small periodic simulation cell. The code [25] generates select compositions which are a function of the phase being modeled and the number of components from a SQS database. A key distinguishing feature of this software system is that it offers an independent control over the different sublattice compositions (i.e., site fractions) when exploring structure space, which allows the determination all the CEF parameters from the ab initio data (and not only the end member energies). Once the energetics of each configuration is completed, the code then packages the result in a Thermodynamic Database (TDB) file that can then be used by standard CALPHAD modeling tools [27–31] for further analysis.

For the aforementioned demonstrations, we chose to investigate the binary Iridium-Ruthenium phase diagram. Iridium and Ruthenium (alloys and oxides), have primarily been of interest in the catalysis community and has applications in treatment of breast cancer [32], coatings [33], oxygen evolution reaction [34, 35]. Hart et. al. [36] also published the results of a large number of stable binary phases in alloys of the Pt-group metals (PGMs), in which it was reported that Ir-Ru binary alloys may have possible stable ordered phases. Thus, it is a good candidate alloy system for our illustration.

3.2 Methods

The process of quickly generating a phase diagram from ab initio data has been explained in detail in reference [25] and illustrated in [37]. The theoretical framework and the description of each command and of the code can be found in that paper as well. Here, we only outline the major steps of the process for the specific example system considered.

1. Setting up structures for electronic structure calculation:

   Sampling the accessible composition range of each potential phase using pre-generated Special Quasirandom Structures (SQS). Here, based on the high-throughput study from [36], we consider the hcp, fcc, $L1_2$ [38] and $D0_{19}$ [39] phases, to which we add the liquid phase. We jointly model the fcc and $L1_2$ as well as the hcp and $D0_{19}$ phases using the same CEF model. The composition grid used includes samples of each sublattice compositions in steps of 50 %

with additional point at 25 % interval on either one sublattice when the other sublattice is defect-free. This corresponds to a composition sampling density "level" of 3 in the `sqs2tdb` structure generation command (see Appendix for details). For the sake of completeness we also have included the other phase (B19, Pt_8Ti, Ir_2Tc, Hf_5Sc) modeled as line compounds even though we had strong indications that those phases will not be energetically competitive. We confirmed this exclusionary hypothesis through our calculations as well.

2. Calculating ab initio energies for each structure:

   One can calculate the electronic ground state formation energies of each of the structures using any electronic structure code. In this work, we used the plane wave basis projector augmented wave method (PAW) [40, 41] with the exchange correlation approximation being the generalized gradient approximation (GGA) in the Perdew-Burke-Ernzerhof (PBE) [42] form as implemented in the Vienna Ab-initio Simulation Package (VASP) [43, 44]. All calculations were conducted at a precision flag of *Accurate* (to set the plane wave cut-off as the maximum of the ENMAX in the POTCAR of the participating species) and an ionic convergence criterion of 10^{-4} eV. The optimization was performed using the conjugate gradient algorithm [45]. The no. of kpoints to sample the first Brillouin Zone was generated automatically at a fixed density of 20^3 Å^{-3}. The partial electronic occupancies were set according to the Methfessel-Paxton scheme of order 1 [46] with a smearing width of 0.1 eV (for overall good force and energies). At the end of the initial relaxation run, a further static electronic relaxation was performed using the tetrahedron method with Blöchl correction [47] (for more accurate energy calculation of the ground state configuration)

   Ab-initio molecular dynamics [48] was run at temperature above the melting point of Ir and Ru to obtain the energy of the liquid phase. The MD runs were conducted at fixed number of atoms, fixed volume and temperature (NVT ensemble) employing a Langevin Thermostat [49, 50]. The desired external pressure of 0 was achieved by adjusting the simulation cell size. Calculation settings (potential and exchange correlation functional, cutoffs, k-points, etc.) were kept consistent with that of the relaxation runs, except for the Fermi smearing, which was set to match the ionic temperature of 3000 K. MD was run for 3300 steps, with each step size being 1.5 fs for a total time of 4.95 ps. We considered the first 1000 steps as equilibration and averaged the energy of the final 2300 steps. The liquid composition sampling grid was kept coarse (levels 0 and 1 in `sqs2tdb`).

3. Calculating Vibrational Entropies:

   To calculate the effect of atomic vibrations in the neighborhood of the relaxed configuration at finite temperature, the `fitfc` code was used [51]. Symmetrically distinct configurations were generated by displacing atoms from their relaxed position and calculating the static energies of these configurations. Subsequently the reaction forces induced by the displacements (frozen in place) were fit to a harmonic spring model to calculate the free energy of vibrations.

This standard procedure is elaborated in [51]. In practice, a good speed/accuracy trade-off is obtained by performing these calculations for endmembers only (corresponding to a composition sampling accuracy "level" of 0). However, more accurate phase boundaries might demand similar calculations on a finer compositions sampling.

In the present work, phonon vibrations were calculated for the end-members of all phases and additionally up to level 1 for the fcc and hcp phase.

In all calculations, the minimum distance between periodic images of the displaced atoms were kept to 4 times the nearest neighbor distance for the phase under considerations (corresponding to the setting `frnn=4` in `fitfc`), while the range of the springs included while fitting a purely harmonic model (`ns=1` setting in `fitfc`) was at 2 times the nearest neighbor distance (`ernn=2` setting in `fitfc`) . The magnitude of displacement of the atoms from the relaxed state were kept at `dr=0.04` Å.

In cases where there were spurious mechanically unstable phonon modes, the procedure as described in the paper [51] was adopted, in which the code generates displacements along the unstable directions to double-check stability. If the instability is not confirmed, the newly generated reaction forces are added to the fit in order to correct the problem.

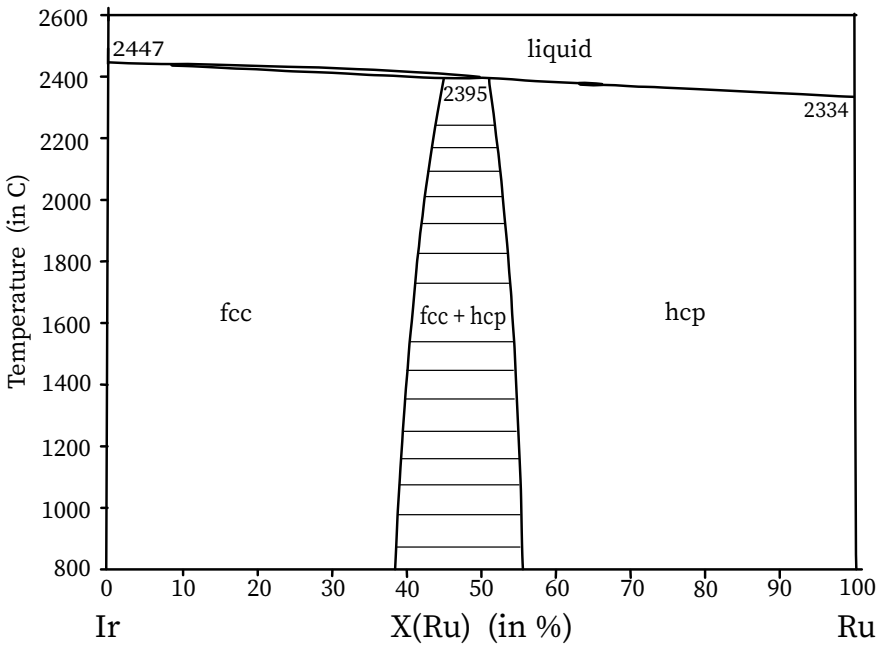

Figure 3.1: Experimental phase Diagram for Ir-Ru binary alloy, Okamoto H., Ir-Ru (Iridium-Ruthenium), Binary Alloy Phase Diagrams, II Ed., Ed. T.B. Massalski, Vol. 3, 1990, p 2345-2348, adapted from ASM International Alloy Phase Diagram database

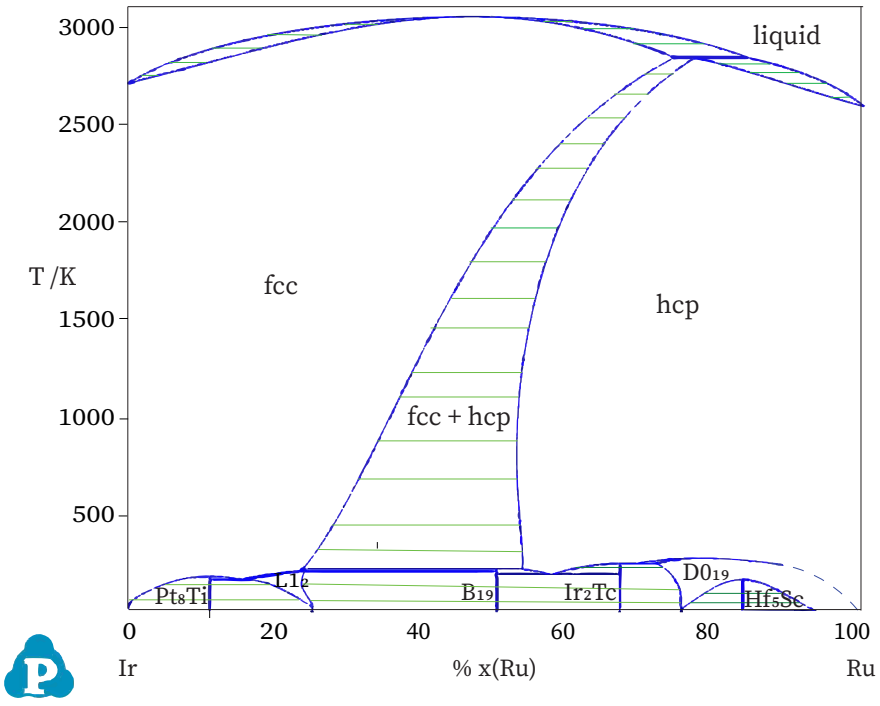

Figure 3.2: Calculated Phase Diagram

4. Reference states used:

   All formation energies were referenced to fcc Ir and hcp Ru. We did not make use of the experimental SGTE free energy difference between the fcc and hcp pure phases. The reason for proceeding in this way is that the SGTE and DFT hcp-fcc free energy differences do not agree very well [52] and we wanted our results to purely reflect the DFT predictions. The corresponding difference for Ru does agree well, so our strategy has little effect on the Ru-rich side of the phase diagram. In the `sqs2tdb` code, this choice of reference states is indicated by including the hcp Ir and fcc Ru phases in the file `exfromsgte.in` in the parent folder of the phase diagram calculations. It should be noted that hcp Ir and fcc Ru are not mechanically unstable, so the discrepancies with SGTE values found here can be attributed to DFT and not any specific treatment of mechanical instability [53].

5. Fitting the data with CALPHAD model:

   With all the energetics computed, a least square fit is performed to obtain the coefficients of the different polynomial thermodynamic functions (formation energy and vibrational formation free energy) according to the CALPHAD formalism. The numbers of terms in the excess free energy function for binary interactions in a sub-lattice of the phase under consideration was limited to 2. The inherent constraint of the CALPHAD formalism dictates that only one

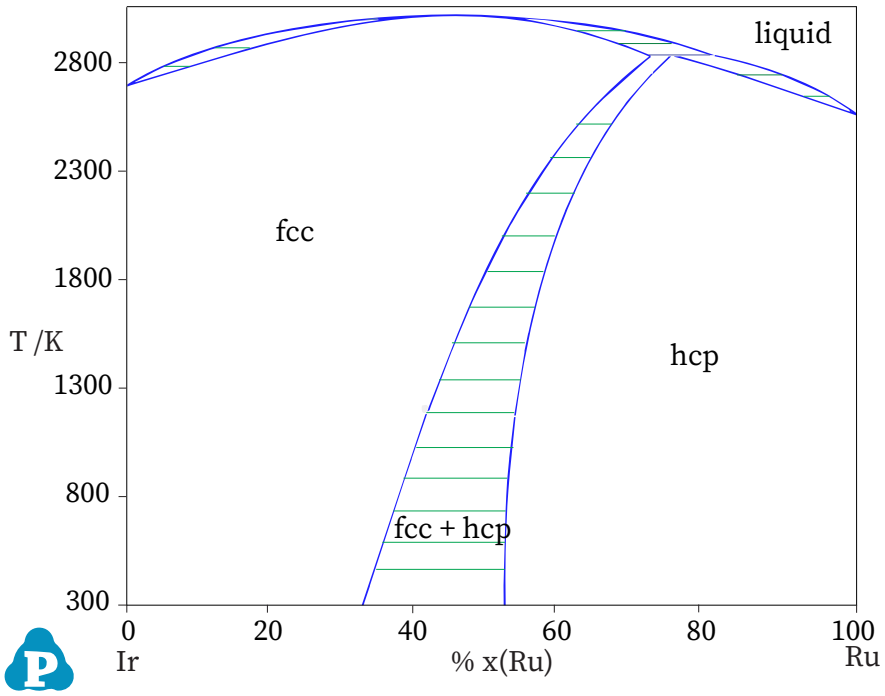

Figure 3.3: Calculated Phase Diagram (with FCC, HCP and Liquid only)

sublattice can have higher order interactions per term.

It should be noted that in this system, the predicted $L1_2$ and $D0_{19}$ phases from [36] turn out to be superstructures of fcc and hcp, respectively. This suggests making use of a multiple-sublattice framework to jointly handle each ordered phase and its associated disordered phase in a single phase description [11, 54]. This approach enables a good approximation of short-range-order (SRO) effects in the solid solution phases by allowing the different sublattices to adopt slightly different compositions. While it would be admittedly preferable to have fcc and hcp phases with uniform sublattice-independent compositions in a fully optimized CALPHAD model of the system, the simple scheme adopted here is ideal for rapid screening. As an input, this approach only demands a few extra SQS calculations in which the different sublattices have different compositions rather than necessitating the use of more advanced models, such as a cluster expansion.

3.3 Results and Discussion

The prediction by Hart and colleagues [36] of new ordered phases in the Ir-Ru system is surprising, given that existing experimental assessments of this system find no such phases [35, 55, 56] (see, for instance, Figure 3.1[57]). Our calculated Ir-Ru phase diagram (reported in Figure 3.2) immediately resolve this apparent conundrum: all predicted ordered phases disorder below room temperature,

making it unlikely that such phases could form through standard heat treatments.However, as our method does not account for SRO within each of the sublattices of $L1_2$ and $D0_{19}$, there is a risk that our calculated free energies for those phases are biased upward.

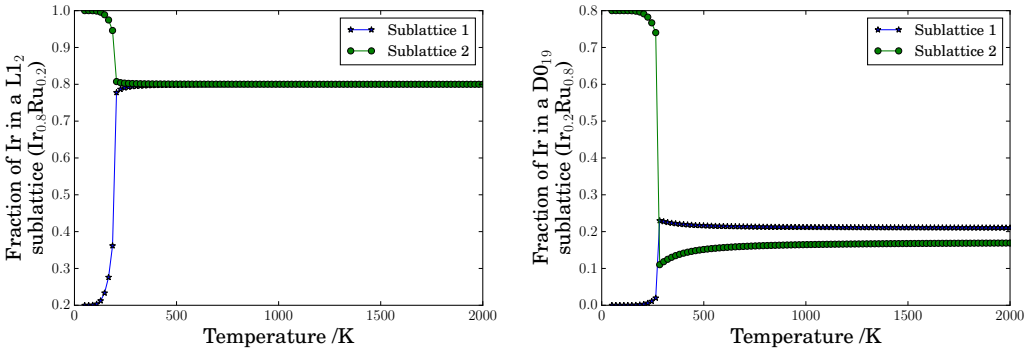

(a) (b)

Figure 3.4: (a) Distribution of Iridium in each sublattice of $L1_2$ at an overall composition of $Ir_{0.8}Ru_{0.2}$, , (b) Distribution of Iridium in each sublattice of $D0_{19}$ at an overall composition of $Ir_{0.2}Ru_{0.8}$, across a range of temperature 50-2000 K

Our calculated liquidus and solidus do not agree particularly well with the experimental assessments, but this is expected given the relatively simplified treatment used for the liquid state (only formation energies are calculated while entropic contributions solely come from the end members' entropy). Likewise, the shift in the predicted fcc-hcp two-phase region at high temperature, relative to the experimental result, is likely due to the use of a harmonic approximation the phonon calculations that becomes progressively less justified at higher temperatures. These inaccuracies, however, are inconsequential for our finding, namely that the predicted ordered phases become unstable at a relatively low temperature.

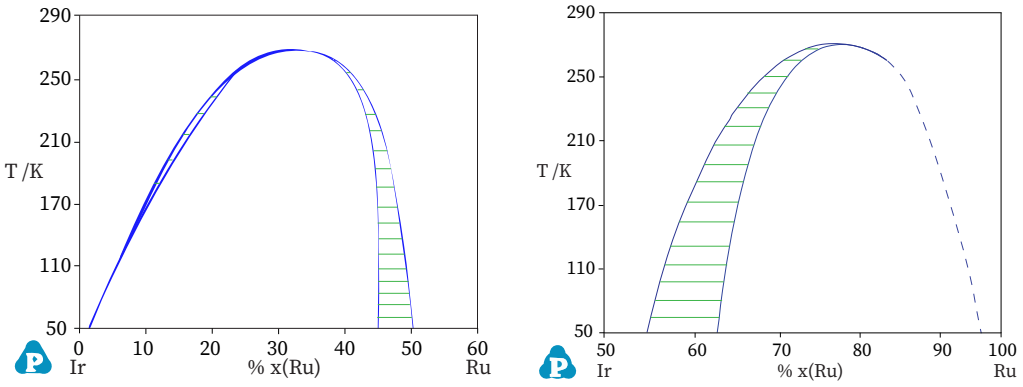

(a) (b)

Figure 3.5: (a) $L1_2$, (b) $D0_{19}$ phases only between 50-300 K, dashed lines denote a possible second order phase transition

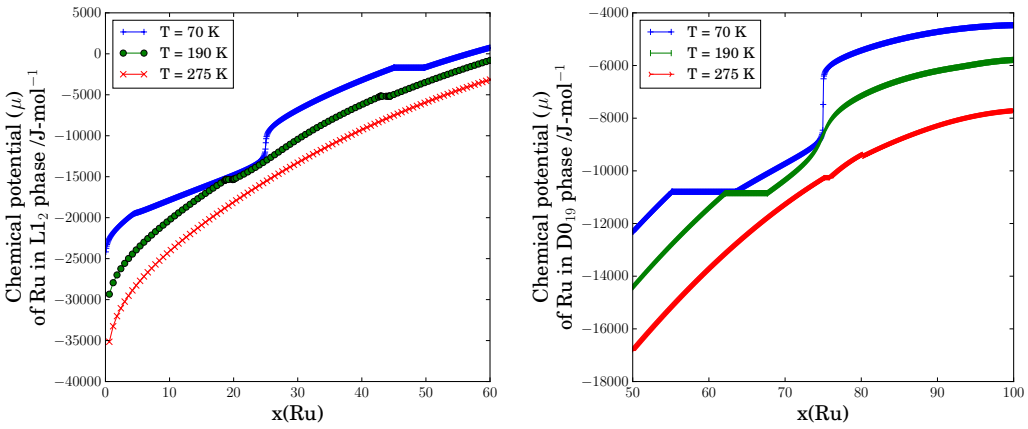

(a) (b)

Figure 3.6: (a) Chemical potential (μ) of Ru in $L1_2$ over a composition range of 0-60% Ru for T = 70, 190, 275 K, (b) Chemical potential (μ) of Ru in $D0_{19}$ over a composition range of 50-100% Ru for T = 70, 190, 275 K

Even though disordering occurs at low-temperatures in this system, the predicted ground states could still provide some information regarding the nature of the SRO in this system. To gain further insight into the system's ordering behavior, we calculate the equilibrium sublattices compositions (i.e. site fractions) for each of the ordered phases as a function of temperature (see Figure 3.4). We select overall compositions such that the graphs cut through the point of highest temperature in the phase's respective region of stability. For both the $L1_2$ and $D0_{19}$ phases, we find that the sublattice compositions sharply change at the transition temperature, consistent with a first order transition. The fact that the two sublattices of $L1_2$ have the essentially the same composition above the transition suggests that the fcc phase exhibits little SRO. For the $D0_{19}$ phase, the small ($< 5\%$) remaining difference in sublattice compositions above the transition temperature suggests that SRO in the hcp phase is also small, although more pronounced than in the fcc phase.

Given that the decomposition temperatures of all the ordered phases are so low, it proves more convenient for most applications to have a thermodynamic model that ignores the low temperature ordered phases and provides a single-sublattice description of the fcc and hcp phases. We have generated a such a thermodynamic model, using standard single-sublattice SQS and including the effect of short-range order using the Cluster Variation Method-based scheme described in [25]. This database is included in the supplementary information and the corresponding phase diagram is shown in Figure 3.3.

It is also instructive to study in more detail, the order-disorder transition by considering the metastable phase diagram for fcc-based and hcp-based phases separately (see Figure 3.5). At the level of accuracy of our thermodynamic description we use, it is not possible to unambiguously

identify second-order transitions, as all parametrizations used are smooth in composition and temperature by construction. However, whenever the width of a two-phase region shrinks to a point, this is suggestive that the phase transition becomes second-order. The $L1_2$ phase appears to be surrounded by first-order transitions, albeit very narrow ones on the Ir-rich side. The Ru-rich side transition are masked by hcp phases in the full phase diagram. The $D0_{19}$ phase exhibits clear first-order transition towards the Ir-rich side while the first-order character completely vanishes towards the Ru-rich side. To ascertain that this disappearance of the first-order transition is not merely a numerical artifact, we also plotted the chemical potential as a function of composition in Figure 3.6. These plots clearly confirm the absence of first-order transition on the Ru-rich side of the $D0_{19}$ phase, which would have been seen as a horizontal line. We conjecture that the phase transition becomes second-order and we indicate this possibility by a dashed line in Figure 3.5b (although its exact position cannot be determined from the present calculations).

3.4 Conclusion

Our first-principles approach to the construction of phase diagram, applied to the Iridium-Ruthenium Binary alloy system, has successfully helped explain certain inconsistencies between past experimental and high-throughput results. The absence of stable ordered phases, (such as the $L1_2$ and $D0_{19}$ phases in this work), in contrast to the predictions from high-throughput calculations, can be attributed to order-disorder transitions at a temperature range lower than the temperature range at which experimental phase diagrams are constructed.

In the process, we observe that representing disordered phases by a partially ordered multi-sublattice can act as a good proxy short range ordering (SRO) behavior. This is advantageous as SRO is computationally expensive [58, 59] to explicitly evaluate, although alternative KKR-CPA-based approaches [60–63], have been shown to be helpful to address this. In general, the CALPHAD formalism, in conjunction with our technique, can provide a general representation for both solid solutions and stoichiometric phases that is amenable to a high-throughput pipeline.

We also observe that entropic contributions to the free energy at higher temperatures can be approximated to a reasonable degree of accuracy by phonon calculations on a few structures (often end-members). For further improvements (particularly to address the greater mismatch solidus and liquidus curves between our calculation and experiments at higher temperature), we postulate that adopting anharmonic spring models and/or denser compositional grids would result in better estimations. A better model of the entropy of the liquid would also likely be needed.

For the purpose of speeding up the liquid calculations, our group is also working on including the liquid phase within the SQS framework. Our method nevertheless provides a automated pipeline for quick assessment of phase diagrams for exploratory purposes, that can be incrementally improved at each step of the calculation to desired levels of accuracy. Although the process described is with first-principles calculations only, it can be easily augmented, when fitting the CALPHAD model,

with experimental data to further enhance the accuracy.

References

1. Laughlin, D. E. & Hono, K. in *Physical Metallurgy (Fifth Edition)* Fifth Edition, 2837–2899 (Elsevier, Oxford, 2014).
2. Saal, J. E., Kirklin, S., Aykol, M., Meredig, B. & Wolverton, C. Materials Design and Discovery with High-Throughput Density Functional Theory: The Open Quantum Materials Database (OQMD). *JOM* **65,** 1501–1509 (2013).
3. Curtarolo, S., Hart, G. L. W., Nardelli, M. B., Mingo, N., Sanvito, S. & Levy, O. The high-throughput highway to computational materials design. *Nature Materials* **12,** 191–201 (2013).
4. Morgan, D., Ceder, G. & Curtarolo, S. High-throughput and data mining with ab initio methods. *Measurement Science and Technology* **16,** 296–301 (2004).
5. Van de Walle, A. & Asta, M. High-Throughput Calculations in the Context of Alloy Design. *MRS Bull.* **44,** 252 (2019).
6. Toher, C., Plata, J. J., Levy, O., de Jong, M., Asta, M., Nardelli, M. B., *et al.* High-throughput computational screening of thermal conductivity, Debye temperature, and Grüneisen parameter using a quasiharmonic Debye model. *Phys. Rev. B* **90,** 174107 (2014).
7. Liu, Z.-K. First-Principles Calculations and CALPHAD Modeling of Thermodynamics. *Journal of Phase Equilibria and Diffusion* **30,** 517 (2009).
8. Spencer, P. J. A brief history of CALPHAD. *Calphad* **32,** 1–8 (2008).
9. Sundman, B. & Ågren, J. A regular solution model for phases with several components and sublattices, suitable for computer applications. *Journal of Physics and Chemistry of Solids* **42,** 297–301 (1981).
10. Hillert, M. The compound energy formalism. *Journal of Alloys and Compounds* **320,** 161–176 (2001).
11. Kusoffsky, A., Dupin, N. & Sundman, B. On the compound energy formalism applied to fcc ordering. *Calphad* **25,** 549–565 (2001).
12. Frisk, K. & Selleby, M. The compound energy formalism: applications. *Journal of Alloys and Compounds* **320,** 177–188 (2001).
13. Jones, R. O. Density functional theory: Its origins, rise to prominence, and future. *Rev. Mod. Phys.* **87,** 897–923 (3 2015).
14. Bigdeli, S., Zhu, L.-F., Glensk, A., Grabowski, B., Lindahl, B., Hickel, T., *et al.* An insight into using DFT data for Calphad modeling of solid phases in the third generation of Calphad databases, a case study for Al. *Calphad* **65,** 79–85 (2019).

15. Chen, B., Li, Y., Guan, X., Wang, C., Wang, C. & Gao, Z. First-principles study of structural, elastic and electronic properties of ZrIr alloy. *Computational Materials Science* **105,** 66–70 (2015).

16. Ong, S. P. Accelerating materials science with high-throughput computations and machine learning. *Computational Materials Science* **161,** 143–150 (2019).

17. Arroyave, R., van de Walle, A. & Liu, Z.-K. First-principles calculations of the Zn–Zr system. *Acta Materialia* **54,** 473–482 (2006).

18. Adjaoud, O., Steinle-Neumann, G., Burton, B. P. & van de Walle, A. First-principles phase diagram calculations for the HfC–TiC, ZrC–TiC, and HfC–ZrC solid solutions. *Phys. Rev. B* **80,** 134112 (13 2009).

19. Ghosh, G., van de Walle, A. & Asta, M. D. First-principles calculations of properties of bcc, fcc and hcp solid solutio ns in Al-TM (TM = Ti, Zr, Hf) systems: A comparison between cluster expansion and supercell methods. *Acta Mater.* **56,** 3202 (2008).

20. Ghosh, G., van de Walle, A., Asta, M. D. & Olson, G. Phase Stability of the Hf-Nb System: From First-Principles to CALPHAD. *Calphad* **26,** 491 (2002).

21. Ghosh, G., van de Walle, A. & Asta, M. D. First-Principles Phase Stability Calculations of Pseudobinary Alloys of $(Al,Zn)_3Ti$ with $L1_2$, DO_{22} and DO_{23} Structu res. *J. Phase Equilib. Diff.* **28,** 9 (2007).

22. Mediukh, N., Ivashchenko, V., Turchi, P., Shevchenko, V., Leszczynski, J. & Gorb, L. Phase diagrams and mechanical properties of TiC-SiC solid solutions from first-principles. *Calphad* **66,** 101643 (2019).

23. Wang, R., Zhang, X., Wang, H. & Ni, J. Phase diagrams and elastic properties of the Fe-Cr-Al alloys: A first-principles based study. *Calphad* **64,** 55–65 (2019).

24. Burton, B. & van de Walle, A. First-principles phase diagram calculations for the system NaCl–KCl: The role of excess vibrational entropy. *Chemical Geology* **225,** 222–229 (2006).

25. Van de Walle, A., Sun, R., Hong, Q.-J. & Kadkhodaei, S. Software tools for high-throughput CALPHAD from first-principles data. *Calphad* **58,** 70–81 (2017).

26. Zunger, A., Wei, S.-H., Ferreira, L. G. & Bernard, J. E. Special quasirandom structures. *Physical Review Letters* **65,** 353–356 (1990).

27. Sundman, B., Jansson, B. & Andersson, J.-O. The Thermo-Calc databank system. *Calphad* **9,** 153–190 (1985).

28. Bale, C., Chartrand, P., Degterov, S., Eriksson, G., Hack, K., Ben Mahfoud, R., *et al.* FactSage thermochemical software and databases. *Calphad* **26,** 189–228 (2002).

29. Bale, C., Bélisle, E., Chartrand, P., Decterov, S., Eriksson, G., Hack, K., *et al.* FactSage thermochemical software and databases — recent developments. *Calphad* **33,** 295–311 (2009).

30. Cao, W., Chen, S.-L., Zhang, F., Wu, K., Yang, Y., Chang, Y., *et al.* PANDAT software with PanEngine, PanOptimizer and PanPrecipitation for multi-component phase diagram calculation and materials property simulation. *Calphad* **33,** 328–342 (2009).

31. Sundman, B., Kattner, U. R., Palumbo, M. & Fries, S. G. OpenCalphad - a free thermodynamic software. *Integrating Materials and Manufacturing Innovation* **4,** 1–15 (2015).

32. Wei, C., Liu, Y., Zhu, X., Chen, X., Zhou, Y., Yuan, G., *et al.* Iridium/ruthenium nanozyme reactors with cascade catalytic ability for synergistic oxidation therapy and starvation therapy in the treatment of breast cancer. *Biomaterials* **238,** 119848 (2020).

33. Vuković, M., Čukman, D., Milun, M., Atanasoska, L. D. & Atanasoski, R. T. Anodic stability and electrochromism of electrodeposited ruthenium-iridium coatings on titanium. *Journal of Electroanalytical Chemistry* **330,** 663–673 (1992).

34. Shan, J., Guo, C., Zhu, Y., Chen, S., Song, L., Jaroniec, M., *et al.* Charge-Redistribution-Enhanced Nanocrystalline Ru@IrO_x Electrocatalysts for Oxygen Evolution in Acidic Media. *Chem* **5,** 445–459 (2019).

35. Kötz, R. & Stucki, S. Oxygen Evolution and Corrosion on Ruthenium-Iridium Alloys. *Journal of The Electrochemical Society* **132,** 103–107 (1985).

36. Hart, G. L. W., Curtarolo, S., Massalski, T. B. & Levy, O. Comprehensive Search for New Phases and Compounds in Binary Alloy Systems Based on Platinum-Group Metals, Using a Computational First-Principles Approach. *Phys. Rev. X* **3,** 041035 (4 2013).

37. Van de Walle, A., Sabisch, J., Minor, A. M. & Asta, M. D. Identifying rhenium substitute candidate multi-principal-element alloys from electronic structure and thermodynamic criteria. *Journal of Materials Research* **34,** 3296 (2019).

38. Himuro, Y., Tanaka, Y., Kamiya, N., Ohnuma, I., Kainuma, R. & Ishida, K. Stability of ordered $L1_2$ phase in Ni_3Fe–Ni_3X (X:Si and Al) pseudobinary alloys. *Intermetallics* **12,** 635–643 (2004).

39. Kang, S.-Y. & Onodera, H. Analyses of HCP/$D0_{19}$ and $D0_{19}$/$L1_0$ phase boundaries in Ti-Al-X (X=V, Mn, Nb, Cr, Mo, Ni, and Co) systems by the cluster variation method. *Journal of Phase Equilibria* **22,** 424–430 (2001).

40. Blöchl, P. E. Projector augmented-wave method. *Phys. Rev. B* **50,** 17953–17979 (1994).

41. Kresse, G. & Joubert, D. From ultrasoft pseudopotentials to the projector augmented-wave method. *Phys. Rev. B* **59,** 1758–1775 (3 1999).

42. Perdew, J. P., Burke, K. & Ernzerhof, M. Generalized Gradient Approximation Made Simple. *Phys. Rev. Lett.* **77,** 3865–3868 (1996).

43. Kresse, G. & Furthmüller, J. Efficiency of ab-initio total energy calculations for metals and semiconductors using a plane-wave basis set. *Computational Materials Science* **6,** 15–50 (1996).

44. Kresse, G. & Furthmüller, J. Efficient iterative schemes for ab initio total-energy calculations using a plane-wave basis set. *Phys. Rev. B* **54,** 11169–11186 (1996).

45. Press, W. H., Teukolsky, S. A., Vetterling, W. T. & Flannery, B. P. *Numerical Recipes in C (2nd Ed.): The Art of Scientific Computing* (Cambridge University Press, USA, 1992).

46. Methfessel, M. & Paxton, A. T. High-precision sampling for Brillouin-zone integration in metals. *Phys. Rev. B* **40,** 3616–3621 (1989).

47. Blöchl, P. E., Jepsen, O. & Andersen, O. K. Improved tetrahedron method for Brillouin-zone integrations. *Phys. Rev. B* **49,** 16223–16233 (23 1994).

48. Kühne, T. D. Second generation Car-Parrinello molecular dynamics. *Wiley Interdisciplinary Reviews: Computational Molecular Science* **4,** 391–406 (2014).

49. Evans, D. J. Computer "experiment" for nonlinear thermodynamics of Couette flow. *The Journal of Chemical Physics* **78,** 3297–3302 (1983).

50. Hoover, W. G., Ladd, A. J. C. & Moran, B. High-Strain-Rate Plastic Flow Studied via Nonequilibrium Molecular Dynamics. *Phys. Rev. Lett.* **48,** 1818–1820 (26 1982).

51. Van de Walle, A. Multicomponent multisublattice alloys, nonconfigurational entropy and other additions to the Alloy Theoretic Automated Toolkit. *Calphad. Tools for Computational Thermodynamics* **33,** 266–278 (2009).

52. van de Walle, A. Invited paper: Reconciling SGTE and ab initio enthalpies of the elements. *Calphad* **60,** 1–6 (2018).

53. Van de Walle, A., Hong, Q., Kadkhodaei, S. & Sun, R. The free energy of mechanically unstable phases. *Nature Communications* **6,** 7559 (2015).

54. Ansara, I., Dupin, N., Lukas, H. L. & Sundman, B. Thermodynamic assessment of the Al-Ni system. *Journal of Alloys and Compounds* **247,** 20–30 (1997).

55. Yusenko, K. V., Martynova, S. A., Khandarkhaeva, S., Fedotenko, T., Glazyrin, K., Koemets, E., *et al.* High compressibility of synthetic analogous of binary iridium–ruthenium and ternary iridium–osmium–ruthenium minerals. *Materialia* **14,** 100920 (2020).

56. Saltykova, N. A. & Portnyagin, O. V. Electrodeposition of Iridium–Ruthenium Alloys from Chloride Melts: the Structure of the Deposits. *Russian Journal of Electrochemistry* **37,** 924–930 (2001).

57. Okamoto, H., Massalski, T. B. & etc. *Binary alloy phase diagrams* 2345–2348 (ASM International, 1990).

58. Kikuchi, R. A Theory of Cooperative Phenomena. *Physical Review* **81,** 988–1003 (1951).

59. Pelizzola, A. Cluster variation method in statistical physics and probabilistic graphical models. *Journal of Physics A: Mathematical and General* **38,** R309–R339 (2005).

60. Khan, S. N., Staunton, J. B. & Stocks, G. M. Statistical physics of multicomponent alloys using KKR-CPA. *Phys. Rev. B* **93,** 054206 (5 2016).

61. Johnson, D. D., Nicholson, D. M., Pinski, F. J., Györffy, B. L. & Stocks, G. M. Total-energy and pressure calculations for random substitutional alloys. *Phys. Rev. B* **41,** 9701–9716 (14 1990).

62. Soven, P. Coherent-Potential Model of Substitutional Disordered Alloys. *Phys. Rev.* **156,** 809–813 (3 1967).

63. Zeller, R. Multiple-scattering solution of Schrodinger's equation for potentials of general shape. *Journal of Physics C: Solid State Physics* **20,** 2347–2360 (1987).

Chapter 4

CVM Correction for Short Range Ordering in Iridium-Ruthenium Binary Phase Diagram

4.1 Introduction

The Cluster Variation Method (CVM) technique, first prescribed by Kikuchi [1–5] and reformulated by Barker [6], can construct a parameterized Hamiltonian for alloy free energies by fitting ab-initio energies to a orthogonal basis of Ising-like clusters functions in the formalism introduced by Sanchez and colleagues [7–9]. Since then it has been successfully used to predict phase stability of binary [10, 11] and ternary alloys [12] , semiconductors [13], vacancies [14], ionic systems [15], lattice vibrations [16–18], special quasirandom structure generation [19, 20], and more recently in the study of anti-phase boundaries [21] and high entropy alloys [22, 23].

We observed in Chapter 3 that while at low T, the ordered phases in the Iridium-Ruthenium binary alloy as predicted by Hart et. al[24] are indeed stable, at higher temperature the system disorders due to entropic effects[25]. It was further deduced that the reported stability of ordered phases are an artifact of the equivalence of ordered and disordered phase site fractions at high temperature. There is therefore a need to introduce temperature dependent corrections to the free energy of disordered phases to accommodate partial short range ordering (SRO), to prevent such conflicting computational and experimental results in a systematically improvable fashion integrated into the CALPHAD model.

In this Chapter, we introduce a software implementation to obtain a temperature dependent function under the CVM formalism representing SRO corrections to the alloy free energy. The code is

independent but seamlessly integrated into the `sqs2tdb` pipeline. This CVM+SQS+CALPHAD amalgamated approach generalizes SQS's ability to represent both partial ordering at low T (via a local short range Cluster Expansion (CE)) and disordered high T structures within a single phase description. Here we numerically minimise Eqn. 2.42 [1], to obtain the optimised CVM free energy of a fixed composition structure up-to a local short-range cluster basis over a range of temperatures. The difference of the optimized free energy from the free energy of a completely disordered structure correlations is then fit to a function which serves as an T-dependent SRO corection to CALPHAD free energy functions. The theoretical background of the CVM approach has been elucidated in Chapter 2; here we only focus on the implementation and working principles by re-evaluating the Ir-Ru binary phase diagram with SRO corrections included. This computationally cheap and systematically improvable strategy reproduces the experimental phase diagram with greater degree of accuracy than in Chapter 3.

4.2 Methods

4.2.1 Input Parameters and files

The procedure to generate the SQS for each phase - fcc, hcp and performing the initial relaxations (including inflection-detection if any) is described in Appendix A. To determine the SRO correction, one does not strictly require any electronic structure relaxation/phonon calculations to be performed prior. It is an independent program but `sqs2tdb` can read the output T-dependent correction function whenever present and include it in the TDB file.

The complete list of parameters and input files are shown in Appendix B. The most relevant input files for the code are:

1. `lat.in` - A file containing the description of the lattice and the atomic basis.
2. `maxclus.in` - A file containing the coordinates of the maximal cluster measured in the lattice reference frame as described in the `lat.in` file. In this work, we adopted the tetrahedron approximation to include the smallest tetrahedron as the maximal 4-point cluster for both hcp and fcc phases.

The `lat.in` is written in the ATAT[31, 32] format describing the global frame of reference, the lattice vectors in terms of the global reference and the basis atoms as fractional coordinates of the lattice vectors. Each line in the `maxclus.in` contain the fractional coordinates of the each atom constituting the maximal cluster. With the aforementioned input files, the SRO correction code utilizes the `cvmclus` routine in ATAT to obtain other CVM parameters.

3. `eci.out` - A file containing the Effect Cluster Correlations (2.26). This can be obtained by performing a CE (usually short range is sufficient) with the set of clusters constrained to

[1] Alternative to Monte Carlo methods as investigated by many [12, 26–30]

include the maximal cluster in `maxclus.in` and all sub-clusters encapsulated by it.

4.2.2 Lattice and Cluster description - fcc and hcp

We use the primitive unit cell description of the fcc and hcp phase and include up to the tetrahedral cluster. The respective `lat.in` and `maxclus.in` is shown in Table 4.1

fcc

`lat.in`

```
1.0 1.0 1.0 90 90 90
0.0 0.5 0.5
0.5 0.0 0.5
0.5 0.5 0.0
0.0 0.0 0.0 Ir,Ru
```

`maxclus.in`

```
1.0 1.0 1.0
1.0 0.5 1.5
0.5 1.0 1.5
0.5 0.5 1.0
```

---

hcp

`lat.in`

```
1.0 1.0 1.63299 90 90 120
1.0 0.0 0.0
0.0 1.0 0.0
0.0 0.0 1.0
0.0 0.0 0.0 Ir,Ru
0.6666666 0.3333333 0.5 Ir,Ru
```

`maxclus.in`

```
1.000000 1.000000 1.000000
1.666667 1.333333 1.500000
0.666667 0.333333 1.500000
0.666667 1.333333 1.500000
```

Table 4.1: Lattice description and coordinates of the tetrahedral maximal cluster for fcc and hcp. On the left we have the `lat.in` file elucidating the global coordinate frame, lattice vectors and basis atom coordinates. On the right we have contents of `maxclus.in` which denote the coordinates of the maximal cluster, one site in each line in terms of fractional coordinates of the lattice vectors.

Fig. 4.1 and 4.2 show the spatial description of the maximal tetrahedrally coordinated cluster and

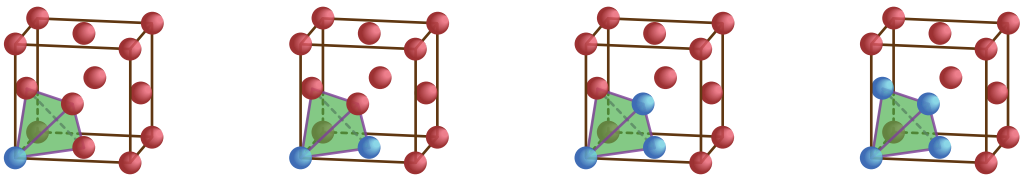

(a) 1-point (b) 2-point (c) 3-point (d) 4-point

Figure 4.1: Description of the different clusters (excluding the zero point cluster), embedded inside a conventional unit cell completely containing the maximal tetrahedron cluster in a fcc lattice. Note that the super-cell construction is for visual convenience only. The `lat.in` and `maxclus.in` contain all necessary information. Any symmetrically equivalent cluster is also an equivalent description.

it's sub-clusters for fcc and hcp lattice respectively. The reader must note that there is nothing special in this particular choice of visualization and any symmetrically equivalent tetrahedron is also equally correct. Also there is no necessity for a super-cell construction. All information is contained in the lattice (`lat.in`) file. All energies reported in this work are in eV per cluster. All multiplicities

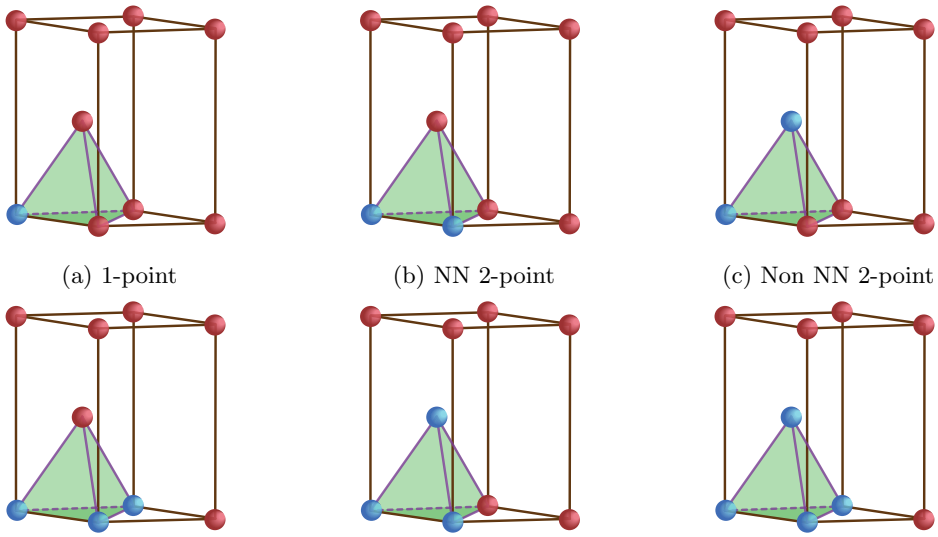

(a) 1-point (b) NN 2-point (c) Non NN 2-point

(d) NN 3-point (e) Non NN 3-point (f) 4-point

Figure 4.2: Description of the different clusters (excluding the zero point cluster), embedded inside a conventional unit cell completely containing the maximal tetrahedron cluster in a hcp lattice. Note that the super-cell construction is for visual convenience only. The `lat.in` and `maxclus.in` contain all necessary information. Any symmetrically equivalent cluster is also an equivalent description.

(cluster and cluster configurations) reported are per the unit cell described in `lat.in`.

For a Ir-Ru binary system, Table 4.2 and Table 4.3 shows the different types of clusters configurations and the sub-configurations along with the KB coefficients and ECIs for fcc and hcp lattice respectively.

Cluster Type	Cluster Multiplicity	Configuration Multiplicity	KB coefficient	ECI
0	1	1	0	-0.065991
1	1	1,1	5	0.000572
2	6	1,2,1	-1	0.009748
3	8	1,3,3,1	0	0.000024
4	2	1,4,6,4,1	1	-0.000418

Table 4.2: All clusters and configurations, with the KB coefficients for the Ir-Ru binary fcc tetrahedron maximal cluster. All clusters of same number of sites have equal KB coefficient.

The output of `cvmclus` are the following files:

1. `clusters.out` - Contains the type, multiplicity, radius, cluster variable occupations and coordinates of the atoms constituting the clusters.

Cluster Type	Cluster Multiplicity	Configuration Multiplicity	KB coefficient	ECI
0	1	1	0	-0.140347
1	2	1,1	2	-0.007593
2	6	1,2,1	0	0.010582
2	6	1,2,1	-1	0.009092
3	2	1,3,3,1	-1	0.000943
3	12	1,1,2,2,1,1	0	0.000783
4	4	1,1,3,3,3,3,1,1	1	-0.000203

Table 4.3: All clusters and configurations, with the KB coefficients for the Ir-Ru binary hcp tetrahedron maximal cluster. All clusters of same number of sites have equal KB coefficient.

2. `clustermult.out` - Contains the multiplicities of the cluster functions.

3. `configkb.out` - Contains the Kikuchi-Barker (KB) coefficients for each cluster. Note that all clusters having the same number of points have equal KB coefficients.

4. `config.out` - Contains the type, multiplicity, element types and coordinates of the atoms constituting the cluster configurations.

5. `configmult.out` - Contains the multiplicities of the cluster configurations.

Note that going from cluster configuration to cluster correlations reduces the dimensionality of the problem since for a system of M elements, you have M different types of point cluster configurations, but $M-1$ different point cluster functions. This means that in the most general case, number of clusters will always be less than equal to number of cluster configurations.

6. `vmat.out` - Contains the V-matrix which is a linear map from cluster correlation space to cluster configuration space. For every cluster configuration of n-atoms having a cluster configuration multiplicity K. There exists a $K \times C$ matrix that transform the C dimensional correlations (equal to number of clusters) to a K dimensional cluster configuration probabilities for all sub-clusters configurations of clusters of the same type. By construction, all cluster configuration probabilities of the same type sum to unity.

4.2.3 CVM Free Energy function, Jacobian and Hessian

As shown in Eqn. 2.42, the CVM Free energy in terms of cluster correlations up to the maximal cluster can be re-written in terms of the output of `cvmclus` as,

$$F = \sum_{i}^{\text{clusters}} m_i V_i \xi_i + k_B T \sum_{i}^{\text{configs}} k_i \left[\sum_{j}^{\text{subconfig}} \alpha_{ij} \left(\sum_{c}^{\text{clusters}} v_{ijc} \xi_c \right) \log \left(\left| \sum_{c}^{\text{clusters}} v_{ijc} \xi_c \right| \right) \right] \tag{4.1}$$

where, k_{B} is the Boltzmann constant, T is the temperature, V_i are the ECIs, ξ_i are the correlations. k_i are the KB coefficients. α_{ij} is the multiplicity of the jth sub-configuration of the i^{th} configuration type and m_i is the multiplicity of cluster i.

The corresponding Jacobian and Hessian of F is given as

$$\frac{\partial F}{\partial \xi_k} = m_k J_k + k_B T \sum_i^{\text{configs}} k_i \left[\sum_j^{\text{subconfig}} a_{ij} v_{ijk} \left\{ 1 + \log \left(\left| \sum_c^{\text{clusters}} v_{ijc} \xi_c \right| \right) \right\} \right] \tag{4.2}$$

$$\frac{\partial^2 F}{\partial \xi_k \partial \xi_{k'}} = k_B T \sum_i^{\text{configs}} k_i \sum_j^{\text{subconfig}} \frac{a_{ij} v_{ijk} v_{ijk'}}{\left(\sum_c^{\text{clusters}} v_{ijc} \xi_c \right)} \tag{4.3}$$

We have added an absolute value operator inside the logarithm, while this does not change the function between the valid bounds of $\rho \in [0, 1]$, outside the regime the function becomes convex and thus by construction make valid ρ's energetically favorable. This is necessary to constrain the optimization to live inside a inscribing polytope in correlation space that correspond to valid ρ's.

Modern numerical libraries are engineered for efficient matrix operations. Therefore for numerical convenience Eqn. 4.1, 4.2 and 4.3 can be recast in there matrix forms -

$$F = (M_{\text{clus}} \odot E) \cdot \xi + k_{\mathrm{B}} T (K \odot M_{\text{config}}) \cdot (V\xi \odot \log |V\xi|) \tag{4.4}$$

The Jacobian in the matrix form are given by:

$$\nabla F = (M_{\text{clus}} \odot E) + k_{\mathrm{B}} T \odot V^T \left[K \odot M_{\text{config}} \odot (1 \oplus \log |V\xi|) \right] \tag{4.5}$$

The Hessian in the matrix form is given by

$$\nabla^2 F = \left(\operatorname{diag} \left[(K \odot M_{\text{config}}) \oslash (V\xi) \right] V \right)^T V \tag{4.6}$$

Here m_{clus} is a vector containing cluster multiplicities, E are the vector of ECI's and ξ is the vector of correlations. $\odot$ represents a point-wise multiplication and $\cdot$ represents a vector inner product. m_{clus} contains the multiplicities of all cluster configurations (including sub-cluster configurations) stacked vertically. K is the vector of KB coefficients stacked vertically; since same type of cluster configurations have same KB, it is usually a column vector of continuous repeated elements. V is the complete V-matrix for all sub-cluster configurations stacked vertically. $\mathbf{1}$ denote a vector of ones while $\oplus$ and $\oslash$ arepoint-wise vector addition and division operators respectively.

The vector $M_{\text{clus}} \odot E$, $K \odot M_{\text{config}}$ and the other necessary matrix construction has to performed once at the start of the optimization. During the optimization, the mathematical operations are vectorized point-wise multiplications, logarithms, sums and matrix products, all of which have efficient algorithmic implementation in most linear algebra libraries (such as in [33]). The detailed

derivation of the matrix formulation of the free energy function and its derivatives can be found in Appendix C

4.2.4 Numerical Optimization

Using the cluster description and ECIs read from the user and `cvmclus` output, we conduct a non-linear constrained optimization to obtain the set of correlations for each SQS non-endmember which have the minimum free energy at the given T. Our code `srocorrection` is written in `python3`[34] and utilizes heavily the linear algebra routines in `numpy`[35] and `scipy`[36] for all optimization and curve fitting problems. The code is free and open-sourced under the MIT license and can be found here[2]. The process flow of the code is as follows:

1. Calculate Disordered and Ordered Correlations - The disordered structure is obtained using the code `corrdump` from the ATAT package.

   ```
   $ corrdump -l=lat.in -s=str.in -c=clusters.out -rnd
   ```

   which gives the correlations of the completely disordered structure with composition same as `str.in` for the set of clusters in `clusters.out` and lattice in `lat.in`.

   With fixed point correlations and ECIs, we then compute the ordered structure correlations by minimizing the enthalpy function as a constrained linear programming problem in correlation space. The linear programming problem is solved using the *revised simplex* method as outlined in [37] with the modification suggested by [38] and implemented in the `linprog` routine in `scipy.optimize`. The code has default parameters that work for most cases, however the detailed parameters can be found in Appendix B and here

2. Set up Bounds and Constraints - To obtain the optimised CVM correlations at fixed composition, we fixed all 1-point correlations equal to the 1-point correlations of the structure in `str.in`. We also limit the solution to lie inside a hyper-sphere of radius 1/2 between the ordered and disordered correlations in the correlation space.

   $$\left|\xi_{\text{optimized}} - \xi_{\text{disordered}}\right| \leq \frac{1}{2}\left|\xi_{\text{ordered}} - \xi_{\text{disordered}}\right| \tag{4.7}$$

   The constraint in Eqn. 4.7 ensures that the correction to the disordered phase does not extend up to the ordered phase since in such cases it would not be possible to distinguish the ordered phase from the disordered (the opposite of the issues in chapter 3). Additional constraint were introduced:

   (a) to limit the correlation search space between -1 and $+1$,

[2] https://github.com/reach2sayan/CVM

(b) bounds on the ρ's were enforced via a linear constraints on linear transformation of the correlations using the V-matrix.

(c) For ease of computation, we also fixed the 0-point correlation at +1 (which is an invariant).

3. Optimization - A trust-region[39] interior point algorithm as elucidated in [40] and implemented in the `minimize(method='trust-constr')` routine of `scipy.optimize` package was used to perform the optimization at each T between 300K and 3000 K with steps of 100K. Once again, the code has a set of default values which work well in general cases[3], however good solutions for non-linear optimization are very sensitive to the choice of hyper-parameters and the user is advised to perform some sort of hyperparamter tuning before production runs.

   Among the hyper-parameters, the initial trust radius (in this work, it was set to 0.01) is crucial to prevent the optimization getting stuck in a local minima or give bogus solutions altogether. To guess a reasonable initial trust radius, at each temperature point, we initially perform brute-force evaluation of free energy for 10^6 randomly chosen correlations normally distributed around the disordered correlations ($\mathcal{N}(0, 0.01)$) and choose the minimum of those as our first trial correlation. If the initial trust radius returns an invalid solution, we repeat the steps after reducing the radius until the optimization leads to a valid solution.

   Following which, the optimization might still get stuck at a local minima within the bounds of the constraints. To resolve this we perform 50 optimization at a fixed temperature with different trial correlations and keep the valid correlations with the minimum free energy. For all calculations, the tolerances for the termination of the optimization was set to 10^{-12} for both changes in correlations and the change in the norm of the lagrangian gradient between subsequent iterations. All other hyper-parameters are equal to the defaults provided by the `scipy.optimize` library.

4. Fitting a T dependent function to model SRO Correction - The end of the optimization routine outputs, for each temperature, the optimized CVM free energy F_{cvm} and the disordered free energy F_{rnd}. Therefore the corrected free energy for the structure is therefore

$$F = F_{\text{sqs}} + \underbrace{(F_{\text{cvm}} - F_{\text{rnd}})}_{r(T)} \tag{4.8}$$

   An ideal function to fit would be a general hyperbolic-tangent like function :

$$r(T) = C \left| \frac{\exp\left\{\left(-\frac{a_1}{k_{\text{B}}T}\right)\right\} - 1}{\exp\left\{\left(-\frac{a_2}{k_{\text{B}}T}\right)\right\} + 1} \right| \tag{4.9}$$

   However to cater to the limitations of the CALPHAD method, we expand the denominator in Eqn. 4.9 as Laurent expansion at $\frac{1}{T} \to \infty$ and truncating all terms beyond the linear term to

[3] tested on ternary bcc besides this work

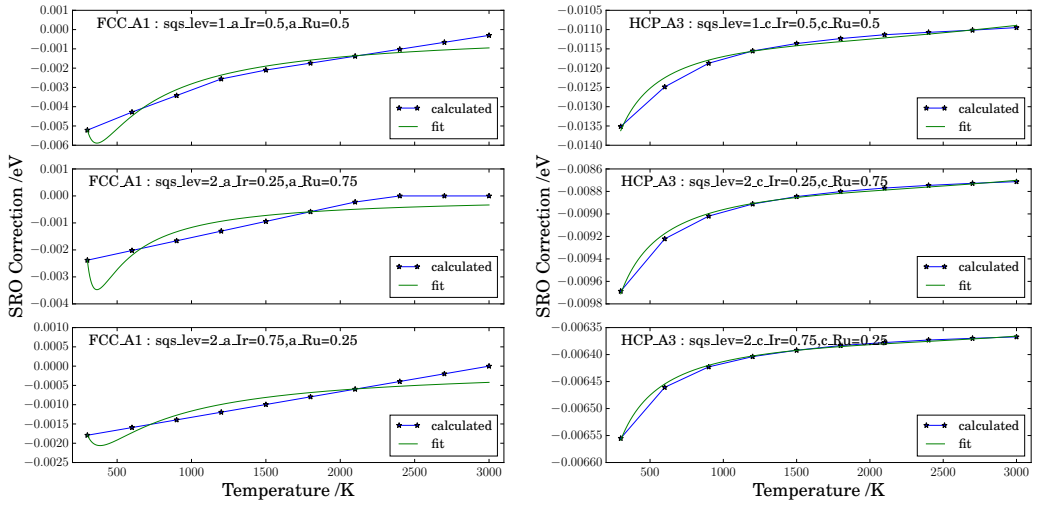

(a) (b)

Figure 4.3: (a) SRO Corrections within the tetrahedron approximation for fcc SQS $Ir_{0.5}Ru_{0.5}$, $Ir_{0.25}Ru_{0.75}$ and $Ir_{0.75}Ru_{0.25}$ (top to bottom). (b) hcp SQS $Ir_{0.5}Ru_{0.5}$, $Ir_{0.25}Ru_{0.75}$ and $Ir_{0.75}Ru_{0.25}$ (top to bottom). The points are the calculated $F_{\text{optimized}}$ - $F_{\text{disordered}}$ at each T. The continuous line is the T-dependent function fit.

obtain the following expansion

$$r(T) = a_1 - a_1 \exp\left\{\left(\frac{b_1}{T}\right)\right\} - \frac{a_2}{T} + \frac{a_2}{T} \exp\left\{\left(\frac{b_1}{T}\right)\right\} \tag{4.10}$$

which is commensurate to the CALPHAD limitations.

A typical command line instruction to initial a SRO Correction optimization would be

```
$ srocorrection --Tmin 300 --Tmax 3000 --Tstep 300 --xtol 1e-12 --gtol 1e-12 --
    initial_tr_radius 0.01 --global_trials 100
```

The code then outputs a file `func` in each SQS structure where SRO correction was evaluated. The `sqs2tdb` code is used to generate the TDB files from the energy, vibrational entropy and SRO-correction functions (the latter two if present). The steps to generate a TDB file is equivalent to that in Appendix A

```
$ foreachfile energy sqs2tdb -fit
$ sqs2tdb -tdb
```

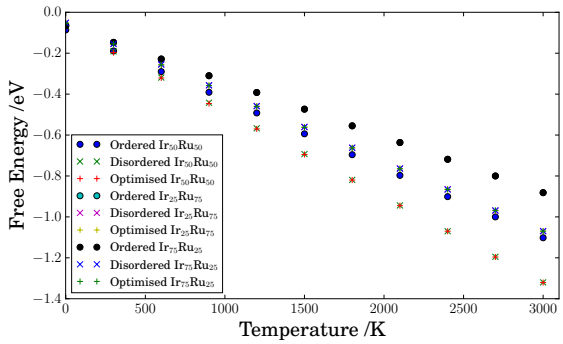

(a)

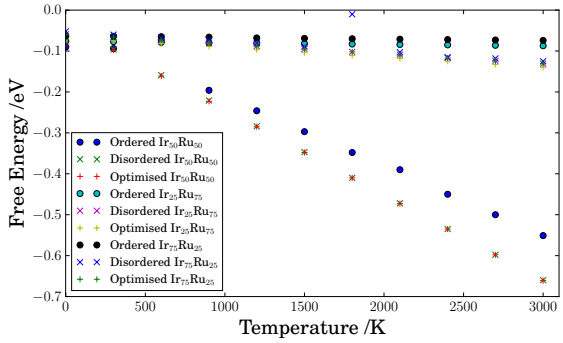

(b)

Figure 4.4: Plot showing the free energy of the optimized, ordered and disordered correlations at different temperatures for (a) fcc and (b) hcp. There is a substantial SRO corrections (under the tetrahedral CVM approximation) in the hcp phase. However under the same approximation, the fcc shows lower SRO correction. The disordered energy is consistently lower than the ordered energy indicating an order-disorder transformation below 300 K

4.3 Results and Discussion

Phase	Structure	Ordered Correlations	Disordered Correlations
HCP	Ir0.5-Ru0.5	1, 0, -0.33, -0.33, 0, 0, 1	1, 0, 0, 0, 0, 0, 0
	Ir0.25-Ru0.75	1, 0.50, 0, 0, -0.50, -0.50, -1	1, 0.50, 0.25, 0.25, 0.125, 0.125, 0.625
	Ir0.75-Ru0.25	1, -0.50, 0, 0, 0.50, 0.50, -1	1, -0.50, 0.25, 0.25, -0.125, -0.125, 0.625
FCC	Ir0.5-Ru0.5	1, 0, -0.33, 0, 1	1, 0, 0, 0, 0
	Ir0.25-Ru0.75	1, 0.5, 0, -0.5, -1	1, 0.5, 0.25, 0.125, 0.625
	Ir0.75-Ru0.25	1, -0.5, 0, 0.5, -1	1, -0.5, 0.25, -0.125, 0.625

Table 4.4: Table showing the Ordered and Disordered Correlations for each SQS structure up to level 2 excluding the end-members

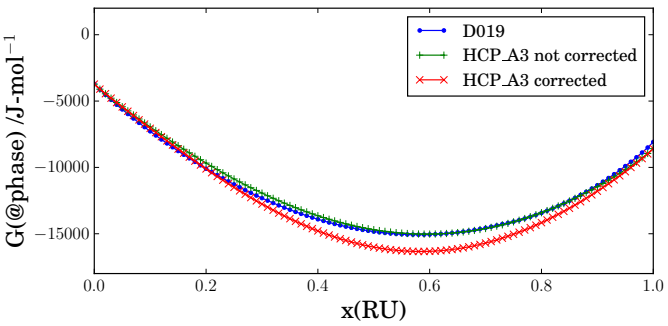

(a)

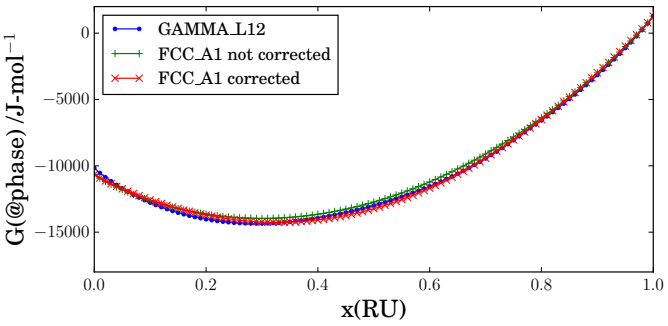

(b)

Figure 4.5: G vs X(Ru) plots for the (a) $D0_{19}$ and hcp (b) $L1_2$ fcc; with and without SRO correction. We can see the considerable SRO correction for hcp within the tetrahedron approximation.

In Fig. 4.3 we show the plot of SRO correction ($F_{\text{optimized}}$ - $F_{\text{disordered}}$) vs. temperature as calculated by the optimization routine. The points are the calculated data point whereas the continuous line is the fit. It must noted that Eqn. 4.10 has a singularity at $T = 0$ and thus the point should be excluded from the fitting if present in the optimization. We also explicitly show the trends in the CVM optimization with respect the ordered and disordered free energies by plotting them together in Fig. 4.4 for each SQS in the hcp and fcc phase at different temperatures. In Fig. 4.4a and 4.4b, it can be observed that in both fcc and hcp, the free energy of the ordered phase is higher than the disordered phase indicating an order-disorder transformation below 300K. Also within the limits of the tetrahedral approximation, there is a persistent SRO in the hcp phase that survives at temperature higher than room temperature when compared to fcc (Fig. 4.3). This is in agreement with Fig. 3.4 where we had a similar observation.

All pair terms upto level 3 (in the `terms.in` file) were used in the RK expansion terms to model the excess free energy of mixing to perfectly fit the energy of the fcc and hcp phase. In Fig. 4.5a, we can observe that at $T = 300K$, the correction is substantial in the Free-energy vs. composition plot for the hcp phase, while there is a small yet decipherable drop in the fcc curve.We can therefore postulate that within the tetrahedral approximation, the hcp phase represent sufficient interactions

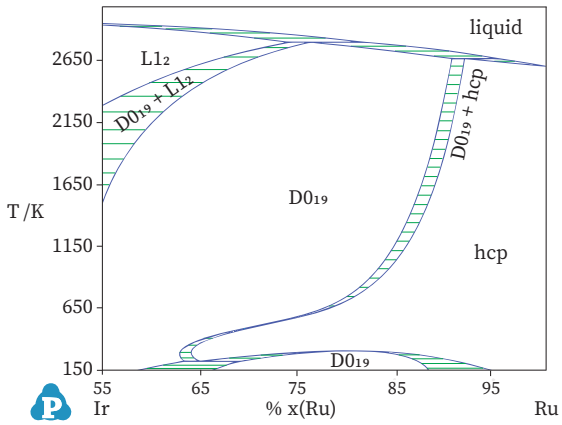

(a)

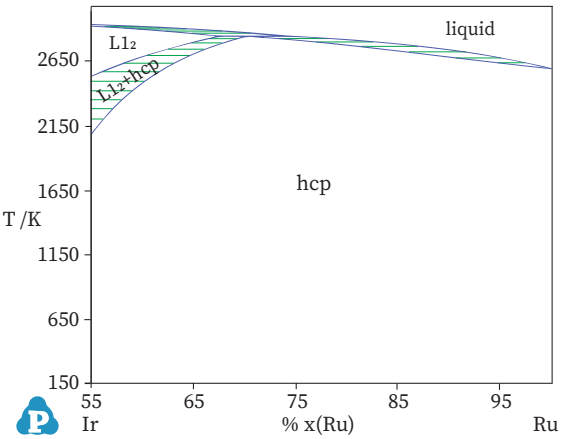

(b)

Figure 4.6: Calculated Phase Diagram with liquid, and all disordered and ordered phases - (a) without SRO correction, (b) with SRO correction

which can correct for the partial ordering of disordered phases. However, probably due to the lack of sufficient clusters in fcc, it is unable to capture necessary interactions for accurate SRO corrections. As a result, comparing Fig. 4.6b to Fig. 4.6a, it is evident that in the Ru rich side the Ir-Ru binary phase diagram, the SRO correction has successfully stabilized the disordered phase over its ordered counterpart $D0_{19}$. This also bears strong resemblance to the experimental phase diagram.

4.4 Conclusion

We have successfully demonstrated a software implementation of introducing temperature dependent SRO correction to alloy free energies under the CVM Formalism and integrated into `sqs2tdb`. The steps of the process - ordered correlation calculation, the central optimization and the T-dependent analytical function fit, are all independent of each other, and can be run as isolated calculations. In

addition to the core functionalities, we also provide a cluster description class that can run inside a *read–eval–print loop* (REPL) to analyse different cluster parameters such as multiplicities and V-Matrix. Vanilla SQS+CALPHAD approach provide an accurate description of high T disordered phases, however the current combined technique allows for incorporation of low T SRO corrections within a single phase description. The re-assessment results of the Ir-Ru phase diagram indicate good agreement with the claim. It is crucial to also note that the inclusion of SRO correction only up to the tetrahedral CVM approximation is sufficient to model the phase stability of the Ru rich hcp side with good agreement with experimental phase diagram. Therefore a limited set of clusters (like the tetrahedral approximation) and SQS's is sufficient to obtain levels of accuracy desired in a rapid high-throughput assessment for alloy free energies as a screening step in alloy-design with prospect for higher-accuracy if needed.

References

1. Kikuchi, R. CVM Entropy Algebra. *Progress of Theoretical Physics Supplement* **115,** 1–26 (1994).
2. Kikuchi, R. Second Hessian determinant as the criterion for order (first or second) of phase transition. *Physica A: Statistical Mechanics and its Applications* **142,** 321–341 (1987).
3. Kikuchi, R. A Theory of Cooperative Phenomena. *Physical Review* **81,** 988–1003 (1951).
4. Colinet, C. Applications of the cluster variation method to empirical phase diagram calculations. *Calphad* **25,** 607–623 (2001).
5. Colinet, C., Inden, G. & Kikuchi, R. CVM calculation of the phase diagram of b.c.c. FeCoAl. *Acta Metallurgica et Materialia* **41,** 1109–1118 (1993).
6. Barker, J. A. & Guggenheim, E. A. Methods of approximation in the theory of regular mixtures. *Proceedings of the Royal Society of London. Series A. Mathematical and Physical Sciences* **216,** 45–56 (1953).
7. Sanchez, J. M. Cluster expansions and the configurational energy of alloys. *Phys. Rev. B* **48,** 14013–14015 (1993).
8. Sanchez, J. M. Cluster expansion and the configurational theory of alloys. *Phys. Rev. B* **81,** 224202 (2010).
9. Sanchez, J. M., Ducastelle, F. & Gratias, D. Generalized cluster description of multicomponent systems. *Physica A: Statistical Mechanics and its Applications* **128,** 334–350 (1984).
10. Asta, M., de Fontaine, D., van Schilfgaarde, M., Sluiter, M. & Methfessel, M. First-principles phase-stability study of fcc alloys in the Ti-Al system. *Phys. Rev. B* **46,** 5055–5072 (1992).
11. Asta, M., McCormack, R. & de Fontaine, D. Theoretical study of alloy phase stability in the Cd-Mg system. *Phys. Rev. B* **48,** 748–766 (1993).

12. Lim, S. H., Murch, G. E. & Oates, W. A. Monte Carlo calculation of phase equilibria in ternary systems. *Calphad* **14,** 27–39 (1990).

13. Wei, S.-H., Ferreira, L. G. & Zunger, A. First-principles calculation of temperature-composition phase diagrams of semiconductor alloys. *Phys. Rev. B* **41,** 8240–8269 (1990).

14. Van der Ven, A. & Ceder, G. Vacancies in ordered and disordered binary alloys treated with the cluster expansion. *Phys. Rev. B* **71,** 054102 (2005).

15. Van der Ven, A., Ceder, G., Asta, M. & Tepesch, P. D. First-principles theory of ionic diffusion with nondilute carriers. *Phys. Rev. B* **64,** 184307 (2001).

16. Van de Walle, A. & Ceder, G. The effect of lattice vibrations on substitutional alloy thermodynamics. *Rev. Mod. Phys.* **74,** 11–45 (2002).

17. Kadkhodaei, S., Hong, Q.-J. & van de Walle, A. Free energy calculation of mechanically unstable but dynamically stabilized bcc titanium. *Physical Review B* **95** (2017).

18. Kadkhodaei, S. & van de Walle, A. Software tools for thermodynamic calculation of mechanically unstable phases from first-principles data. *Computer Physics Communications* (2019).

19. Zunger, A., Wei, S.-H., Ferreira, L. G. & Bernard, J. E. Special quasirandom structures. *Physical Review Letters* **65,** 353–356 (1990).

20. Van de Walle, A., Tiwary, P., de Jong, M., Olmsted, D. L., Asta, M., Dick, A., *et al.* Efficient stochastic generation of special quasirandom structures. *Calphad* **42,** 13–18 (2013).

21. Nataraj, C., Sun, R., Woodward, C. & van de Walle, A. First-principles study of the effect of Al and Hf impurities on Co3W antiphase boundary energies. *Acta Materialia* **215,** 117075 (2021).

22. Nataraj, C., Borda, E. J. L., van de Walle, A. & Samanta, A. A systematic analysis of phase stability in refractory high entropy alloys utilizing linear and non-linear cluster expansion models. *Acta Materialia* **220,** 117269 (2021).

23. Nataraj, C. M., van de Walle, A. & Samanta, A. Temperature-Dependent Configurational Entropy Calculations for Refractory High-Entropy Alloys. *Journal of Phase Equilibria and Diffusion* **42,** 571–577 (2021).

24. Hart, G. L. W., Curtarolo, S., Massalski, T. B. & Levy, O. Comprehensive Search for New Phases and Compounds in Binary Alloy Systems Based on Platinum-Group Metals, Using a Computational First-Principles Approach. *Phys. Rev. X* **3,** 041035 (4 2013).

25. **Samanta, Sayan** & van de Walle, A. Rapid screening of high-throughput ground state predictions. *Calphad* **74,** 102306 (2021).

26. Wu, Q., He, B., Song, T., Gao, J. & Shi, S. Cluster expansion method and its application in computational materials science. *Computational Materials Science* **125,** 243–254 (2016).

27. Nguyen, M. C., Zhao, X., Wang, C.-Z. & Ho, K.-M. Cluster expansion modeling and Monte Carlo simulation of alnico 5–7 permanent magnets. *Journal of Applied Physics* **117,** 093905 (2015).

28. Sun, R. & van de Walle, A. Automating impurity-enhanced antiphase boundary energy calculations from ab initio Monte Carlo. *Calphad* **53,** 20–24 (2016).

29. Chinnappan, R. Phase stability of V–Ta alloy using cluster expansion and Monte Carlo techniques. *Calphad* **39,** 33–36 (2012).

30. Van de Walle, A. & Asta, M. Self-driven lattice-model Monte Carlo simulations of alloy thermodynamic. *Modelling Simul. Mater. Sci. Eng.* **10,** 521–538 (2002).

31. Van de Walle, A., Asta, M. & Ceder, G. The Alloy Theoretic Automated Toolkit: A User Guide. *Calphad* **26,** 539–553 (2002).

32. Van de Walle, A. Multicomponent multisublattice alloys, nonconfigurational entropy and other additions to the Alloy Theoretic Automated Toolkit. *Calphad. Tools for Computational Thermodynamics* **33.** Code available from http://www.alum.mit.edu/www/avdw/atat, 266–278 (2009).

33. Anderson, E., Bai, Z., Bischof, C., Blackford, S., Demmel, J., Dongarra, J., *et al. LAPACK Users' Guide* Third (Society for Industrial and Applied Mathematics, Philadelphia, PA).

34. Van Rossum, G. & Drake, F. L. *Python 3 Reference Manual* (CreateSpace, Scotts Valley, CA, 2009).

35. Harris, C. R., Millman, K. J., van der Walt, S. J., Gommers, R., Virtanen, P., Cournapeau, D., *et al.* Array programming with NumPy. *Nature* **585,** 357–362 (2020).

36. Virtanen, P., Gommers, R., Oliphant, T. E., Haberland, M., Reddy, T., Cournapeau, D., *et al.* SciPy 1.0: Fundamental Algorithms for Scientific Computing in Python. *Nature Methods* **17,** 261–272 (2020).

37. Bertsimas, D., Tsitsiklis, J. N., Tsitsiklis, J., Bertsimas, D. & Tsitsiklis, J. *Introduction to Linear Optimization (Athena Scientific Series in Optimization and Neural Computation, 6)* Hardcover, 608 (Athena Scientific, Feb. 1, 1997).

38. Bartels, R. H. A stabilization of the simplex method. *Numer. Math.* **16,** 414–434 (1971).

39. Conn, A. R., Gould, N. I. M. & Toint, P. L. *Trust Region Methods* (Society for Industrial and Applied Mathematics, 2000).

40. Byrd, R. H., Hribar, M. E. & Nocedal, J. An Interior Point Algorithm for Large-Scale Nonlinear Programming. *SIAM J. on Optimization* **9,** 877–900 (1999).

Chapter 5

Classical EAM Force-Field construction of Zr-Cu-Al-Ni class of Bulk Metallic Glasses

5.1 Introduction

In certain metallic alloys, when a liquid melt is cooled at a fast cooling rate, nucleation process is inhibited and the alloy vitrifies to an amorphous state. Bulk Metallic Glasses (BMG) is class of multi-component metallic glasses with critical cooling rate of $< 10^3$ K/s and can be cast in thickness up to ~ 10 mm [1–5].

Several structural descriptors and conditions have been proposed to ascertain the Glass Forming Ability (GFA) of a candidate BMG alloy[6–13]. However conventional approach towards BMG alloy discovery leverage certain empirical trends such as:

1. 3 or more elements with mutual difference in radius $> 12\%$ [4, 14–16],
2. Negative Heat of mixing among the elements, favoring disorder between constituent elements [2]
3. 'Confusion principle': More the number of elements, greater is the 'frustration' to choose a particular crystal structure. [17].

The common theme in all these heuristics is the kinetic slowdown of atomic diffusion to hinder long range rearrangement. In the light of these observations viscosity of a liquid melt is often considered a key indicator of GFA. Since lower diffusivity of alloy melts correlate with higher viscosity; denser

and higher viscosity is indicative of higher GFA. BMGs are often characterized by homogeneous long range order and local icosahedron clusters; this also positively correlates with higher viscosity since the least mobile constituents are found in these clusters [18, 19]. BMG alloys exhibit a characteristic glass transition temperature (T_g), which is the temperature below which the supercooled liquid vitrifies. Lower degree of supercooling to transition into a glassy phase is a desirable property towards promoting glass formation. This is due to general sluggish kinetics inherent of solid phase is achieved without much drastic cooling regimen. The glassy structure would also expectedly bear more resemblance to the liquid structure in terms of distribution of atoms (among many other influencing factors notwithstanding). Therefore GFA is inversely related to the difference between the melting point ($\Delta T = T_m - T_g$) or directly related to Turnbull criterion (T_g/T_m). Deep eutectic phases in multicomponent alloys exihibit such behaviour and thus are of practical importance in the alloy search of new BMG materials.

Even with the aforementioned empirical criterion the candidate space is simply astronomical [6, 20]. While the stability of super-cooled liquids in deep-eutectic pockets make it amenable to viscosity measurements, the number of degrees of freedom in high-dimensional composition space make systematic search across the space tedious. The non-equilibrium nature (high cooling rates, surface diffusion), also pose experimental challenges. Therefore there is a need of a computational high-throughput technique to quickly assess promising structure prior to laborious experimental confirmations.

The Zr- family of BMGs have been known since seminal works of Inoue and co-workers [2, 21, 22] and since then have been extensively studied by the scientific community [22–30]. In this paper, we fit an analytical EAM model to the quaternary Zr-Cu-Ni-Al system and validate the potential over an independent test set. Using the potential we calculate viscosity using the Green-Kubo[31–33] formula for viscosity and the auto-correlation of the shear component of the stress tensor. We also performed equilibrium volume calculations at 0 bar pressure. All the EAM simulations were performed on a family of $Zr_{55+x}Cu_{30-x-y}Al_{10}Ni_{5+y}$ glasses where $x \in \{0, 5, 10\}$ and $y \in \{0, 2, 5, 10\}$ around the well-studied Zr-based BMG - $Zr_{55}Cu_{30}Al_{10}Ni_5$ [34–41]. This effort would form the basis of a more ambitious program of obtaining potentials for even more components, with the goal of exploring viscosity for novel glass-forming chemistries.

5.2 Methods

5.2.1 Preparing Fitting Dataset

All reference data containing Zr, Cu and Al along with a Zr-Cu-Al ternary EAM potential were obtained from this repository. The reference ternary EAM was constructed with 751 reference structures including solid solutions and intermetallics and crystals and liquids with the target of analyzing a $Zr_{47}Cu_{46}Al_7$ BMGs[30]. In addition, to include a 4th element Ni in the EAM fit, we searched for known crystal structures of pure Ni and inter-metallics between Zr,Cu,Al with Ni -

Zr_2Ni_7 (C12/m1), Zr_7Ni_{10} (Cmce), Zr_6Ni_{23} (Fm-3m) $ZrNi_2$ (Fd-3m), Cu_4NiAl_7 (R-3m), Ni_2Al_3 (P-3m1), Ni_3Al (Pm-3m), NiAl (Pm-3m), $NiAl_3$ (Pnma), Zr_5Ni_4Al ($P4_2/2$), $Zr_6Ni_8Al_{15}$ (Fm-3m), Zr_6NiAl_2 (P-62m) using the `pymatgen` python API of the Materials Project (MP) Database[42, 43]. To make the energy scale of the Zr-Cu-Al database and the additional Ni structures comparable, all new structures were relaxed using VASP with a plane-wave energy cut-off as 300 eV using Projector Augmented Wave (PAW)[44, 45] pseudopotentials with the Perdew-Burke-Ernzerhof (PBE)[46] exchange correlation functional. For each structure, the Brillouin zone was sampled with a $2 \times 2 \times 2$ Monkhorst-Pack grid. The relaxations was done in two step - a conjugate gradient ionic relaxation with fermi smearing set according to Methfessel-Paxton scheme of order 1[47] and a final static run with the tetrahedron method with Blöchl correction [48] (for more accurate energy calculation of the final configuration).

To create the full fitting dataset, the initial set of inter-metallics were relaxed using DFT and then a initial EAM fit was performed. Using this intermediate EAM, a MD of a NPT ensemble for 100 ps followed by NVT ensemble for 10 ps was run for all structures at an average temperature of 300K and 0 bar of pressure. The final structures were again relaxed using DFT to the locally stable configuration, added to the fitting dataset, and a new fit was conducted. This step-wise relaxation-MD run was performed twice more at 1000 K and 2000 K. All MD simulations in this work was run using the *Large-scale Atomic/Molecular Massively Parallel Simulator* (LAMMPS)[49]. It must be noted that while the initial structures from MP were defined as primitive unit cells, further NPT at 300, 1000 and 2000 K were performed on a commensurate super-cell having less than equal to 128 atoms. Since DFT relaxations find the local minima around the starting structure, the result of the DFT on high-T and liquid structures is not the stable ground-state but is essential to obtain excited state energies and forces which is required to model the energy landscape of high temperature liquid phase. On the other hand, the ordered inter-metallics provide crucial information about the energetics of the local environment in a long range amorphous structures. In total, the final fit comprised of 1943 structures with forces and stress value with an average concentration of 51.2% Zr, 29.95% Cu, 9.9% Al and 8.96% Ni. A hold-out set of 765 structures (sampled at random from the total structure pool) was used to assess the generalization error of the EAM. In Fig. 5.1, we show all the distinct compositions included in the fitting and testing dataset. At each composition, there exists multiple data-points representing 0 and high T structures.

5.2.2 EAM functions and fitting

In this work, we use analytical morse-type potential [50] (Eqn.2.62) for the pair functions,

$$E = D_r[(1 - \exp\{(-a(r - r_o))\})^2 - 1]$$

the electron density is represented by a oscillatory function[51] (Eqn. 2.63)

$$\rho(r) = \frac{1 + a_1 \cos(\alpha r + \varphi)}{r^\beta}$$

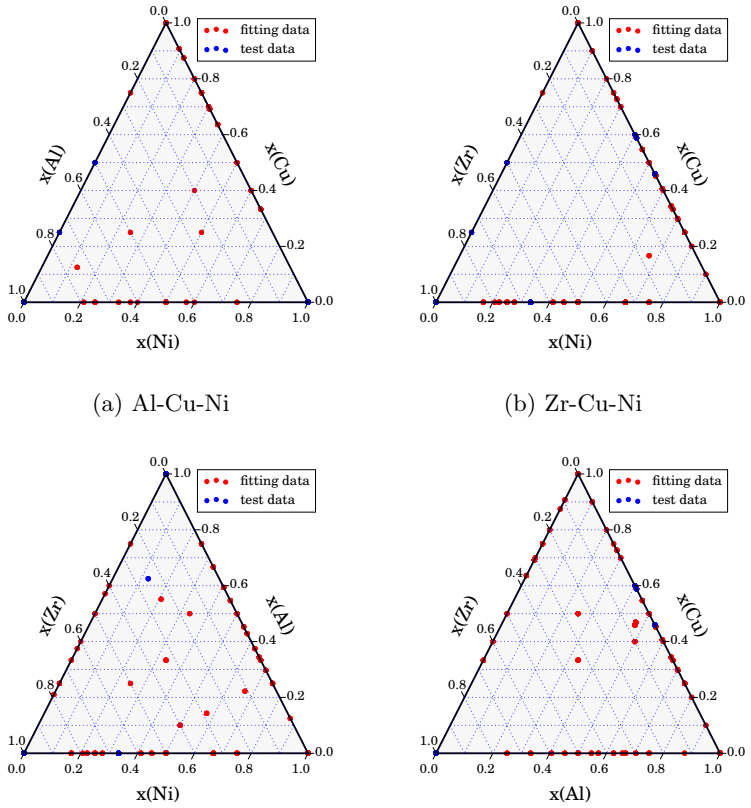

(a) Al-Cu-Ni

(b) Zr-Cu-Ni

(c) Zr-Al-Ni

(d) Zr-Cu-Al

Figure 5.1: Ternary plots showing the different compositions of the Zr-Cu-Al-Ni system for the fitting dataset (red) and the test set (blue). Note that at each composition, there are multiple structures with different configurations representing structures at 0, 300, 1000 and 2000 K. The intermetallic structures contain information about the local structure while high T structures accommodates for liquid behavior.

and the embedding energy in the form the the BJS function[52] (Eqn. 2.65).

$$E = E_o \left[1 - \gamma \log \rho\right] \rho^{\gamma} + E_1 \rho$$

The code `potfit`[53] was used to fit the EAM using the force matching algorithm [54]. A global cut-off radius of 6.5 Åwas set for all pair functions. In our fit, we weighted the total error contributions from the energies to 300 and that of stresses to 50 with respect to the an error contribution of weight factor for the forces which is set to 1. In addition, we boltzmann weighted the contribution of structures (forces,energies and stresses equally) with respect with distance from the convex hull at that composition, i.e.

$$w_i = 10 \times e^{-0.45 \Delta E_i} \tag{5.1}$$

where $\Delta E_i = E^* - E_i$, E^* is the lowest energy at that composition, E_i is the energy of the i^{th} structure with the same composition. This ensures that the convex hull structures have a stronger signal to the total error and it smoothly decays to higher energy structures. The initial fit was obtained with a non-linear least squares fits of the different analytical functions with the Zr-Cu-Al EAM potential for the Zr, Cu and Al pair, transfer and embedding functions. Similar fit was made for Zr-Ni pair and Ni transfer and embedding functions with the Ni-Zr EAM potential. The initial Al-Ni and Cu-Ni potentials were set to arbitrary but reasonable values which provide energies within the range of the dataset.

Typically in such high-dimension system, any gradient based iterative algorithm might get stuck at a local minima. To ameliorate this issue, an initial Simulated Annealing algorithm[55] based of off the original work by Metropolis et. al.[56] was executed for a coarse grain search of the global error landscape. Following which a gradient-free optimization algorithm (Powell's algorithm[57]) was executed to fine-tune the fit starting from the minimum error parameters obtained in the simulated-annealing step. The full set of parameters and initial potential and final potential parameters can be found in Appendix D.

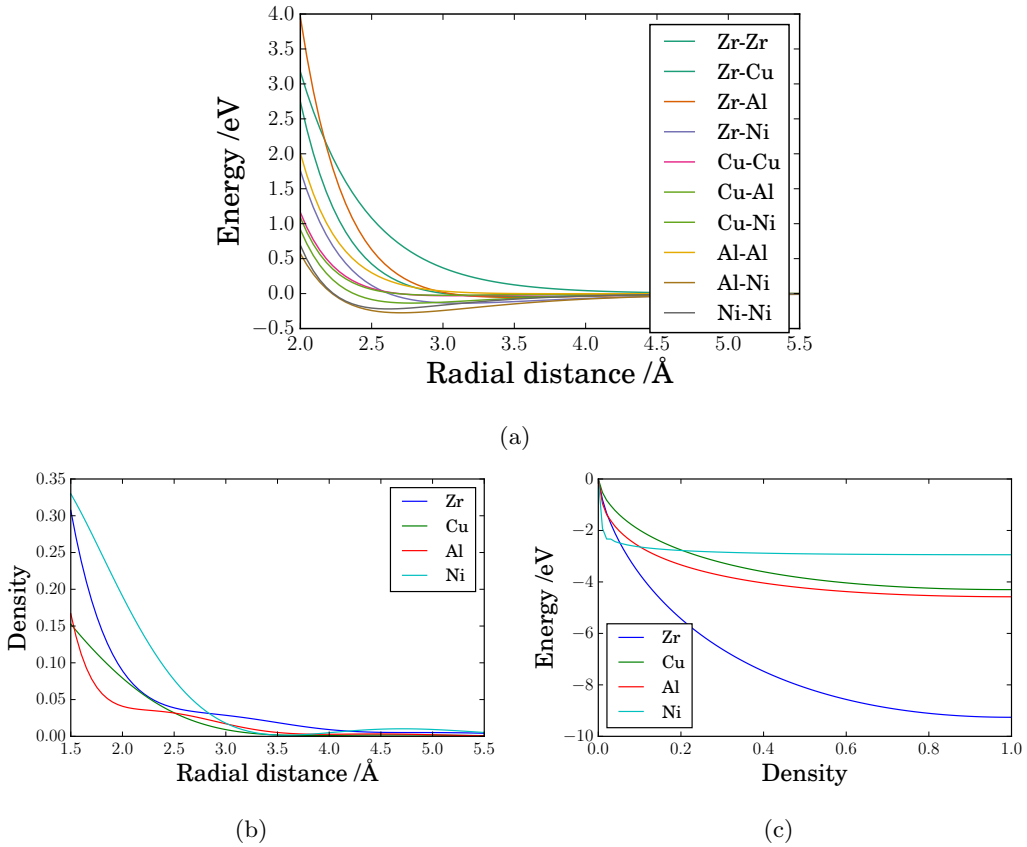

Figure 5.2: Potential Functions for (a) Morse Pair Potentials[50] for different pair combinations, (b) Transfer/Charge Density Functions (CSW)[51] and (c) Embedding Energy Functions (BJS)[52].

5.2.3 EAM structure generation and validation

In this work 10 distinct compositions of the Zr-Cu-Al-Ni systems was studied as a validation test on the fitted EAM - $Zr_{55}Cu_{20}Al_{10}Ni_{15}$, $Zr_{55}Cu_{25}Al_{10}Ni_{10}$, $Zr_{55}Cu_{28}Al_{10}Ni_{7}$, $Zr_{55}Cu_{30}Al_{10}Ni_{5}$, $Zr_{60}Cu_{15}Al_{10}Ni_{15}$, $Zr_{60}Cu_{20}Al_{10}Ni_{10}$, $Zr_{60}Cu_{23}Al_{10}Ni_{7}$, $Zr_{60}Cu_{25}Al_{10}Ni_{5}$, $Zr_{65}Cu_{10}Al_{10}Ni_{15}$, $Zr_{65}Cu_{15}Al_{10}Ni_{10}$, $Zr_{65}Cu_{18}Al_{10}Ni_{7}$, $Zr_{65}Cu_{20}Al_{10}Ni_{5}$.

For each structure, the same computational recipe was followed to (i) generate the 'liquid' structure followed by (ii) (a) calculation of equilibrium volume at 0 bars and, (b) viscosity calculation according to the Green-Kubo formalism at different temperatures between 800-1600 K. The timestep in all calculations was set to 0.001 ps and thermodynamic state of the ensembles were sampled every 5ps. As a starting template, we used a 32000 atom $Zr_{47}Cu_{46}Al_{7}$ glass structure. The atoms were re-labeled at random to obtain the desired composition, followed by a LAMMPS MD with an equilibriation NPT run at 300 K, 0 bar pressure for 100 ps, followed by a temperature ramp-up to 5000 K at a heating rate of $\sim$ 10 K/ns. Finally at the highest temp, we hold the temperature for 200ps.

We used the Green-Kubo (GK) formula[31–33] to relate the ensemble average of the auto-correlation of the shear stress components of the stress tensor to calculate shear viscosity at each temperature.

$$\eta = \frac{V}{k_{\mathrm{B}}T}\int_0^\infty \langle \sigma_{xy}(0)\sigma_{xy}(t)\rangle \, dt \tag{5.2}$$

A NVT equilibration run for 100 ps followed by a second equilibration at NPT for further 600 ps is performed. Following this, we calculate the NVT ensemble average of the auto-correlation of the non-diagonal components of the stress tensor over a time period of 3000 ps with a correlation window of 400 snapshots, each snapshot sampled every 5th timestep, with the average auto-correlation evaluated every 2000th timestep (2ps).

For the equilibrium volume calculation, the initial temperature was set to 800 in which a 100 ns NVT dynamics followed by a 600 ns NVT equilibration run were performed. Following which a NPT simulation with temperature ramp-up to 1800 K at a rate of $\sim$ 3 K/ns. In Appendix D, Fig. D.1, we show a schematic of the different MD schedules.

For pedagogical intent, we emphasize on the necessity of the initial *equilibration runs*. The pilot NVT run reduces statistical biases of the initial 'arbitrary' structure from affecting any statistics we collect from the simulation. The subsequent NPT run is then intended to reduce bias and obtain the equilibrium volume at the intended pressure of study (0 atm in study). Once the fluctuations of the thermodynamic variables has stabilized, *production runs* as entailed by the specifics of the simulation is carried out. In case of GK calculations, we switched to NVT, since we intended to monitor the stress at a constant volume (which was pre-equilibrated to the equilibrium volume at 0 atm).

5.3 Results and Discussion

RMS deviations of the forces, energy and stress for the EAM fit are 268.96 meV/Å, 242.89 meV and 0.156 MPa respectively. The average error in formation energy-per atom over all structures is 0.06 eV for the fitting dataset and 0.14 eV for the test dataset. Since the target application for this potential is to simulate liquid dynamics; the error is comparable to thermal fluctuations $k_{\mathrm{B}}T$ between $800 - 1800$ K. The approximate range of the energy (~ 5 eV) is comparable to the difference between the lowest (Zr : -8.51 eV/atom) and the highest (Cu : -3.72 eV/atom) single-atom energies. In addition to energy, the average error of 0.14 eV/Å over all single-atom force prediction is a desirable property since accurate forces would be instrumental is capturing physical stress correlations during viscosity calculations (explained later). In Fig. 5.3 we show the scatter plot of the predicted formation energy vs. the reference formation energy for the fitting data and the test data. The diagonal nature indicates an overall good fit for both energies and forces in the

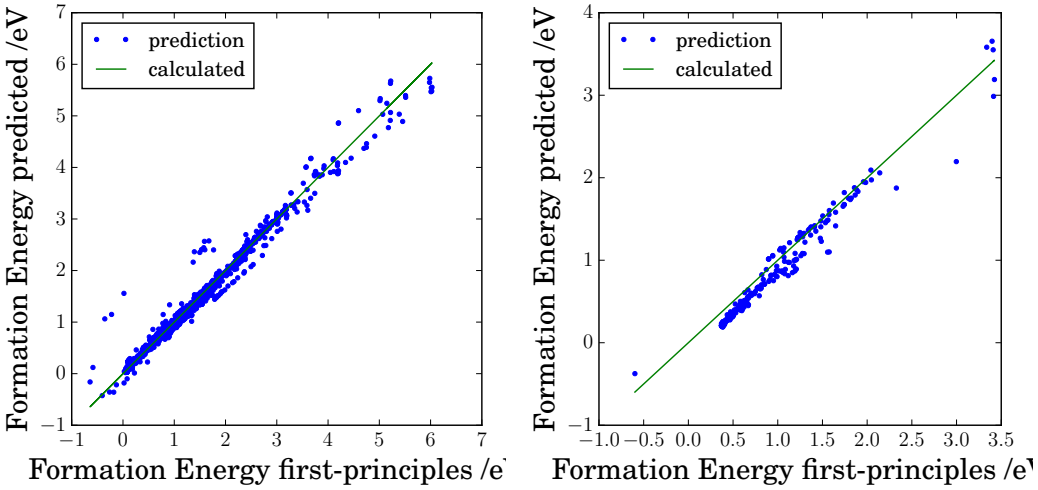

(a) (b)

Figure 5.3: Plot showing Predicted vs Reference energy for (a) fitting dataset, (b) test dataset. The diagonal nature indicate a good fit. Certain low energy bad predictions are for high Ni structures which are outside the composition range of interest. The higher energy discrepancy is a result of the boltzmann weighting of structures measured from the lowest energy structure at any given composition. The range of ~ 4 eV is comparable to difference between the species with highest and lowest single atom energy.

training set. An investigation of the deviation in the bottom left corner of Fig. 5.3a suggest that those are high Ni structures, which possibly contributed overall less to the error sum due to paucity of reference structures. The intended composition range for the applicability of our EAM is low Ni Zr-Cu-Al liquid BMGs and therefore the deviation is not a cause for concern. In Fig. 5.3b, the higher prediction error in the higher end of the energy and RMS forces could be direct result of the boltzmann weighting of the energies in the fitting data. Fig. 5.2a indicates the different

pair potential functions, Fig. 5.2b and Fig. 5.2c, the electron density / transfer functions[1] and the embedding energy function respectively.

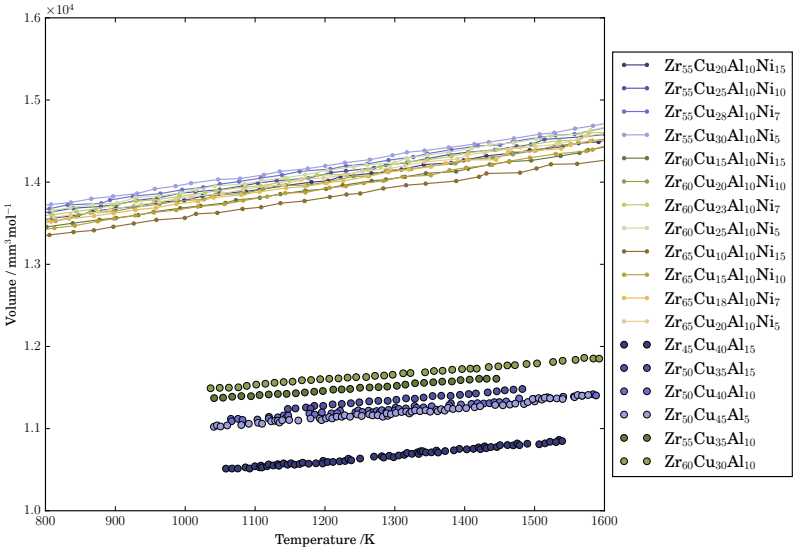

Figure 5.4: Equilibrium volume at 0 bar for different $Zr_{55+x}Cu_{30-x-y}Al_{10}Ni_{5+y}$. Dots are experimental data of Zr-Cu-Al liquids obtained from [58]

To the best of our knowledge, there is no published EAM potential for the Zr-Cu-Al-Ni system. Most experimental studies are also limited to the low temperature glassy structure and not of *liquid* Zr-Cu-Al-Ni alloys probably due to difficulty of accurate measurements and difficult experimental conditions. To validate our EAM viscosity calculations on the Zr-Cu-Al-Ni liquids, we compare our calculated viscosity's with experimental Zr-Cu-Al liquid volume and viscosity calculations from Yokoyama et. al.[58] and extrapolate the effects of Ni in the Zr-Cu-Al-Ni system.

Fig. 5.4 show the equilibrium volumes at 0 bar for different Zr-Cu-Al-Ni liquid alloy as calculated by the EAM potential superimposed with the experimental data from [58]. The slopes of the V-T curve agree with the experimental value. The overall increase in volume can be attributed to the addition of Ni. It was discerned that with a fixed amount of Zr, replacing Cu with Ni decrease the molar volume of the liquid which can be explained by the difference of Molar volume of Ni (6.59 cm^3mol^{-1}) compared to Cu (7.11 cm^3mol^{-1}). Surprisingly, the molar volume argument seems to fail in cases where increasing Zr at the cost of Cu keeping Al and Ni concentration fixed causes a decrease in Molar Volume. Similar trend is observed when the mutual concentration of Zr and Ni is varied keeping Cu and Al concentration fixed. This behavior could probably be explained by the possibility that deviation from the central $Zr_{55}Cu_{30}Al_{10}Ni_5$ alloy cause deviation from the ideal glass-forming icosahedral symmetry to some more close packed structure which cause a decrease in *excess free volume*[59] of the overall structure.

[1] in literature these two terms are often used interchangeably

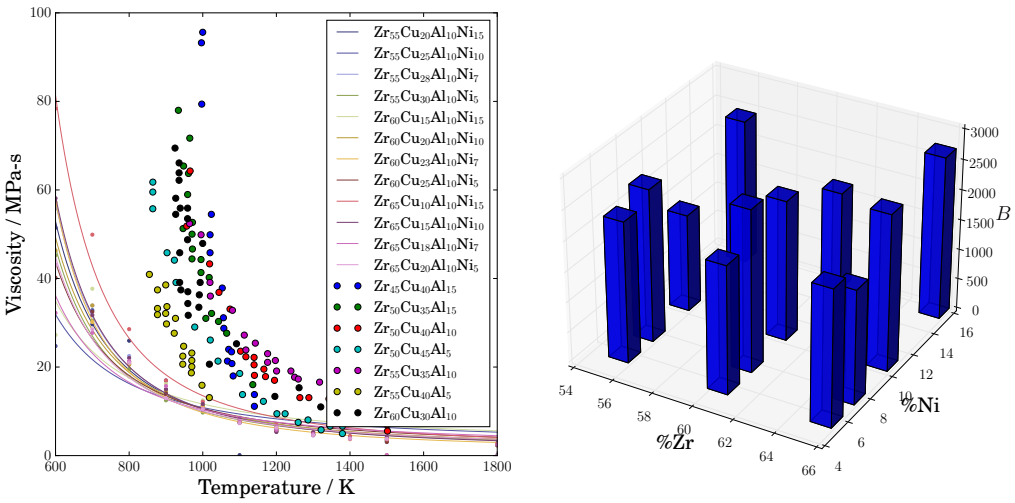

(a) (b)

Figure 5.5: (a) Calculated Viscosity for $Zr_{55+x}Cu_{30-x-y}Al_{10}Ni_{5+y}$ structures between 600-2000 K. The dotted points are experimental reference from Zr-Cu-Al liquids[58]. Note that due to difference of temperature scale, the calculated and experimental values are not directly comparable beyond the reasons of compositions; (b) B for different $Zr_{55+x}Cu_{30-x-y}Al_{10}Ni_{5+y}$. The difference of 100 - 10 - %Zr - %Ni defines the x% of Cu.

In Fig. 5.5a, we show the plot of viscosity for all temperature and the fitted Vogel-Fulcher-Tammann Equation : $\eta = \eta_0 e^{B/T}$[60] for each structure. The dotted points superimposed for reference are from the work of Yokoyama and colleagues[58], the fitted values for the exponential coefficient B, for different compositions is shown in Fig. 5.5b. Replacing Cu with Ni keeping Zr and Al concentration fixed increase the viscosity at all temperatures. These trend are in agreement to the results of Li et. al.[61] where they state that addition of elements of comparable concentration increase the 'confusion effect'[17] and therefore have greater GFA. Similarly, keeping Al and Ni fixed causes reduction in viscosity with an increase in Zr at the cost of Cu. This could be directly related to the reduction in GFA, since it has been reported that lethargy of flow promotes vitrification upon cooling in BMGs[62]. It must be noted that while the trend is akin, the temperature scale of the MD simulations and experiments are not comparable.

5.4 Conclusion

In this work we fitted a new EAM Zr-Cu-Al-Ni analytical potential built primarily to support classical MD simulations for liquid alloys. The EAM was validated by testing it on a independent set of known reference data and we obtained good agreement both in energy and RMS average force. The equilibrium volume at 0 bar pressure for structures in the neighborhood of $Zr_{55}Cu_{30}Al_{10}Ni_5$ fall within the range and trends of other experimentally determined Zr-Cu-Al BMG liquids. Likewise, the trends in the equilibrium volume corroborate with that in the viscosity calculations. The EAM

results concur with the empirical correlations between GFA and viscosity. Based on the simulations, Zr at 55% is a important central composition, furthermore addition of Ni increase viscosity and ergo GFA. Initial analysis also suggests that equi-molar concentration of the multiple minor elements promote GFA. Both of which are in agreement to known experimental results. The reported EAM potential could therefore potentially be of use in accelerating screening of candidate structures in novel BMGs of the Zr-Cu-Al-Ni family in a high-throughput pipeline.

References

1. Chen, H. S. Glassy metals. *Rep. Prog. Phys.* **43,** 353–432 (1980).
2. Inoue, A. Stabilization of metallic supercooled liquid and bulk amorphous alloys. *Acta Materialia* **48,** 279–306 (2000).
3. Greer, A. L. & Ma, E. Bulk Metallic Glasses: At the Cutting Edge of Metals Research. *MRS Bulletin* **32,** 611–619 (2007).
4. Greer, A. L. Metallic glasses... on the threshold. *Materials Today* **12,** 14–22 (2009).
5. Ashby, M. F. & Greer, A. L. Metallic glasses as structural materials. *Scripta Materialia. Viewpoint set no: 37. On mechanical behavior of metallic glasses* **54,** 321–326 (2006).
6. Ren, F., Ward, L., Williams, T., Laws, K. J., Wolverton, C., Hattrick-Simpers, J., *et al.* Accelerated discovery of metallic glasses through iteration of machine learning and high-throughput experiments. *Science Advances* **4,** 1566 (2018).
7. Inoue, A. High Strength Bulk Amorphous Alloys with Low Critical Cooling Rates (Overview). *Materials Transactions, JIM* **36,** 866–875 (1995).
8. Laws, K. J., Miracle, D. B. & Ferry, M. A predictive structural model for bulk metallic glasses. *Nat Commun* **6,** 8123 (2015).
9. Turnbull, D. Under what conditions can a glass be formed? *Contemporary Physics* **10,** 473–488 (1969).
10. Perim, E., Lee, D., Liu, Y., Toher, C., Gong, P., Li, Y., *et al.* Spectral descriptors for bulk metallic glasses based on the thermodynamics of competing crystalline phases. *Nature Communications* **7,** 12315 (2016).
11. Vincent, S., Peshwe, D. R., Murty, B. S. & Bhatt, J. Thermodynamic prediction of bulk metallic glass forming alloys in ternary Zr-Cu-X (X = Ag, Al, Ti, Ga) systems. *Journal of Non Crystalline Solids* **357,** 3495 (2011).
12. Zhang, K., Dice, B., Liu, Y., Schroers, J., Shattuck, M. D. & O'Hern, C. S. On the origin of multi-component bulk metallic glasses: Atomic size mismatches and de-mixing. *J. Chem. Phys.* **143,** 054501 (2015).
13. Miracle, D. B. A structural model for metallic glasses. *Nature Mater* **3,** 697–702 (2004).

14. Bernal, J. D. A Geometrical Approach to the Structure Of Liquids. *Nature* **183,** 141–147 (1959).

15. Bernal, J. D. Geometry of the Structure of Monatomic Liquids. *Nature* **185,** 68–70 (1960).

16. Inoue, A., Zhang, T. & Takeuchi, A. Ferrous and Nonferrous Bulk Amorphous Alloys. *Materials Science Forum* **269-272,** 855–864 (1998).

17. Greer, A. L. Confusion by design. *Nature* **366,** 303–304 (1993).

18. Sheng, H. W., Luo, W. K., Alamgir, F. M., Bai, J. M. & Ma, E. Atomic packing and short-to-medium-range order in metallic glasses. *Nature* **439,** 419–425 (2006).

19. Shen, Y. T., Kim, T. H., Gangopadhyay, A. K. & Kelton, K. F. Icosahedral Order, Frustration, and the Glass Transition: Evidence from Time-Dependent Nucleation and Supercooled Liquid Structure Studies. *Phys. Rev. Lett.* **102,** 057801 (2009).

20. Li, Y., Zhao, S., Liu, Y., Gong, P. & Schroers, J. How Many Bulk Metallic Glasses Are There? *ACS Comb. Sci.* **19,** 687–693 (2017).

21. Inoue, A., Zhang, T. & Masumoto, T. Zr–Al–Ni Amorphous Alloys with High Glass Transition Temperature and Significant Supercooled Liquid Region. *Materials Transactions, JIM* **31,** 177–183 (1990).

22. Zhang, T., Inoue, A. & Masumoto, T. Amorphous Zr–Al–TM (TM=Co, Ni, Cu) Alloys with Significant Supercooled Liquid Region of Over 100 K. *Materials Transactions, JIM* **32,** 1005–1010 (1991).

23. Georgarakis, K., Yavari, A. R., Louzguine-Luzgin, D. V., Antonowicz, J., Stoica, M., Li, Y., *et al.* Atomic structure of Zr–Cu glassy alloys and detection of deviations from ideal solution behavior with Al addition by x-ray diffraction using synchrotron light in transmission. *Appl. Phys. Lett.* **94,** 191912 (2009).

24. Georgarakis, K., Yavari, A. R., Aljerf, M., Louzguine-Luzgin, D. V., Stoica, M., Vaughan, G., *et al.* On the atomic structure of Zr–Ni and Zr–Ni–Al metallic glasses. *Journal of Applied Physics* **108,** 023514 (2010).

25. Chen, W., Wang, Y., Qiang, J. & Dong, C. Bulk metallic glasses in the Zr-Al-Ni-Cu system. *Acta Materialia* **51,** 1899–1907 (2003).

26. Peker, A. & Johnson, W. L. A highly processable metallic glass: $Zr_{41.2}Ti_{13.8}Cu_{12.5}Ni_{10.0}Be_{22.5}$. *Appl. Phys. Lett.* **63,** 2342–2344 (1993).

27. Dabrowa, J., Perriere, L., Stygar, M., Kucza, W., Klita, L. & Danielewski, M. Oxidation Behavior of $Zr_{43}Cu_{45}Al_{12}$ Bulk Metallic Glass at 400-525°C in Air Atmosphere. *J. of Materi Eng and Perform* **24,** 4863–4869 (2015).

28. Kai, W., Lin, P. C., Chen, W. S., Chuang, C. P., Liaw, P. K., Huang, H. H., *et al.* Air-oxidation of a $Zr_{50}Cu_{43}Al_7$ bulk metallic glass at 400–500°C. *Corrosion Science* **64,** 98–104 (2012).

29. Singh, D., Mandal, R. K., Tiwari, R. S. & Srivastava, O. N. *Mechanical Behavior of Zr-Based Metallic Glasses and Their Nanocomposites* (IntechOpen, 2016).

30. Cheng, Y. Q., Ma, E. & Sheng, H. W. Atomic Level Structure in Multicomponent Bulk Metallic Glass. *Phys. Rev. Lett.* **102,** 245501 (2009).

31. Green, M. S. Markoff Random Processes and the Statistical Mechanics of Time-Dependent Phenomena. II. Irreversible Processes in Fluids. *The Journal of Chemical Physics* **22,** 398–413. ISSN: 0021-9606, 1089-7690 (1954).

32. Kubo, R. Statistical-Mechanical Theory of Irreversible Processes. I. General Theory and Simple Applications to Magnetic and Conduction Problems. *Journal of the Physical Society of Japan* **12,** 570–586. (2022) (1957).

33. Kubo, R. The fluctuation-dissipation theorem. *Reports on Progress in Physics* **29,** 255–284. (2020) (1966).

34. Yamasaki, T., Yamada, M., Mori, T., Kikuchi, T., Yokoyama, Y., Inoue, A., *et al.* Viscous Flow Behaviour of Supercooled Liquids and Mechanical Properties in Zr-Cu-Ni-Al Bulk Metallic Glasses. *Materials Science Forum* **654-656,** 1046–1049 (2010).

35. Kübler, A., Eckert, J., Gebert, A. & Schultz, L. Influence of oxygen on the viscosity of Zr–Al–Cu–Ni metallic glasses in the undercooled liquid region. *Journal of Applied Physics* **83,** 3438 (1998).

36. Gebert, A., Buchholz, K., El-Aziz, A. & Eckert, J. Hot water corrosion behaviour of Zr–Cu–Al–Ni bulk metallic glass. *Materials Science and Engineering: A* **316,** 60–65 (2001).

37. Jun, H.-J., Lee, K., Eckert, J. & Chang, Y. High-Temperature Deformation Behavior and Formability of a Zr-Cu-Al-Ni Bulk Metallic Glass. *Metallurgical and Materials Transactions A* **39,** 1831–1837 (2008).

38. Kato, H., Inoue, A. & Chen, H. S. Heating and structural disordering effects of the nonlinear viscous flow in a $Zr_{55}Al_{10}Ni_5Cu_{30}$ bulk metallic glass. *Applied Physics Letters,* 4 (2009).

39. Xue, R. J., Wang, D. P., Zhu, Z. G., Ding, D. W., Zhang, B. & Wang, W. H. Characterization of flow units in metallic glass through density variation. *Journal of Applied Physics* **114,** 123514 (2013).

40. Slipenyuk, A. & Eckert, J. Correlation between enthalpy change and free volume reduction during structural relaxation of $Zr_{55}Cu_{30}Al_{10}Ni_5$ metallic glass. *Scripta Materialia* **50,** 39–44 (2004).

41. Xie, G., Zhang, W., Louzguine-Luzgin, D. V., Kimura, H. & Inoue, A. Fabrication of porous Zr–Cu–Al–Ni bulk metallic glass by spark plasma sintering process. *Scripta Materialia* **55,** 687–690 (2006).

42. Ong, S. P., Cholia, S., Jain, A., Brafman, M., Gunter, D., Ceder, G., *et al.* The Materials Application Programming Interface (API): A simple, flexible and efficient API for materials data based on REpresentational State Transfer (REST) principles. *Computational Materials Science* **97,** 209–215 (2015).

43. Jain, A., Ong, S. P., Hautier, G., Chen, W., Richards, W. D., Dacek, S., *et al.* Commentary: The Materials Project: A materials genome approach to accelerating materials innovation. *APL Materials* **1,** 011002 (2013).

44. Blöchl, P. E. Projector augmented-wave method. *Phys. Rev. B* **50,** 17953–17979 (1994).

45. Kresse, G. & Joubert, D. From ultrasoft pseudopotentials to the projector augmented-wave method. *Phys. Rev. B* **59,** 1758–1775 (3 1999).

46. Perdew, J. P., Burke, K. & Ernzerhof, M. Generalized Gradient Approximation Made Simple. *Phys. Rev. Lett.* **77,** 3865–3868 (1996).

47. Methfessel, M. & Paxton, A. T. High-precision sampling for Brillouin-zone integration in metals. *Phys. Rev. B* **40,** 3616–3621 (1989).

48. Blöchl, P. E., Jepsen, O. & Andersen, O. K. Improved tetrahedron method for Brillouin-zone integrations. *Phys. Rev. B* **49,** 16223–16233 (23 1994).

49. Thompson, A. P., Aktulga, H. M., Berger, R., Bolintineanu, D. S., Brown, W. M., Crozier, P. S., *et al.* LAMMPS - a flexible simulation tool for particle-based materials modeling at the atomic, meso, and continuum scales. *Comp. Phys. Comm.* **271,** 108171 (2022).

50. Morse, P. M. Diatomic Molecules According to the Wave Mechanics. II. Vibrational Levels. *Phys. Rev.* **34,** 57–64 (1929).

51. Chantasiriwan, S. & Milstein, F. Higher-order elasticity of cubic metals in the embedded-atom method. *Phys. Rev. B* **53,** 14080–14088 (1996).

52. Banerjea, A. & Smith, J. R. Origins of the universal binding-energy relation. *Phys. Rev. B* **37,** 6632–6645 (1988).

53. Brommer, P. & Gähler, F. Potfit: effective potentials from ab-initio data. *Modelling and Simulation in Materials Science and Engineering* **15,** 295–304 (2007).

54. Ercolessi, F. & Adams, J. B. Interatomic Potentials from First-Principles Calculations: The Force-Matching Method. *EPL (Europhysics Letters)* **26,** 583–588 (1994).

55. Kirkpatrick, S., Gelatt, C. D. & Vecchi, M. P. Optimization by Simulated Annealing. *Science* **220,** 671–680 (1983).

56. Metropolis, N., Rosenbluth, A. W., Rosenbluth, M. N., Teller, A. H. & Teller, E. Equation of State Calculations by Fast Computing Machines. *The Journal of Chemical Physics* **21,** 1087–1092 (1953).

57. Powell, M. J. D. A Method for Minimizing a Sum of Squares of Non-Linear Functions Without Calculating Derivatives. *The Computer Journal* **7,** 303–307 (1965).

58. Yokoyama, Y., Ishikawa, T., Okada, J. T., Watanabe, Y., Nanao, S. & Inoue, A. Volume and viscosity of Zr–Cu–Al glass-forming liquid alloys. *Journal of Non-Crystalline Solids* **355,** 317–322 (2009).

59. Turnbull, D. & Cohen, M. H. On the Free-Volume Model of the Liquid-Glass Transition. *The Journal of Chemical Physics* **52,** 3038–3041 (1970).

60. Ngai, K. *Relaxation and Diffusion in Complex Systems (Partially Ordered Systems Book 0)* 1727 (Springer, Mar. 25, 2011).

61. Li, Y., Zhang, W., Dong, C., Qiang, J., Fukuhara, M., Makino, A., *et al.* Effects of Ni addition on the glass-forming ability, mechanical properties and corrosion resistance of Zr–Cu–Al bulk metallic glasses. *Materials Science and Engineering: A* **528,** 8551–8556 (2011).

62. Yavari, A. R. & Desre, P. Substrate-induced liquid shearing and defect anisotropy in metallic glasses. *Journal of Physics F: Metal Physics* **14,** 291–299 (1984).

Chapter 6

Conclusions

The results from Chapter 3 and Chapter 4 reveal the efficacy of the SQS formalism + short CVM SRO correction to analyze the thermodynamics of alloys up to a reasonable degree of accuracy within the CALPHAD framework. Our approach is completely from first-principles and is amenable for incorporation into other high-throughput pipelines. The systematic improve-ability of the system alloys enables the user to obtain a balance between accuracy and speed and thus perform a wide spectrum of analysis. The possibility of inclusion of experimental data at any point of the analysis to augment present models imply compatibility with pre-existing data. In Chapter 3, it was convincingly proven that use of SQS significantly reduce computation cost and is a suitable representation of high-T disordered phase in the CALPHAD framework with small enough number of atoms for feasible high-throughput DFT. Using the code `sqs2tdb`, past experimental/DFT discrepancy regarding stability of ordered phases at low T was resolved. It was established that disordered alloys predicted to be stable at 0 K disorder below room temperature due to entropic effects admittedly with sustained partial ordering. We thus additionally proposed short-range CVM mediated SRO corrections in Chapter 4 to resolve this low-T discrepancy. The encompassing CVM+SQS+CALPHAD paradigm provide for accurate CALPHAD thermodynamic assessments of order/partially ordered/disordered systems in a single phase description. A thermodynamic description for Ir-Ru binary alloy was generated using this scheme and it was established that even with a short range CVM using the `srocorrection` code on top of `sqs2tdb` analysis re-produced the hcp side of the Ir-Ru binary phase diagram with good accuracy compared to experimental investigations.

We also constructed a Zr-Cu-Al-Ni Embedded Atom Method (EAM) classical inter-atomic potential in Chapter 5 using analytical parametric functions for the individual pair, charge density and embedding energy functions. The EAM coefficients were obtained by performing numerical regression over a set of Zr, Cu, Al and Ni containing binary and ternary intermetallics and liquid structures calculated from DFT. Evaluation of the EAM performance with a first-principles data-set convey a good degree of agreement to the liquid phase of Zr-Cu-Al-Ni bulk metallic glass (BMG) forming

alloy. The EAM analysis confirmed experimental evidence that addition of small amounts of Ni, enhance the viscosity hence Glass Forming Ability (GFA) of Zr-Cu-Al systems. It also corroborated reduction in GFA away from 55% Zr compositions. The trends of equilibrium volume and shear viscosity offer confidence in using the EAM potential in high-throughput kinetic analysis of such non-equilibrium phase.

All methods above entail approximating free energies with a simple functions (functionals) from select few first-principle calculations. In this concluding chapter, it is worth discussing some of the ways in which these techniques can be applied to further scientific advancements and engineering applications. Generation of phase diagrams without any experimental input is a novelty to the field of high-throughput alloy design. Especially as the engineering community is increasingly looking at 4-or more elements alloys where experiment focused prototyping is getting increasingly difficult. The manifestation of short-range ordering with or without the presence of lattice crystalinity is crucial in establishing the stable structures/energetics and therefore properties of alloys. As an example, in novel cathode materials for Li-ion batteries, the manifestation of local structure with increasing amounts of Li correlate directly to the capacity in the charge-discharge cycles[1–4]. Likewise in perovskite nano-crystals in solar cells materials, it was observed that low amounts of doping modify the local ordering to improve photoluminescence quantum yields (PLQYs)[5–8]. Unfortunately studies related to ordering has been limited to indirect analysis via radial distribution functions, experimental reasoning and empirical models. Attempts using the empirical *order parameter* is also defined only up to nearest neighbour order. In the light of these existing gaps, a rigorous multi-body SRO order assessment would benefit the community manifold. Similarly, in the field of High Entropy Alloys, the ordering of elements is so far tackled in an heuristic Hume-Rothery like rules. An accurate SRO estimate has potential in establishing a fundamental footing behind empirical trends.

A natural extension of CVM to time domain is the Path Probability Method (PPM)[9] which is useful for predicting transformation and relaxation kinetics[10]. Additionally a Fourier transformed version of cluster probabilities can be used to study the intrinsic stability of a system[11]. A Continuous Displacement Cluster Variation Method (CDCVM)[12, 13], which as a continuous generalization of CVM reformulates cluster probabilities as continuous probability distributions over quasi-lattice points around the unit-cell lattice sites. These extensions to CVM have been shown promising results with it's compatibility to interface with meso-scale Phase Field methods[14–16]. Although these methods have existed since early 1990's, recent developments in high dimensional optimization frameworks might infuse fresh breath to these erstwhile intractable models.

The vast depth of classical inter-atomic potential is not done thorough justice in the work. With the popularization of high-dimensional non-linear regression in the field of Machine Learning/Artificial Intelligence, the materials science community has now a zoo of many symmetry-equivariant descriptors. All of which target to map the structure to the energy/forces to reasonable degree of accuracy and computational simplicity[17–21]. These extend the energetic interaction beyond pair

and mean field approximations of EAM to more sophisticated models, involving many-body terms for greater expressivity. Even deviations from strict analytical functions to spline interpolations on a grid of points can provide sufficient flexibility for the model to accurately describe the system within the force-matching methodology. The lack of generalizability of such potentials is also a target for improvement.

References

1. Meng, Y. S. & Arroyo-de Dompablo, M. E. Recent Advances in First Principles Computational Research of Cathode Materials for Lithium-Ion Batteries. *Accounts of Chemical Research* **46,** 1171–1180. (2022) (2013).
2. Christensen, C. K., Sørensen, D. R., Hvam, J. & Ravnsbæk, D. B. Structural Evolution of Disordered $Li_xV_2O_5$ Bronzes in V_2O_5 Cathodes for Li-Ion Batteries. *Chemistry of Materials* **31,** 512–520 (Jan. 2019).
3. Lun, Z., Ouyang, B., Kwon, D.-H., Ha, Y., Foley, E. E., Huang, T.-Y., *et al.* Cation-disordered rocksalt-type high-entropy cathodes for Li-ion batteries. *Nature Materials* **20,** 214–221 (2021).
4. Wolverton, C. & Zunger, A. Cation and vacancy ordering in Li_xCoO_2. *Physical Review B* **57,** 2242–2252 (1998).
5. Yong, Z.-J., Guo, S.-Q., Ma, J.-P., Zhang, J.-Y., Li, Z.-Y., Chen, Y.-M., *et al.* Doping-Enhanced Short-Range Order of Perovskite Nanocrystals for Near-Unity Violet Luminescence Quantum Yield. *Journal of the American Chemical Society* **140,** 9942–9951 (2018).
6. Yuan, G., Huang, S., Qin, S., Wu, X., Ding, H. & Lu, A. Structural, Optical, and Thermal Properties of $Cs_2SnI_{6-x}Br_x$ Mixed Perovskite Solid Solutions. *European Journal of Inorganic Chemistry* **2019,** 2524–2529 (2019).
7. Sonigara, K. K., Shao, Z., Prasad, J., Machhi, H. K., Cui, G., Pang, S., *et al.* Organic Ionic Plastic Crystals as Hole Transporting Layer for Stable and Efficient Perovskite Solar Cells. *Advanced Functional Materials* **30,** 2001460 (2020).
8. Liu, T., Li, Y., Feng, S., Yang, W., Xu, R., Zhang, X., *et al.* Incorporation of Nickel Ions to Enhance Integrity and Stability of Perovskite Crystal Lattice for High-Performance Planar Heterojunction Solar Cells. *ACS Applied Materials & Interfaces* **12,** 904–913 (2020).
9. Kikuchi, R. The Path Probability Method. *Progress of Theoretical Physics Supplement* **35,** 1–64. (2022) (1966).
10. Yamada, R., Ohno, M. & Mohri, T. Configurational kinetics studied by Path Probability Method. *Progress in Materials Science* **120,** 100765 (2021).
11. Uzawa, H. & Mohri, T. Continuous Displacement Cluster Variation Method in Fourier Space. *Materials Transactions* **43,** 2185–2188 (2002).

12. Kikuchi, R. & Beldjenna, A. Continuous displacement of “lattice” atoms. *Physica A: Statistical Mechanics and its Applications* **182,** 617–634 (1992).

13. Mohri, T. Cluster Variation Method. *JOM* **65,** 1510–1522 (2013).

14. Chen, L.-Q. Phase-Field Models for Microstructure Evolution. *Annual Review of Materials Research* **32,** 113–140 (2002).

15. Ohno, M. & Mohri, T. Disorder-$L1_0$ Transition Investigated by Phase Field Method with CVM Local Free Energy. *Materials Transactions* **42,** 2033–2041 (2001).

16. Mohri, T., Ohno, M. & Chen, Y. First-principles calculations of phase equilibria and transformation dynamics of Fe-based alloys. *Journal of Phase Equilibria and Diffusion* **27,** 47–53 (2006).

17. Thompson, A. P., Swiler, L. P., Trott, C. R., Foiles, S. M. & Tucker, G. J. Spectral neighbor analysis method for automated generation of quantum-accurate interatomic potentials. *Journal of Computational Physics* **285,** 316–330 (2015).

18. Behler, J. & Parrinello, M. Generalized Neural-Network Representation of High-Dimensional Potential-Energy Surfaces. *Physical Review Letters* **98,** 146401 (2007).

19. Thomas, N., Smidt, T., Kearnes, S., Yang, L., Li, L., Kohlhoff, K., *et al.* Tensor field networks: Rotation- and translation-equivariant neural networks for 3D point clouds. *arXiv:1802.08219 [cs]* (2018).

20. Drautz, R. Atomic cluster expansion for accurate and transferable interatomic potentials. *Physical Review B* **99,** 014104 (2019).

21. Sinz, P., Swift, M. W., Brumwell, X., Liu, J., Kim, K. J., Qi, Y., *et al.* Wavelet scattering networks for atomistic systems with extrapolation of material properties. *The Journal of Chemical Physics* **153,** 084109 (2020).

Appendix A

ATAT Commands used to generate Ir-Ru Binary phase diagram

To facilitate reproducing the results and help readers undertake their own analysis on other systems, we here provide the commands of the ATAT package used in this work (we omit ab initio code-specific commands).

1. To generate the input structures for the ab initio calculations, we use:

   ```
   sqs2tdb -cp -lv=[1,2,3], -l=[FCC_A1,BCC_A2,...] -sp=Ir,Ru
   ```

   This creates a set of folder for each phase where the SQS structures up to the desired levels are copied. We can run our ab-initio code inside these to calculate the electronic ground state structure and energy.

2. For the phonon calculations:

   For every level of a particular phase for which we want to include phonon vibrational entropy calculations, we can generate symmetrically distinct configurations with specified displacements per atom and distance between the periodic images of the displaced atom (here the distance between two periodic atom images is in units of nearest neighbour distance. Check [8] for more details).

   ```
   fitfc -ernn=4 -ns=1 -dr=0.04
   ```

   This creates a set of folders `vol_*/p*` representing every symmetrically distinct perturbed structures. Calculate energy of each from ab-initio method. Then we can fit the forces to a specified spring model (here `ns=1` indicate a harmonic model), using the code snippet

   ```
   fitfc -frnn=2 -ns=1 -dr=0.04 -fu
   ```

The `-fu` tag provides information on the unstable modes if any suggested by the initial fit report suggestive of the presence of mechanical instability. If any such modes are suspected, we can read the file `vol_*/unstable.out`. Re-running the fitting procedure with an addition tag `-gu=[index]`, creates a supercell representing the mode describing the imaginary mode which is described in the row matching the `[index]` at the second column of the `vol_*/unstable.out` file . We can then calculate the reaction forces in the direction and include it in the fit. Often if the instability is an artifact of the fitting process (imaginary modes), this process can solve the issue. Note that this process might have to be repeated multiple times until we include all the suspected unstable modes in our fit or unless a true unstable mode is found.

3. Generate Thermodynamic Database file:

   We first input to the code the types of interactions (just single atom, binary, ternary etc.) and to which levels (0,1,2 etc.) in the excess free energy term as per the CALPHAD formalism [9] in to the `terms.in` file with the following format

   ```
   cat <<EOF > terms.in
   1,0:1,0
   2,1:1,0
   EOF
   ```

   (the example shown is for a two sublattice phase where we include all first order terms (only level 0 is possible). We also include order 2 terms with 1 level. Note. that the CALPHAD model only allows greater than 1 order for only one sublattice at a time.)

   Then run the command:

   ```
   sqs2tdb -fit [-sro]
   ```

   This creates a partial Thermodynamic DataBase (TDB) file containing the function and structure for the particular phase. The optional parameter `-sro` can be specified to include short-range order effects in single-sublattice phases (this was used for the fcc and hcp phases in this work). It is at this step when the code decides which reference values are to be drawn from SGTE database or not. These individual TDB files (one for each phase) can be combined in to a single TDB file for the alloy system using the command.

   ```
   sqs2tdb -tdb [-oc]
   ```

   The `-oc` tag is optional used to create the TDB file in the OpenCalphad format (OC) [10]

Appendix B

List of parameters - CVM SRO Correction Code

Parameter Name	Description	Default
Optimization Parameters		
`no_constraint`	Flag to disable norm constraint	`False`
`constr_tol`	Maximum accepted constraint violation	`1e-5`
`fit_ordered_only`	Only calculate ordered correlations and exit	`False`
`approx_deriv`	Flag to enable numerical estimation of derivatives	`False`
`no_inter`	Flag to disable intermediate optimization results	`False`
`maxiter`	Maximum no. of iterations for the optimiser	`5000`
`maxiter_simplex`	Maximum no. of iterations for the ordered correlation calculator	`1000000`
`earlystop`	No. of trials before termination if no new minima is found	`25`
`xtol`	tolerance termination by the change of the independent variable.	`1e-12`

List of parameters and default values for CVM SRO correction Code. (continued next page ...)

Parameter Name	Description	Default
`gtol`	tolerance for termination by the norm of the lagrangian gradient	`1e-12`
`trial_variance`	variance of the gaussian around the disordered correlations from which the trial correlations are sampled	`1e-3`
`initial_tr_radius`	Initial guess trial radius for the trust-region optimiser	`1e-2`
`global_trials`	No. of trials to find global minima for each temperature	`50`
`init_trials`	No. of brute force samples to find appropriate trust radius	`1000`
`out`	Name of the output file	`result.json`
`toscreen`	Flag to display output to stdout	`False`
`log`	Name of the log file	`log`
SRO Parameters		
`Tmin`	Minimum temperature to perform SRO correction optimization	`100`
`Tmax`	Maximum temperature to perform SRO correction optimization	`2000`
`Tstep`	Temperature steps between Tmin and Tmax	`1e-12`
`inJoules`	Flag to set energy units to kJ/mol	`False`
`coeff_out`	File name for the output of the coefficients of the SRO correction vs T fit	`sro_coeffs.out`
`skip_sro_fit`*	Flag to skip the SRO correction vs T fit	`False`
`fit_sro_only`*	Flag to fit SRO only with existing optimization if any	`False`
Cluster Description Parameters†		
`eci`	File containing the ECI values	`eci.out`

List of parameters and default values for CVM SRO correction Code. (continued next page ...)

*These commands are complementary

†to be defined in case of user defined clusters not obtained from `maxclus.in` or to read from an alternate maximal cluster file

Parameter Name	Description	Default
`maximal_clusters`	File containing the maximal cluster description	`maxclus.in`
`clusters`	File containing the cluster description	`clusters.out`
`clustermult`	File containing the cluster multiplicities	`clusmult.out`
`kb`	File containing Kikuchi-Baker Coefficients	`kb.out`
`configmult`	File containing cluster configuration multiplicities	`configmult.out`
`config`	File containing cluster configuration description	`config.out`
`lat`	File containing lattice description	`lat.in`

Table B.1: List of parameters and default values for CVM SRO correction Code.

Appendix C

Matrix Formulation - Free Energy function, Jacobian and Hessian

From 2.42, the CVM Free energy function is given by The equation for free energy in the cluster variation formalism is given by:

$$F = \sum_{i}^{\text{clusters}} m_i J_i \xi_i + k_B T \sum_{i}^{\text{configs}} k_i \left[\sum_{j}^{\text{subconfig}} \alpha_{ij} \left(\sum_{c}^{\text{corrs}} v_{ijc} \xi_c \right) \log \left(\sum_{c}^{\text{corrs}} v_{ijc} \xi_c \right) \right] \tag{C.1}$$

C.1 Enthalpy

The Enthalpy function:

$$H = \sum_{i}^{\text{clusters}} m_i J_i \xi_i \tag{C.2}$$

can be written in the matrix form as:

$$\begin{aligned} H &= \sum M_{\text{clus}} \odot E \odot \xi \\ &= (M_{\text{clus}} \odot E) \cdot \xi \end{aligned} \tag{C.3}$$

C.1.1 Jacobian - Enthalpy

$$\frac{\partial H}{\partial \xi} = M_{\text{clus}} \odot E \tag{C.4}$$

C.1.2 Hessian - Enthalpy

$$\frac{\partial^2 H}{\partial \xi \partial \xi} = \varnothing \tag{C.5}$$

C.2 Entropy

Likewise, re-writing the Entropy function

$$\frac{S}{k_{\mathrm{B}}T} = \sum_{i}^{\text{configs}} k_i \left[\sum_{j}^{\text{subconfig}} \alpha_{ij} \left(\sum_{c}^{\text{corrs}} v_{ijc}\xi_c \right) \log \left(\sum_{c}^{\text{corrs}} v_{ijc}\xi_c \right) \right] \tag{C.6}$$

in the matrix form:

$$\frac{S}{k_{\mathrm{B}}T} = (K \odot M_c) \cdot (V\xi \odot \log |V\xi|) \tag{C.7}$$

C.2.1 Jacobian - Entropy

Applying chain-rule of differentiation, we get

$$\frac{\partial S}{\partial \xi} = \frac{\partial S_1}{\partial \xi} + \frac{\partial S_2}{\partial \xi} \tag{C.8}$$

where

$$\begin{aligned} \frac{\partial S_1}{\partial \xi} &= (K \odot M_c \odot \log |V\xi|) \cdot \frac{\partial (V\xi)}{\partial \xi} \\ &= (K \odot M_c \odot \log |V\xi|) \cdot V \\ &= V^T (K \odot M_c \odot \log |V\xi|) \end{aligned} \tag{C.9}$$

$$\begin{aligned} \frac{\partial S_2}{\partial \xi} &= (K \odot M_c) \odot (V\xi) \cdot \frac{\partial}{\partial \xi} \log |V\xi| \\ &= (K \odot M_c) \odot \cancel{V\xi} \frac{1}{\cancel{V\xi}} \cdot V \\ &= (K \odot M_c) \cdot V \\ &= V^T (K \odot M_c) \end{aligned} \tag{C.10}$$

Therefore

$$\begin{aligned} \frac{1}{k_{\mathrm{B}}T} \frac{\partial S}{\partial \xi} &= V^T (K \odot M_c \odot \log |V\xi|) + V^T (K \odot M_c) \\ &= V^T \left[K \odot M_c \odot (1 \oplus \log |V\xi|) \right] \end{aligned} \tag{C.11}$$

C.2.2 Hessian - Entropy

$$\begin{aligned}\frac{\partial^2 S}{\partial \xi \partial \xi'} &= V^T \left[(K \odot M_c) \odot \frac{\partial}{\partial \xi} \log |V\xi| \right] \\ &= V^T (\operatorname{diag}\left[(K \odot M_c) \oslash (V\xi) \right] V) \\ &= (\operatorname{diag}\left[(K \odot M_c) \oslash (V\xi) \right] V)^T V\end{aligned} \tag{C.12}$$

Appendix D

Potential Coefficients - Zr-Cu-Al-Ni EAM potential

D.1 EAM Functions

D.1.1 Pair Functions

	D_e	a	r_e
Zr-Zr	0.0	1.0772	10.000
Zr-Cu	0.043	1.492	3.477
Zr-Al	0.054	1.494	3.515
Zr-Ni	0.13	1.383	3.121
Cu-Cu	0.031	1.861	3.064
Cu-Al	0.024	2.005	3.027
Cu-Ni	0.136	1.704	2.781
Al-Al	0.002	1.809	3.927
Al-Ni	0.275	1.437	2.705
Ni-Ni	0.219	1.804	2.616

Table D.1: Coefficients of all pair interaction Morse functions.

D.1.2 Transfer/Electron density Functions

	a	α	φ	β
Zr	-0.215	3.078	5.274	3.320
Cu	0.679	2.223	1.177	4.277
Al	-0.404	3.249	0.261	3.969
Ni	-0.898	2.150	4.919	3.301

Table D.2: Coefficients of all electron density CSW functions.

D.1.3 Embedding energy Functions

	F_0	γ	F_1
Zr	-9.276	0.881	0.016
Cu	-4.311	0.785	0.012
Al	-4.541	0.625	-0.036
Ni	-2.941	0.234	-0.002

Table D.3: Coefficients of all embedding energy universal BJS functions

D.2 LAMMPS Molecular Dynamics Schedules

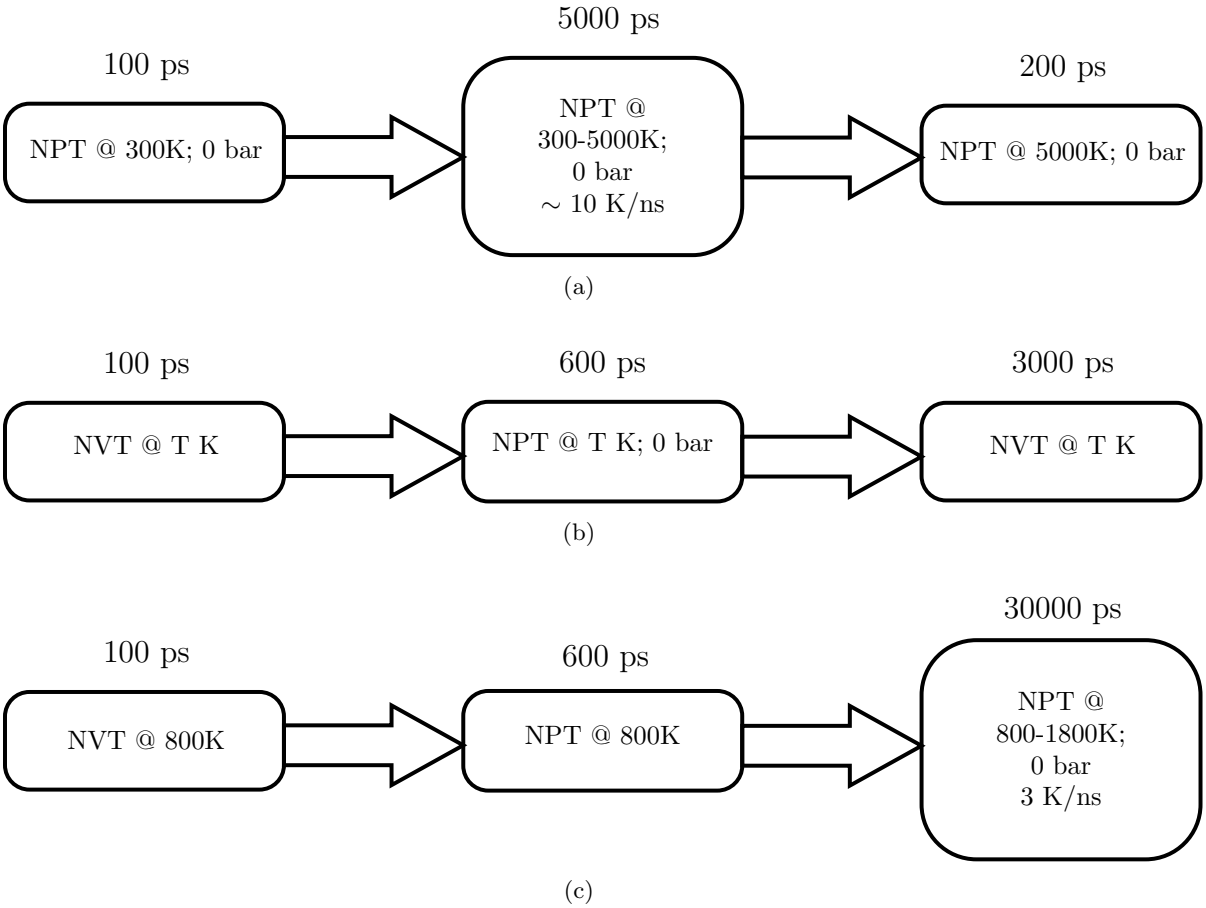

Figure D.1: LAMMPS MD schedules for (a) Generating initial structures at each composition for viscosity and volume calculations, (b) Calculating viscosity for each structure at a particular temperature T and (c) Calculating equilibrium volume at 0 bar pressure between 800 - 1800 K